Dissertation

Magnetization Dynamics of Itinerant and Localized Electrons in Lanthanide Metals

Björn Frietsch

im Fachbereich Physik der
Freien Universität Berlin
eingereichte Dissertation

—

Max-Born-Institut Berlin

September 2015

1. Gutachter: Prof. Dr. Martin Weinelt

2. Gutachter: Prof. Karsten Horn PhD

3. Gutachter: Prof. Dr. Alexander Lichtenstein (Universität Hamburg)

Tag der Disputation: 15. Dezember 2015

Abstract

We investigate the magnetization dynamics of the rare earth metals gadolinium (Gd) and terbium (Tb). To this end we perform IR pump and XUV probe experiments where we follow the evolution of the exchange-split valence band-structure which is a measure of the short-range magnetic order of the itinerant 5d6s electrons. In addition, the intensity and binding energy of the occupied surface state is surveyed as well as the magnetization of the 4f core level. The captured states determine the rich magnetic phenomena of the lanthanides and – upon laser excitation – we find distinct dynamics in all the observed states, revealing a highly perturbed magnetic system far from equilibrium. In particular Gd shows distinct dynamics with a fast response of the minority bulk band which increases its occupation as the majority surface state depletes. This surface to bulk electron redistribution is driven by electron-magnon and electron-electron exchange scattering. As a consequence we find that this process depends on the initial sample temperature, as it determines the polarization and thus the availability of the minority bulk band as a decay channel for the majority surface state electrons. The somewhat slower majority bulk band shows a response that is delayed by half a picosecond and follows the decay of the electron temperature which indicates a demagnetization driven by Elliot-Yafet type scattering. The overall timescale of the valence band dynamics depends, apart from the initial sample temperature, on the absorbed pump fluence. The average time constant of the Gd 5d6s demagnetization, as indicated by the collapse of its exchange splitting, is on the order of 0.8 ps. In contrast, the localized 4f electrons react much slower and show a time constant of $\sim$14 ps as measured by magnetic linear dichroism. This remarkable difference demonstrates a perturbation even beyond the strong intra-atomic exchange interaction which – thus far – was believed to act on a timescale of a few femtoseconds. In fact, the slow demagnetization of the 4f system indicates that it is almost exclusively driven by phonon-magnon scattering. These findings are in line with the Tb response where a strong spin-lattice coupling keeps the magnetic system relatively close to equilibrium. All these results are reproduced by orbital-resolved spin-dynamic simulations coupling 5d and 4f spins to an electron and phonon heat bath.

In conclusion we show that laser driven demagnetization drives Gd out of magnetic equilibrium with distinct timescales for the itinerant and localized electrons. The intra-atomic exchange is thereby overpowered on a timescale of tens of picoseconds, magnetic equilibrium is finally established via spin-lattice relaxation. In Tb this relaxation acts on the ultrafast timescale due to a strong 4f coupling to the lattice, keeping the magnetic system close to equilibrium at all times.

Kurzfassung

Ziel dieser Arbeit ist die Untersuchung der elementaren Prozesse die zur laserinduzierten Demagnetisierung in den Lanthanidmetallen Gadolinium (Gd) und Terbium (Tb) führen. Zu diesem Zweck wurden Zeit- und Winkelaufgelöste Photoelektronenspektroskopie-Experimente durchgeführt, wobei die für den Magnetismus verantwortlichen Zustände vermessen wurden. Zeitgleich mit der Austauschaufspaltung der delokalisierten Valenzelektronen wurde auch die Polarisation des 4f Rumpfniveaus mittels magnetischem Lineardichroismus vermessen was einen umfassenden Einblick in intra- und interatomare Prozesse ermöglicht. Nach der Anregung durch einen infraroten Laserpuls zeigen alle beobachteten Zustände unterschiedliche Dynamiken was eine starke Störung des magnetischen Systems, fern des Gleichgewichtszustandes, bedeutet. Insbesondere Gd zeigt unterschiedliche Zeitskalen in der Dynamik. Wir beobachten nach der Anregung eine schnelle Verschiebung des 5d6s Minoritätsvalenzbandes hin zu höheren Bindungsenergien der eine instantane Entvölkerung des Majoritäts-Oberflächenzustandes vorausgeht. Da das Minoritätsvalenzband die Fermikante schneidet, deutet dieses Verhalten auf eine Ladungsumverteilung hin welche durch Elektron-Elektron und Elektron-Magnon Streuung verursacht wurde. Da die anfängliche Polarisation der Bänder von der Temperatur abhängt, erhöht sich bei steigender Temperatur auch der Streuquerschnitt vom Majoritäts-Oberflächenzustand in das Minoritätsvalenzband. Das im Vergleich langsamere Majoritätsvalenzband zeigt eine um eine halbe Picosekunde verzögerte Reaktion und folgt im Wesentlichen der Relaxation der heißen Elektronen, was ein starkes Indiz für eine Demagnetisierung über Elliot-Yafet artige Elektron-Phonon Streuung ist. Die mittlere Demagnetisierungszeit des Valenzbandsystems, welche üblicherweise durch die Austauschaufspaltung gemessen wird, beträgt dabei 0,8 ps in Gd. Im Gegensatz dazu reagieren die lokalisierten 4f Elektronen in Gd wesentlich langsamer und zeigen eine Demagnetisierungs-Zeitkonstante von 14 ps. Dies ist insofern bemerkenswert, da bisher angenommen wurde, dass die starke intraatomare Austauschwechselwirkung innerhalb von wenigen Femtosekunden zu einem magnetischen Gleichgewichtszustand führt. Tatsächlich aber scheint die Demagnetisierung des 4f Zustandes beinahe ausschließlich durch gewöhnliche Spin-Gitter Wechselwirkung verursacht zu werden. Diese Interpretation wird auch dadurch gestützt, dass in Tb, durch die starke Kopplung der 4f Elektronen an das Gitter, die magnetischen Subsysteme während der Demagnetisierung größtenteils im Gleichgewicht bleiben. Diese Beobachtungen können durch orbitalabhängige Spindynamik-Simulationen innerhalb eines erweiterten Dreitemperaturmodells reproduziert und erklärt werden.

Contents

List of used symbols and abbreviations

List of symbols

Vectors and vector-operators are printed in bold in this thesis for better clarity

$\hbar = h/(2\pi)$	reduced Planck constant
e	electron charge
c	speed of light
k_B	Boltzmann constant
m_e	rest mass of the electron
m^*	effective mass of the electron in the solid
g_J	Landé factor of the electron in a solid
μ_B, μ_b	Bohr magneton, reduced magneton $\mu_b = \mu_B/\hbar$
$\gamma_s = g_s\mu_b$	gyromagnetic ratio of an electron spin
U_p	pondermotive potential
ϕ	work function, also known as surface potential
E_{Ph}, $\hbar\omega$	photon energy
E_F	Fermi level
E_{vac}	vacuum level
E_b	binding energy of the electron
T_C	Curie temperature
T_N	Néel temperature
$\boldsymbol{k}$	wave vector of the electron
$k_\perp$	wave vector perpendicular to the sample surface
$\boldsymbol{k}_\parallel$	wave vector parallel to the sample surface
$\boldsymbol{k}^{in}$	wave vector in the sample
$\boldsymbol{k}^{ex}$	wave vector in vacuum
J	coupling constant
J_{ex}	exchange integral
$\boldsymbol{S}$	electron spin operator
$\boldsymbol{L}$	orbital angular momentum operator
$\boldsymbol{J}$	total momentum operator
$\mathcal{H}$	Hamiltonian

List of abbreviations

3TM	three-temperature model of magnetism
AC	autocorrelation
ARPES	angle-resolved photoemission spectroscopy
CW	continuous wave
E3TM	extended three-temperature model
EDC	energy distribution curve
EY	Elliott-Yafet
FWHM	full width at half maximum
Gd	gadolinium
hcp	hexagonal close packing
HHG	high harmonic generation
IR	infra red
LEED	low-energy electron diffraction
LLG	Landau-Lifshitz-Gilbert
M3TM	microscopic three-temperature model
MBE	molecular beam epitaxy
MA	magnetic anisotropy
MCA	magnetocrystalline anisotropy
MCD	magnetic circular dichrosim
MD	magnetic dichroism
MLD	magnetic linear dichroism
MOKE	magneto-optic Kerr effect
Nd:YAG	neodymium-doped yttrium aluminium garnet
RKKY	Ruderman-Kittel-Kasuya-Yosida
SCC	space-charge cloud
SCS	space-charge shift
SOC	spin-orbit coupling
Tb	terbium
Ti:S	titanium-doped sapphire crystal
TM	transition metal
UHV	ultra high vacuum, $p < 10^{-10}\,\mathrm{mbar}$
QMS	quadrupole mass spectrometer
RE	rare earth
XC	cross-correlation
XMCD	x-ray magnetic circular dichroism
XPS	x-ray photoelectron spectroscopy
XUV	extreme ultraviolet radiation, $\hbar\omega = 10 - 124\,\mathrm{eV}$

Ch.	Chapter
Eq.	Equation
Fig.	Figure
Ref.	Reference

Chapter 1

Introduction

> *"The essence of magnetization is angular momentum. The key issues in magnetization dynamics are therefore the processes underlying the change of angular momentum."* – J. Stöhr and H.C. Siegmann [1]

Today laser-driven, ultrafast magnetization dynamics is an active field of research motivated by both, the technological importance as well as the provided insights into the involved physics. It started out in the 90s with the pioneering work of Vaterlaus *et al.* [2] who investigated the spin-lattice relaxation time in Gd using two synchronized pulsed lasers in an pump-probe arrangement. The idea behind their experiment is that the laser pulse only heats the electron system and leaves the spins unchanged. Subsequent electron-phonon relaxation then heats the lattice within 1 - 2 ps. Equilibrium between the spin system and the lattice is then established via phonon-magnon scattering [3]. The timescale they found for this process is 100 ± 80 ps in Gd. Following this experiment it was shown by Beaurepaire *et al.*, that demagnetization can even take place on sub-picosecond timescales [4]. In particular they investigated Ni where they found the spin temperature exceeding the heating of the lattice during ultrafast demagnetization. This can not be explained by ordinary phonon-magnon coupling and rises the question which underlying process is responsible for this ultrafast transfer of angular momentum.

In the following years the field of ultrafast magnetization dynamics grew with many theoretical contributions attempting to explain the fast dynamics in magnetic metals. Among the suggested processes were:

- Photon-magnon interaction, i.e., direct spin flips in the vicinity of the laser field via or beyond spin-orbit interaction [5–7] and magnon excitations through THz emission [8]. These processes, however, contribute only little to the overall dynamics and are commonly neglected [9].

- Electron-magnon scattering [10], where the angular momentum conservation is ensured by spin-orbit coupling, i.e., a proposed ultrafast transfer of angular momentum form the spin to the orbital system with subsequent transfer to the lattice.

- Electron-electron Coulomb scattering [11] which acts on the same ultrafast timescale than the electron-magnon interaction.

- *Elliott-Yafet* (EY) scattering [12–14] which is an electron-phonon mediated spin-flip scattering and relies, like the above processes, on spin-orbit interaction [15, 16].

- Superdiffusive spin transport [17] which explains the dynamics in terms of spin currents out of the probed region; a process that has its origin in the spin-dependent mean free path of the electrons.

Out of these processes, EY-scattering is often regarded as the most promising candidate to explain ultrafast demagnetization [18]. Contrary to ordinary spin-lattice relaxation, EY-like demagnetization depends not solely on the temperature of the lattice, but includes the temperature of the electrons as well, since they both determine the spin-flip scattering probability. With such an electron-phonon-mediated spin-flip process it is possible to explain many of the experimental observations [14]. Nevertheless it seems unlikely that only one process causes the variety of the observed phenomena. It is therefore not surprising, that also combinations of the above mechanisms were used to explain the dynamics [19]. Beside these microscopic processes, additional correlation effects, like the influence of the transient band structure, play a role during demagnetization [20].

In parallel with the theoretical progress numerous experimental contributions comprising various different time-resolved techniques[1] have contributed to the understanding of magnetization dynamics. In particular, the discovery of magnetization reversal upon fs laser excitation is a milestone towards the realization of magneto-optical storage devices [21]. The effect was found in an GdFeCo ferrimagnet were the *all-optical magnetic switching* (AOS) is driven by the angular momentum exchange between the circularly polarized light of a pulsed laser and the magnetic system of the sample, which implies direct photon-magnon interaction. Therefore it was surprising when Radu *et al.* published results in 2011 where they showed AOS with linearly polarized light on the same system, indicating that the driving force thereby is the internal coupling of the magnetic sublattices of *rare earth* (RE) and *transition metal* (TM) as they show transient ferromagnetic exchange in the process [22]. These observations made it imperative to distinguish between the different sublattices as well as the itinerant and localized electrons of the rare earth [23]. The internal coupling processes during demangetization of the rare earth are thereby not completely understood.

Our goal is to further clarify this issue by examining the role of inter- and intra-atomic exchange, the influence of the spin-lattice coupling, and the role of the different states that are involved in the magnetization dynamics. To this end we build a unique high-order harmonic setup to

[1] Such as m-SHG, MOKE, (X)MCD, (X)MLD, (Sr-)PES, PEEM, RIXS, RXD, ISHE, NRS, and THz-S, all performed in a pump-probe arrangement. The examined systems range thereby from pure transition metals to rare earth magnets as well as layered systems, alloys, magnetic clusters and oxides, Heusler alloys and many more.

conduct time- and angle-resolved photoelectron spectroscopy experiments comparing Gd and Tb thin films. With this novel approach it is possible to measure for the first time the transient, exchange split, valence band structure of the itinerant electrons in parallel with the polarization of the localized 4f electrons which is captured by magnetic linear dichroism. This way we are able to obtain nearly full information[2] of the distinct magnetic subsystems in Gd and Tb.

1.1 Outline

We start with a short introduction into the basic characteristics of the studied lanthanides to set the stage for the following studies. Some of the more important properties are summarized in Table 1.1. Before we come to the actual experiments we will recall the theoretical foundations in Ch. 2 starting with the basic concepts of magnetism (in particular exchange) followed by some common theories of ultrafast demagnetization that are needed for the classification of our work. In Ch. 3 we introduce the basic concepts of the experimental methods that are used. We specially emphasize the section about atomic and diffraction dichroism (Ch. 3.3). The actual apparatus for the time- and angle-resolved photoelectron spectroscopy is described in Ch. 4 with focus on the unique setup for high-order harmonic generation. Here we will also have a look at the problems that come with low repetition fs-XUV spectroscopy and discuss, in depth, IR and XUV space-charge effects. The chapter ends with a section about sample preparation, were Gd and Tb thin film epitaxy and their common impurities are examined.

Chapter 5 and 6 are the heart of this thesis. Here the data of the itinerant and localized electron dynamics are presented and interpreted. Starting with the valence band system we have a look at distinct band dynamics comparing laser-driven dynamics with static temperature-dependent measurements. We prove a residual exchange splitting in Gd above the Curie temperature and have a look at the fluence and temperature dependence of the dynamics. Comparing Gd and Tb we will discuss different proposed models of demagnetization and give an interpretation of our experimental data. Following the itinerant dynamics in Ch. 5 we concentrate on the polarization of the localized electrons in Ch. 6. Thereby we compare our findings with up to date results from other techniques and discuss them within an extended three-temperature model.

In the course of this work several articles have been published which are listed on page 105 and referred to as [I - VII] throughout this thesis. Note that Ch. 3.1 and 4.3 are revised versions of the corresponding chapters in the authors diploma thesis.

[2] Within our experiment we cover all relevant states, but have no direct information about the spin polarization. See discussions in Ch. 5.1.3 and 6.1.4.

1.2 Basic properties of Gd and Tb.

The rare earths Gd and Tb crystallize in a *hexagonal close-packed* (hcp) lattice structure. As lanthanides they are sometimes called 4f-transition metals which refers to Madelungs's rule that predict a successive filling of the inner 4f shell from the first lanthanide, lanthanum, with zero to lutetium with fourteen 4f electrons. As neighbors in the periodic table (atomic numbers 64 and 65), Gd and Tb metal differ thus mainly in the electron configuration of the 4f core level which, in the case of Gd, is exactly half filled. Tb has one additional 4f electron and thus unlike Gd a large angular orbital momentum (Gd 4f: $S = 7/2$, $L = 0$; Tb 4f: $S = 3$, $L = 3$). Both metals, however, have very similar chemical properties as a result of the identical electron configuration of the outer 5d6s shells[3]. The 5d6s valence electrons hybridize and form bands. These bands show significant s-like character at the Γ point [24] but are overall dominated by the 5d density of states [25], that is why some authors refer to them simply as 5d bands [26]. The magnetic moment per atom is remarkably large for both elements. In Gd the 4f spins contribute with $7\,\mu_B$ and intra-atomic exchange leads to a polarization of the 5d6s electrons which contribute an additional $0.63\,\mu_B$. In Tb we have only $6\,\mu_B$ from unpaired spins but additional $3\,\mu_B$ arising from the angular orbital momentum of the eighth 4f electron. The 5d6s electrons contribute here with only $0.33\,\mu_B$ since the polarization scales with the spin rather then the magnetic moment of the 4f system [27, 28]. This makes Gd and Tb ideal candidates for comparing experiments regarding the role of angular orbital momentum in magnetization dynamics.

The hcp structure of Gd and Tb leads to a hexagonal Brillouin zone for those materials. Fig. 1.1 b) shows such a Brillouin zone with marked high symmetry points. A special feature of the hcp structure is the existence of two sublattices in the (0001) direction (the primitive unit cell includes two atoms). These sublattices seem to stretch the Brillouin zone by a factor two[4] along $k_\perp$. To take this into account it is common to add an index to distinguish between Γ_1 and Γ_2. The electronic structure at this Γ points are quite different, we speak of Δ_1- and Δ_2-like bands whether they are close to the Γ_1 or the Γ_2 point. Fig. 1.1 c) shows this on the

[3] The bulk electron configuration is given by Gd: $[Xe]4f^7(5d6s)^3$ and Tb: $[Xe]4f^8(5d6s)^3$.

[4] The expected size of the Gd Brillouin zone (Γ to Γ) is $2k_{\Gamma-A} = 2\pi/c = 1.08\,\text{Å}^{-1}$. But with the second sublattice at $c/2$ the effective Brillouin zone is $k_{\Gamma_1-\Gamma_1} = 2.16\,\text{Å}^{-1}$. Such a stretching results in another spin-like quantum number for the electrons which describes the additional degree of freedom to be in one of the two sublattices. This pseudo spin has to be conserved in the photoemission process [31], which leads to a $k_\perp$ selective excitation. This can be understood if we keep in mind that the detected final state has to contain plane waves that travel in the direction of the surface vector. This plane waves have to be invariant under space group transformation of the lattice [32]. A simple point group symmetry will not affect the transition rules, but a transformation between the sublattices has to include a translation of $c/2$ in (0001) direction. This is equivalent to a change of the photoemission energy for the final state and can be described by a complex phase factor α in the corresponding space group transformation operator [32]:

$$\alpha = \exp\left(i\pi k_\perp \frac{c}{2\pi}\right) = \exp\left(i\pi \frac{c}{z}\right)_\perp$$

its projection on the real axis gives the symmetry [29]. A positive real part leads to Δ_1 like bands and a negative real part to Δ_2 like bands near Γ.

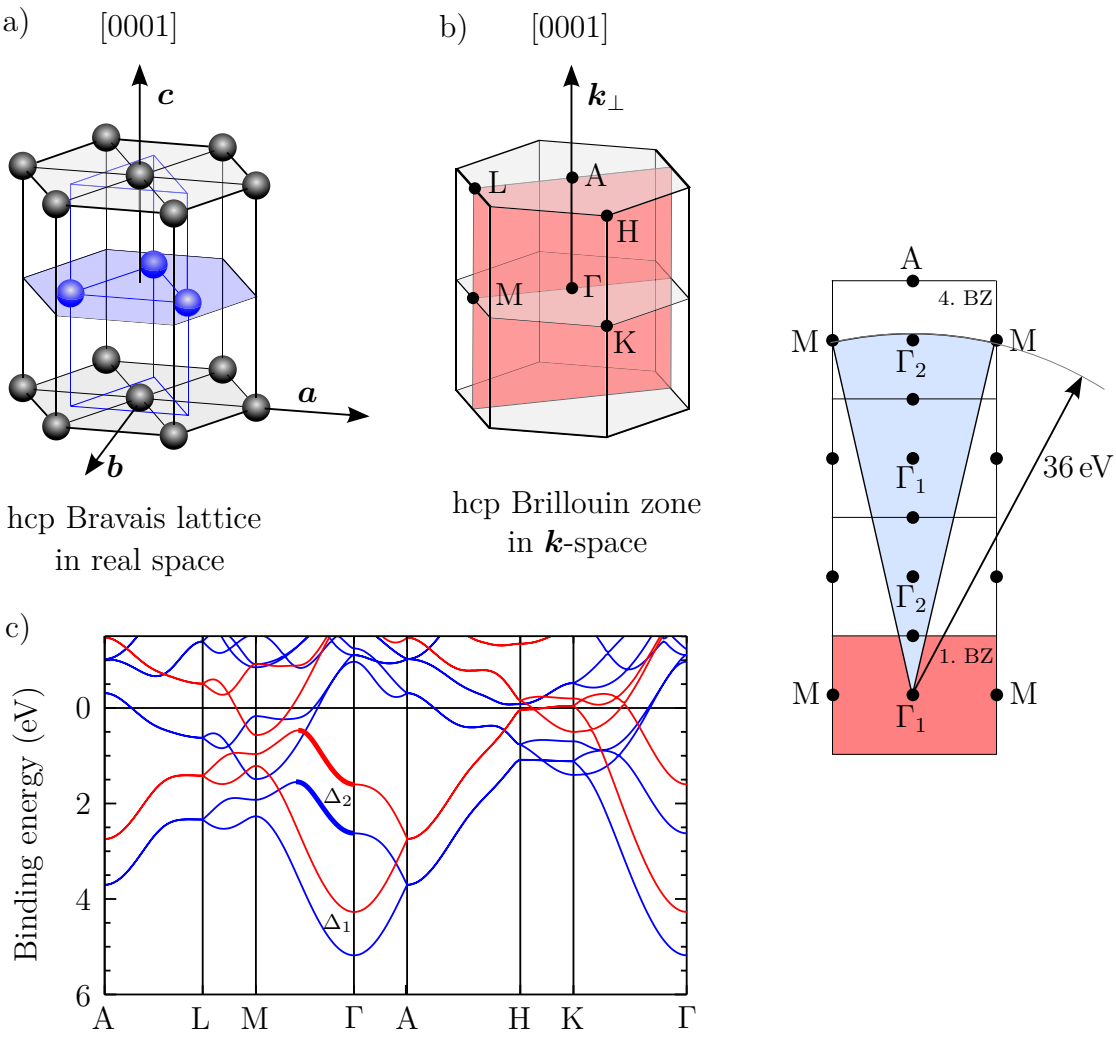

Figure 1.1: Structure of Gd and Tb in real and k-space. *(Not to scale)* ***a)*** *The hcp lattice structure of Gd and Tb with ABA stacking. If grown on a W(110) substrate the (0001) direction will coincide with the surface normal.* ***b)*** *The corresponding Brillouin zone with marked high symmetry points. The highlighted plane can be scanned by variation of the probe photon energy (i.e.* $\boldsymbol{k}_\perp$*) and rotation of the sample in Γ-M direction. In our experiment we probe* Γ_2 *in the 4th Brillouin zone using 36 eV photons (schematic sketch on the right). The used energy for Gd agrees well with the interpolated value of 35.5 eV from Ref. [29] and the measured value of* ≈ 35 *eV from Ref. [30].* ***c)*** *Bulk band structure calculations of Gd for minority (red) and majority (blue) electrons, from Ref. [24]. Highlighted are the exchange-split* Δ_2 *like valence bands which are probed in our experiment.*

example of the Gd band structure. For our studies we use photon energies around 36 eV which leads to a probing of the band structure at the Γ_2 point in the fourth Brillouin zone. The resolvable angle is thereby determined by the measurement geometry, for the here presented data we chose the Γ - M direction.

Table 1.1: Some important properties of Gd and Tb metal.

Structural properties

	Gd	Tb	Ref.
Lattice const.	$a = 3.625\,\text{Å}$	$a = 3.590\,\text{Å}$	[33]^b[34]^b
		$b = 6.260\,\text{Å}$	[-] [34]^b
	$c = 5.796\,\text{Å}$	$c = 5.714\,\text{Å}$	[33]^b[34]^b
distance $\Gamma-$ K	$1.00\,\text{Å}^{-1}$	$1.15\,\text{Å}^{-1}$	calc.
distance $\Gamma-$ M	$0.87\,\text{Å}^{-1}$	$0.88\,\text{Å}^{-1}$	calc.
distance $\Gamma-$ A	$0.54\,\text{Å}^{-1}$	$0.55\,\text{Å}^{-1}$	calc.

Magnetic properties

	Gd	Tb	Ref.
Curie temp.	$T_C = 285\,\text{K}$	$T_C = 223\,\text{K}$	[35]*[36]*
	$T_C = 293\,\text{K}$		[37]^b[-]
Neel temp.	-	$T_N = 233\,\text{K}$	[-] [36]*
magnetic moment	$\mu_{4f} = 7\,\mu_B$	$\mu_{4f} = 9\,\mu_B$	
	$\mu_{5d6s} = 0.63\,\mu_B$	$\mu_{5d6s} = 0.33\,\mu_B$	[38]^b_z[39]^b_z
4f $\lvert i\rangle$	$S = 7/2, L = 0$	$S = 3, L = 3$	
term symbol	$^8\text{S}_{7/2}$	$^7\text{F}_6$	
coupling param.	$J_{4f-5d} = 130\,\text{meV}$		[23]^t[-]
	$J_{5d-5d} = 6\,\text{meV}$		[VI]^t[-]
anisotropy	$E_{MCA} = 0.03\,\text{meV}$	$E_{MCA} = 11\,\text{meV}$	[40]^b_z[41]^b_z
spin-orbit coupling	$71.2\,\text{meV}$	-	[40]^t[-]
VB exch. splitting	$0.89\,\text{eV}$	$0.78\,\text{eV}$	[42]*[42]*

Other properties

	Gd	Tb	Ref.
Electron config.	[Xe] 4f^7 $(5\text{d}6\text{s})^3$	[Xe] 4f^8 $(5\text{d}6\text{s})^3$	
de Gennes factor	$G = 15.75$	$G = 10.5$	
Lande factor	$g_J = 2$	$g_J = 1.5$	
work function	$\Phi_{(0001)} = 3.72\,\text{eV}$	$\Phi_{(0001)} = 4.95\,\text{eV}$	[43]*[44]
Annealing temp.	$T_A = 680\,\text{K}$	$T_A = 880\,\text{K}$	

* value for a 100 Å thin film on W at $\approx 90\,\text{K}$
^{b} the value for a bulk single crystal
^{t} theoretical value (0 K, bulk)
^{z} measured near 0 K
^{r} measured at room temperature = 300 K

Chapter 2

Theoretical considerations

2.1 Concepts of magnetism

Magnetism in solids is mainly a correlation phenomenon of electrons. The two most important features are the intrinsic magnetic moment of the electron and the angular orbital momentum of its atomic state. In a classical picture both contributions are the result of the moving electron charge, thus the names: spin and orbital. In truth, classical concepts can only explain macroscopic features of magnetism like the shape anisotropy. To see this let us consider the magnetic dipole interaction of two electrons with parallel aligned spins. The magnetic dipole contribution to the energy of such a system depends on the distance r of the electrons:

$$E_{mag} = \frac{\mu_0 \mu_B^2}{2\pi r^3} \tag{2.1}$$

with μ_0 the magnetic permeability of free space and μ_B the Bohr magneton[1]. In gadolinium there are 7 unpaired electrons per atom which mainly contribute to magnetism. The inter-atomic distance to the next nearest neighbor is 3.64 Å giving an energy of 0.1 meV and thus a predicted ordering temperature[2] from magnetic dipole interaction of 1.3 K. In contrast the measured Curie temperature of Gd is 293 K. Ferromagnetism therefore has to have a different origin and solid state magnetism, at its heart, is a purely quantum mechanical effect stemming from fundamental symmetry principles which we will discuss next.

2.1.1 Exchange interaction

Electrons are elementary particles and as such indistinguishable. As a result a physical state remains the same under the exchange of two electrons. This means

[1] The connection between the spin $\boldsymbol{s}$ and the magnetic moment $\boldsymbol{\mu}$ of an electron is given by $\boldsymbol{\mu} = \boldsymbol{s} \cdot ge/(2m_e)$ with g the Landé factor ($g \approx 2$ for a free electron), e its charge, and m_e its mass.

[2] Since the calculated energy is positive, the dipoles considered would align antiparallel.

for the wave function of two electrons, that $|\Psi(1,2)|^2 = |\Psi(2,1)|^2$ and thus that they can only differ by a phase vector $\Psi(1,2) = e^{i\alpha}\,\Psi(2,1)$. Assuming that a second exchange of the two electrons (that is the change back) will necessarily result in the original wave function the phase vector $e^{i\alpha}$ has to be either $+1$ or -1, i.e., the wave function has to be either symmetric $\Psi(1,2) = \Psi(2,1)$ or antisymmetric $\Psi(1,2) = -\Psi(2,1)$ under exchange. Experimentally it has been found that electrons only have antisymmetric wave functions[3]. For a two electron system the wave function is thus an antisymmetric linear combination of the two one-electron functions $\Psi_{12} = 1/\sqrt{2}\,[\Psi_i(1)\Psi_j(2) - \Psi_i(2)\Psi_j(1)]$. As a direct consequence two electrons can not occupy the same state since $\Psi_{12} = 0$ for $i = j$ (Pauli principle).

The total wave function of an electron can often be expressed as the product of a spatial and a spin part $\Psi(r,s) = \phi(r)\chi(s)$ with the spin component fully described by the spin quantum number and its projection $\chi(s) = |S, m_s\rangle$. For a two electron system the total wave function is only antisymmetric if exclusively one, the spin or the spatial wave function is antisymmetric. For a symmetrical spatial part this implies the following solution for the corresponding spin component:

$$|S, m_s\rangle = |0,0\rangle = \frac{1}{\sqrt{2}}\,(\uparrow\downarrow - \downarrow\uparrow) \tag{2.2}$$

This linear combination of the single electron spin eigenstates $\uparrow$ and $\downarrow$, is called the singlet spin state. Analogue for an antisymmetric spatial wave function we get a triplet spin state:

$$|1,1\rangle = \uparrow\uparrow \tag{2.3}$$

$$|1,0\rangle = \frac{1}{\sqrt{2}}\,(\uparrow\downarrow + \downarrow\uparrow) \tag{2.4}$$

$$|1,-1\rangle = \downarrow\downarrow \tag{2.5}$$

The spins of electrons only contribute to the atomic magnetism, if the total spin is non-vanishing $S \neq 0$, i.e., in the case of symmetric spin wave functions. The spin singlet state $|0,0\rangle$ is therefore nonmagnetic due to its antisymmetric spin wave function. In general for any electron system there is magnetism when the spatial wave function is symmetric, i.e., when the Coulomb repulsion between the electrons overcomes the single electron energy defined by the attraction from the core. This difference in energy, between a parallel and antiparallel alignment, is called exchange energy.

Intra-atomic exchange: The intra-atomic exchange between electrons of the same atom is the reason why its degenerate energy levels are filled according to

[3] In general, according to the spin statistics theorem, all particles with half integer spins (Fermions) have antisymmetric wave functions and particles with integer spins (Bosons) have symmetric wave functions.

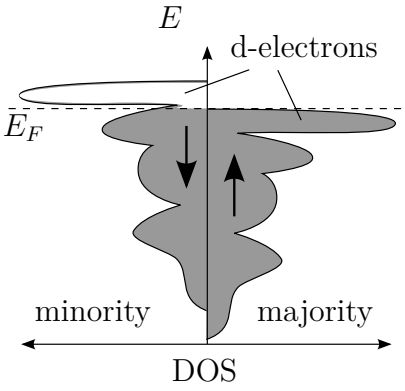

Figure 2.1: Schematics of the density of states of the minority and majority electrons in a transition metal. *The weakly dispersing d-bands at the Fermi level have a high DOS, leading to magnetism according to the Stoner criteria (Eq. 2.18). The origin of the energetic splitting is the exchange interaction and its size is given by the coupling parameter J and is usually on the order of 1 eV.*

Hund's rule of maximum multiplicity. The size of this energy is generally in the order of a few electron volts. In the specific case of the 4f core level in gadolinium one needs 12 eV for the transition to an antisymmetric spin wave function for one electron. The more interesting exchange between the 4f and 5d electrons is with ~ 100 meV a lot weaker [23, 45].

Inter-atomic exchange of itinerant electrons: Magnetism in condensed matter is the result of exchange between electrons of neighboring atoms. These electrons form energy bands according to Bloch's theorem. In metals inter-atomic exchange is stronger because of the mobile conduction electrons. It is on the order of 10 meV [46] and leads, together with the intra-atomic exchange, to a spin polarized splitting of the valence band-structure, the so-called exchange splitting (ΔE_{ex}). The itinerant $(5d6s)^3$ electrons in Gd and Tb show such a splitting. Its size is with 0.91 eV (Gd) and 0.85 eV (Tb) comparable to values found for the 3d transition metals Fe, Co, Ni with $\Delta E_{ex} \approx 2.2, 1.8, 0.25$ eV, respectively [42, 47].

The magnetism of transition metals are often described within the free electron model. According to the discussion above one-electron energies can be lowered by exchange which can favor parallel spin alignment due to the reduced Coulomb repulsion originating from the collective anti-symmetric spatial wave function. Since the exchange parameter J is on the order of 1 eV, ferromagnetism can only occur when the metal has a high density of states at the Fermi level, i.e. when the spin-dependent energy shift leads to a sufficient difference in occupation as shown in Fig. 2.1. The formal criteria was first given by Stoner [48] and shall be recalled in the following. In a simple free electron picture the energy is reduced, the more electrons of the system share a symmetric spin wave function. Renormalization of these energies satisfies the condition [49]

$$E_\uparrow(\boldsymbol{k}) = E(\boldsymbol{k}) - J\frac{N_\uparrow}{N} \quad \text{and} \quad E_\downarrow(\boldsymbol{k}) = E(\boldsymbol{k}) - J\frac{N_\downarrow}{N} \tag{2.6}$$

with $N_{\uparrow/\downarrow}$ the number of up and down spins respectively with $N = N_\uparrow + N_\downarrow$. The dispersion relation $E(\boldsymbol{k})$ is given for the single electron case; $E_{\uparrow/\downarrow}(\boldsymbol{k})$ denotes it for up/down electrons whose energy is reduced through exchange. We can rewrite

Eq. 2.6 and get:

$$E_{\uparrow/\downarrow}(\boldsymbol{k}) = E(\boldsymbol{k}) \mp J\frac{N_\uparrow + N_\uparrow - N_\downarrow + N_\downarrow}{2N} \tag{2.7}$$

$$= E(\boldsymbol{k}) - \frac{J}{2} \mp \frac{J}{2}R \quad \text{with} \quad R = \frac{N_\uparrow - N_\downarrow}{N} \tag{2.8}$$

$$= \mathcal{E}(\boldsymbol{k}) \mp \frac{J}{2}R \tag{2.9}$$

with the effective one-electron energy $\mathcal{E}(\boldsymbol{k}) = E(\boldsymbol{k}) - J/2$. The system is ferromagnetic when $N_\uparrow \neq N_\downarrow$, i.e. when $R \neq 0$. The number of up/down electrons is given by the summation over the Fermi-Dirac distribution $f(\mathcal{E}(\boldsymbol{k})) \equiv f$:

$$N_{\uparrow/\downarrow} = \sum_k f_{\uparrow/\downarrow} = \sum_k \left[\exp\left(\frac{E_{\uparrow/\downarrow}(\boldsymbol{k}) - E_F}{k_B T}\right) + 1\right]^{-1} \tag{2.10}$$

with the equations above we get the following expression for the spin excess R:

$$R = \frac{1}{N}\sum_k \Bigg\{ \left[\exp\left(\frac{\mathcal{E}(\boldsymbol{k}) - RJ/2 - E_F}{k_B T}\right) + 1\right]^{-1} - \left[\exp\left(\frac{\mathcal{E}(\boldsymbol{k}) + RJ/2 - E_F}{k_B T}\right) + 1\right]^{-1} \Bigg\} \tag{2.11}$$

with the substitutions $x = (\mathcal{E}(\boldsymbol{k}) - E_F)/(k_B T)$ and $a = RJ/(2k_B T)$ we can rewrite R and find its Taylor series for small values of R:

$$R = \frac{1}{N}\sum_k [f(x-a) - f(x+a)] = \frac{2}{N}\sum_k \left[-a\partial_x f - \frac{1}{3!}a^3 \partial_x^3 f\right] \tag{2.12}$$

using the fact that

$$\partial_x f = \frac{\partial f}{\partial \mathcal{E}(\boldsymbol{k})}\frac{\partial \mathcal{E}(\boldsymbol{k})}{\partial x} = k_B T \partial_\mathcal{E} f \tag{2.13}$$

we can now rewrite R in the form of

$$R = -\frac{JR}{N}\sum_k \partial_\mathcal{E} f - \frac{J^3 R^3}{24N}\sum_k \partial_\mathcal{E}^3 f \tag{2.14}$$

$$R^2 \frac{J^3}{24N}\sum \partial_\mathcal{E}^3 f = -\frac{J}{N}\sum \partial_\mathcal{E} f - 1 \tag{2.15}$$

Since we know that the first derivative of the Fermi function is negative, and the third positive $[\partial_\mathcal{E} f < 0;\ \partial_\mathcal{E}^3 f > 0]$ we need:

$$-\frac{J}{N}\sum_k \partial_\mathcal{E} f > 1 \tag{2.16}$$

for $R \in \mathbb{R}$. For small temperatures the Fermi distribution can be approximated by the Heaviside step function hence its derivation by a delta distribution $\partial_\mathcal{E} f \to -\delta(\mathcal{E}(\boldsymbol{k}) - E_F)$:

$$-\frac{J}{N}\sum_k \partial_\mathcal{E} f = \frac{J}{N}\sum_k \delta(\mathcal{E}(\boldsymbol{k}) - E_F) = \frac{J}{N} N_{E_F} = JD(E_F) \tag{2.17}$$

with N_{E_F} the number of states at the Fermi level and $D(E_F)$ the relative spin density of these states. We therefore get the Stoner criteria for itinerant ferromagnetism:

$$JD(E_F) > 1 \tag{2.18}$$

For a Stoner ferromagnet equation 2.16 can be used to calculate the Curie temperature; the temperature broadened Fermi function leads to a reduced spin excess and thus to a breakdown of magnetism when the Stoner criterion is violated.

Inter-atomic exchange of localized electrons: Stoner's model explains the magnetism in transition metals like Fe, Co and Ni whose itinerant d electrons have a high DOS at the Fermi level. However, for the magnetism of rare earth elements like Gd and Tb the model fails. The reason for this is the localized character of the magnetic 4f state which leads to a general breakdown of free electron based theories. The high magnetic moment of the 4f electrons of Gd with $7\,\mu_b$ ($\mathrm{S}=7/2$, $\mathrm{L}=0$) and Tb with $9\,\mu_B$ ($\mathrm{S}=3$, $\mathrm{L}=3$) makes them perfect candidates for localized spin theories where especially Gd is an interesting case because of the vanishing angular orbital momentum. The interaction of localized spins are described following the approach by Heisenberg [50] using the Hamiltonian:

$$\mathcal{H} = -J \sum_{i,j} \boldsymbol{S}_i \boldsymbol{S}_j \quad \text{with} \quad i,j \text{ nearest neighbors} \tag{2.19}$$

where J is a constant and describes the average coupling between two neighboring spins. In a more realistic model this can be extended with a coupling parameter that dependents on the distance of the spins as well as their position in the lattice. In such a model $\mathcal{H}$ can be expressed by:

$$\mathcal{H} = -\frac{1}{2} \sum_{i,j} J_{ij}\, \boldsymbol{S}_i \boldsymbol{S}_j \qquad \text{with} \qquad J_{ij} = \frac{J_{ex} - CB^2}{1 - B^4} \tag{2.20}$$

With J_{ex} being the exchange integral, C the coulomb integral and B the overlap integral. The factor $1/2$ compensates the double summation in J_{ij}. The integrals are given in first order perturbation theory by:

$$J_{ex} = \langle \Phi_i(r_i), \Phi_j(r_j) |\, V(\boldsymbol{r}_{ij}) \,| \Phi_j(r_i), \Phi_i(r_j) \rangle \tag{2.21}$$

$$C = \langle \Phi_i(r_i), \Phi_j(r_j) |\, V(\boldsymbol{r}_{ij}) \,| \Phi_i(r_i), \Phi_j(r_j) \rangle \tag{2.22}$$

$$B = \langle \Phi_j | \Phi_i \rangle \tag{2.23}$$

With the potential $V(\boldsymbol{r}_{ij})$ describing coulomb repulsion between the electrons as well as attraction by the lattice. Note that for orthogonal states, e.g., different orbitals in the same atom, the overlap integral vanishes and $J_{ij} = J_{ex}$. On the contrary for a large overlap we see directly from 2.20 that the sign of J_{ij} becomes negative and the coupling is antiferromagnetic: a high overlap implies symmetric spatial wave functions. This direct exchange, however, can not describe the magnetism in the local moment ferromagnets Gd and Tb because the potential between 4f shells of neighboring atoms ($V_{4f}(\boldsymbol{r})$) is shielded by the valence electrons. These electrons though can mediate the exchange interaction which is described by a model that includes both localized and itinerant electrons as discussed in the following.

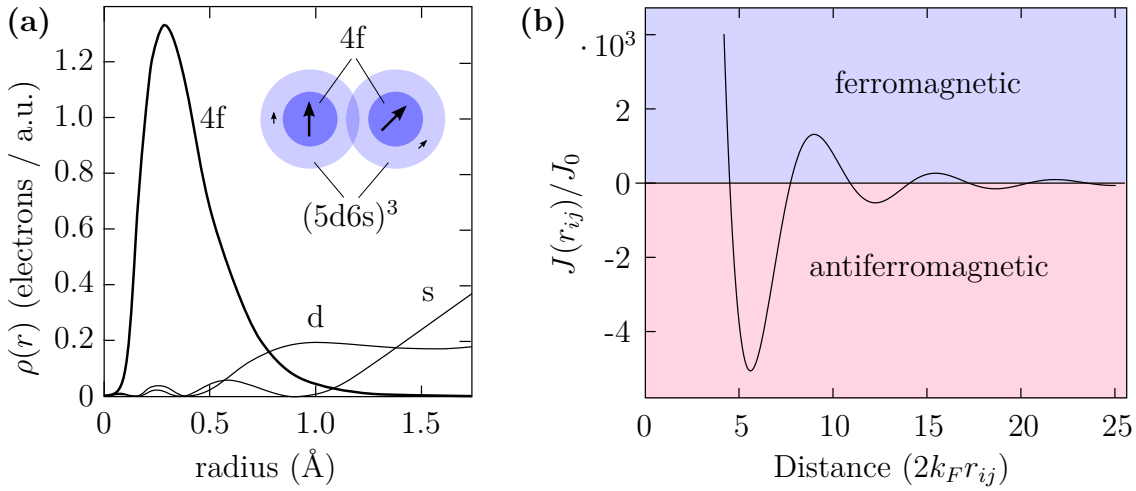

Figure 2.2: ***(a)****Calculated radial densities of the 4f state and the s- and d-like wave functions in Gd (adapted from ref. [51]). The inter-atomic distance is 3.64 Å; therefore the 4f orbital overlap of neighboring atoms is negligible and 4f interaction between different atoms has to be mediated via the much stronger 4f - $(5d6s)^3$ exchange.* ***(b)*** *The interaction parameter of indirect exchange. It describes the coupling between the localized spins and is given by Eq. 2.24. The sign depends on the inter-atomic distance, favoring alternating ferro- and antiferromagnetic coupling. This behavior is known as RKKY coupling or Friedel oscillations [52].*

Indirect exchange - the RKKY theory: As mentioned above, the magnetism in lanthanide metals is quite complicated, because on the one hand the origin of the magnetic moment is the partially filled 4f core level and on the other hand magnetic alignment is mediated through itinerant valence electrons. Figure 2.2 (a) shows the radial densities of the orbitals involved in the magnetism of gadolinium. A successful description of such an indirect exchange is the *Ruderman-Kittel-Kasuya-Yosida theory* (RKKY theory). It was originally developed by Ruderman and Kittel to describe the broadening of nuclear spin resonances in some systems [53]. The theory proposes an indirect exchange coupling of the nuclei via conduction electrons by second-order perturbation theory. It was then adopted by Kasuya [54] and Yosida [55] to suggest a similar coupling of the inner electron spins (here the 4f electrons in Gd and Tb) to the conduction electrons. As a result of the RKKY theory the Fermi surface plays an important role in the magnetic properties of the lanthanide metals. The coupling in this model is described by:

$$J(r_{ij}) = J_0 S_i S_j \frac{\sin(2k_F r_{ij}) - 2k_F r_{ij}\cos(2k_F r_{ij})}{(2k_F r_{ij})^4} \tag{2.24}$$

with J_0 an interaction coefficient which describes the coupling of the localized spins with the free electron gas. It dependents on the shape and size of the Fermi surface as well as the density of the itinerant electrons at the localized spins [56, 57]. As shown in Fig. 2.2 (b) $J(r_{ij})$ oscillates with the distance of the localized magnetic moments with a strong $1/r^3$ damping. The oscillation and the damping can be explained as a result of scattering and screening of the itinerant electrons [52].

2.1.2 Magnetic anisotropy

Spin-Orbit Interaction: Up to now we only discussed isotropic exchange of spins and we have neglected interaction with the lattice via *spin-orbit coupling* (SOC). SOC can favor certain magnetization directions, so called easy axis, as the lattice is not isotropic for orbitals with $L \neq 0$ leading to *magnetocrystalline anisotropy* (MCA). Anisotropies arising from these orbitals are dominated by single-ion contributions, only determined by the orientation of the atomic orbital in a lattice. That is why usually orbitals with $L = 0$ are neglected as their contribution to the MCA stems from two-ion effects such as anisotropic exchange or dipole-dipole interactions which is two to three orders of magnitude smaller. In Gd though these second order effects play an important role as they determine the easy axis due to lack of 4f orbital momentum. The interaction energy for SOC of a single atom is given by

$$E_{SOC} = \left(\frac{e}{m_e c}\right)^2 \frac{Z}{r^3} \boldsymbol{L} \cdot \boldsymbol{S} = \lambda_{SOC} \boldsymbol{L} \cdot \boldsymbol{S} \tag{2.25}$$

where Z is the atomic number and r the distance of the electron to the core. In a solid the symmetry of the crystal is usually included using a phenomenological description where the anisotropy is described in an expansion of the free energy F using spherical harmonics Y_l^m. For a hcp lattice it is convenient to use polar coordinates [58]:

$$F(\theta, \phi) = \sum_{l=2,4,6} K_l^0(T) Y_l^0(\theta, \phi) + K_6^6(T)[Y_6^6(\theta, \phi) + Y_6^{-6}(\theta, \phi)] \tag{2.26}$$

In this formula the strength of the anisotropy is represented by the coefficients K_l^m and the alignment by the normalized spherical harmonics. The uniaxial anisotropy (i.e. the anisotropy with respect to the $\boldsymbol{c}$-axis) is described by the terms with $m = 0$, thereby an alignment parallel to $\boldsymbol{c}$ is favored if $K_l^0 < 0$, otherwise with $K_l^0 > 0$ the anisotropy favors perpendicular alignment. The last term with K_6^6 describes the anisotropy within the basal plane and is proportional to $\sin^6(\theta)\cos(6\phi)$ reflecting the hexagonal crystal symmetry.

In Tb bulk samples uniaxial anisotropy dominates with positive $K_2^0 = 11\,\text{meV}$ [41] keeping the easy axis perpendicular to $\boldsymbol{c}$. The in-plane anisotropy is given by $K_6^6 = 0.06\,\text{meV}$ [59] favoring magnetization along the $\boldsymbol{b}$ axis (values measured at 4 K).

In a Gd bulk crystal the situation is different as the easy axis can point out of plane towards the $\boldsymbol{c}$ direction. The dominating anisotropy coefficients $K_2^0 = -11\,\mu\text{eV}$ and $K_4^0 = 9\,\mu\text{eV}$ [60] are of the same size, thus Gd bulk samples display a complicated temperature dependency with the easy axis pointing 45° off $\boldsymbol{c}$ at 100 K [61]. For thin Gd films ($< 350\,\text{Å}$) the magnetic anisotropy is dominated by stray fields and favors an in-plane magnetization.

Even though Gd and Tb are heavy elements (atomic number 64 and 65) it is known that SOC is relatively small so that LS coupling is a better approach than jj coupling [62].

Dipole-dipole interaction is the cause of the formation of magnetic domains and shape anisotropy to minimize the stray field. Magnetic domains are to be expected for thicker films to reduce the emerging field. For thin films however the low magnetic permeability of vacuum as well as of the tungsten substrate favors a single magnetic domain with in-plane magnetization. The driving force behind stray fields are dipole-dipole interactions which can be described by:

$$E = \frac{\mu_0}{4\pi r^3}\left(\boldsymbol{\mu}_1 \cdot \boldsymbol{\mu}_2 - \frac{3}{r^2}(\boldsymbol{\mu}_1 \cdot \boldsymbol{r})(\boldsymbol{\mu}_2 \cdot \boldsymbol{r})\right) \tag{2.27}$$

where $\boldsymbol{\mu}_1$ and $\boldsymbol{\mu}_2$ are the interacting magnetic moments separated by the distance $\boldsymbol{r}$. From this we see directly that the dipole-dipole energy is small at the atomic range if compared to exchange interaction but since it only decays with $1/r^3$ it can influence the long range magnetic order as seen, e.g., in thin films.

2.1.3 The Hamiltonian of the Gd and Tb spin system

It is common to use an Heisenberg approach to describe the spin Hamiltonian of lanthanides such as Gd and Tb. Such a treatment is well justified because of the localized character of the 4f electrons. As mentioned above inter-atomic exchange is mediated by the valence electrons, thus the interaction between lattice sites i and j can be expressed by:

$$\mathcal{H}_{5d-5d} = -\frac{1}{2}\sum_{\langle ij \rangle} J_{ij} \boldsymbol{S}_i^{5d} \cdot \boldsymbol{S}_j^{5d} \tag{2.28}$$

Where $\boldsymbol{S}_i^{5d}$ is the normalized 5d magnetic moment which represents the itinerant 5d6s spin system in this model and is expressed by a unit vector in the classical limit. Since we chose a localized spin model the 5d exchange parameter J_{ij} is constant and calculated to be 5.9 meV for Gd [VI]. The inter-atomic exchange in Tb should be of comparable size because the valence band system is not very different from Gd.

Analogue the intra-atomic exchange can be expressed by:

$$\mathcal{H}_{4f-5d} = -\sum_i J_{int} \boldsymbol{S}_i^{5d} \cdot \boldsymbol{S}_i^{4f} \tag{2.29}$$

The exchange parameter here was calculated to be $J_{int} = 130$ meV in Gd [23]. This value could be somehow different in Tb, because of the additional 4f electron. By adding uniaxial anisotropy, which is normally dominant in a hcp lattice we get a similar Hamiltonian as used by Wienholdt *et al.* to describe GdFe compounds [23]:

$$\mathcal{H} = -\frac{1}{2}\sum_{\langle ij \rangle} J_{ij} \boldsymbol{S}_i^{5d} \cdot \boldsymbol{S}_j^{5d} - \sum_i J_{int} \boldsymbol{S}_i^{5d} \cdot \boldsymbol{S}_i^{4f} - K^0 \sum_i (S_i^{5d})_z^2 \tag{2.30}$$

In Ch. 6 we present calculations which are based on this Hamiltonian to explain the distinct dynamics found in Gd.

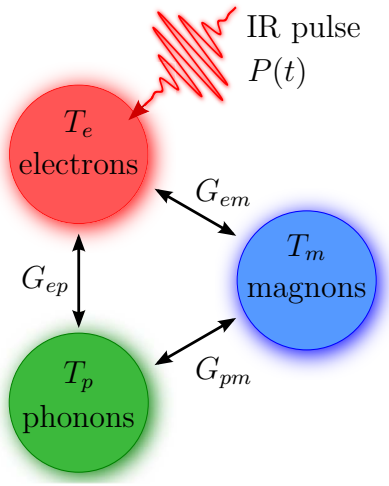

Figure 2.3: Three-temperature model of magnetism. *The three subsystems – electrons, phonons and magnons – have distinct temperatures which are coupled through the interacting constants G_{ep}, G_{em} and G_{pm} allowing heat transfer. Initially only the electron system is excited by the laser pulse $P(t)$.*

2.2 Theories of ultrafast demagnetization

2.2.1 Three-temperature model

In laser driven magnetization dynamics it is common to describe the sample-system in terms of three types of quasi-particles first spinless electrons, second phonons, and third magnons. Each quasi-particle system is denoted to a distinct temperature (T_e, T_p and T_m respectively). Within this model the interaction between the different heat baths is of interest.

When a metallic sample absorbs an IR laser pulse some electrons are lifted above the Fermi level. Assuming typical intensities we can neglect multi photon absorption and the wavelength of the driving laser determines the electrons that can be excited. In our case only states up to 1.6 eV binding energy are directly perturbed by the laser pulse. In good approximation the phonon and the magnon systems are unperturbed by the laser since direct spin flip processes are forbidden with linearly polarized light[4] and our elementary samples lack the electric dipole moment needed for a direct phonon excitation. Additionally the maximum possible magnon and phonon energies in Gd and Tb lie well below 30 meV [64–67] which is far from resonance with the laser field.

Immediately after excitation, it takes about 50-100 fs for the electronic system to equilibrate through electron-electron scattering and establish a defined temperature T_e [68]. At this time the lattice and the spin systems can still be considered cold. Some authors therefore define an initial state at t_0 with $T_e > T_p = T_m$ which does not take the actual absorption process of the pump pulse into account.

Coupling between the different heat baths are now described by a set of three simple rate equations [2, 4, 69, 70]:

[4] Zhang and Hübner proposed a direct spin-flip channel via spin orbit coupling in the vicinity of the laser field to explain ultrafast demagnetization in nickel [5]. Later it was shown by Stamm *et al.* [63] that this effect is not responsible for the demagnetization, but a fast spin-lattice coupling. We believe that such direct spin-flips do not play a significant role in our experiment as the main magnetic states react not during, but after excitation.

$$C_e(T_e)\,\partial_t T_e = G_{ep}(T_p - T_e) + G_{es}(T_m - T_e) + P(t) \tag{2.31}$$
$$C_p(T_p)\,\partial_t T_p = G_{ep}(T_e - T_p) + G_{sp}(T_m - T_p) \tag{2.32}$$
$$C_s(T_m)\,\partial_t T_m = G_{em}(T_e - T_m) + G_{sp}(T_p - T_m) \tag{2.33}$$

With the laser excitation $P(t)$ and the electron, phonon and magnetic heat capacities C_e, C_p and C_m. These equations allow energy and momentum transfer which leads to converging temperatures between the subsystems. The timescale on which the equilibration takes place is given by the interaction constants G_{ep}, G_{em} and G_{pm}. Since the three-temperature model is phenomenological these constants are normally free parameters in a fit to the data.

Microscopic three-temperature model (M3TM) In 2010 Koopmans *et al.* published an article with a microscopic interpretation of the three-temperature model [14]. They propose an Elliott-Yafet like spin-flip to be responsible for ultrafast demagnetization. In this model the spin-flip occurs during electron-phonon scattering in which angular momentum is transfered from the spin system to the lattice. It can be shown, that such a process scales with the spin-orbit coupling of the involved states [15]. Within the M3TM the differential equations given above are modified to describe the magnetization dynamics. The first two are now given by:

$$C_e(T_e)\,\partial_t T_e = g_{ep}(T_p - T_e) + \partial_z(\kappa \partial_z T_e) \tag{2.34}$$
$$C_p\,\partial_t T_p = g_{ep}(T_e - T_p) \tag{2.35}$$

The model does not cover the absorption process but starts with the already hot electrons. Equation 2.34 therefore lacks the term for the laser excitation, instead a different term is introduced describing heat diffusion of hot electrons into the substrate (with κ being the thermal conductivity of the electrons). The electron-phonon coupling g_{ep} in this model is now given by microscopic parameters (see supplementary information of Ref. [14] for details). To describe the spin excitations they chose a mean-field Weiss model:

$$\partial_t m = Rm\frac{T_p}{T_C}\left[1 - m\coth\left(m\frac{T_C}{T_e}\right)\right], \quad \text{with} \quad m = \frac{M(T)}{M(0)} \tag{2.36}$$

This has the consequence that the spin specific heat is not taken into account and thus also missing in Eq. 2.34 and 2.35. Such an approximation is reasonable for 3d magnets where the magnetic moment per atom is relatively small but invalid for Gd and Tb where the spin heat capacity exceeds the phonon contribution near the Curie temperature [71, 72].

The factor R in Eq. 2.36 holds material-specific parameters like the spin-flip probability a_{sf}, the atomic volume V_{at}, the Debye energy E_D, the magnetic moment

of the atom μ_{at} and the Curie temperature T_C:

$$R = 8 k_B \mu_B \frac{a_{sf} g_{ep} T_C^2 V_{at}}{\mu_{at} E_D^2} \tag{2.37}$$

Within this model it is possible to explain the magnetization dynamics in elementary 3d magnets and the Gd measurements that were published at that time. In Ch. 5 we will see that the M3TM can not solely explain demagnetization dynamics in Gd and Tb.

Extended three-temperature model (E3TM) In this section we will discuss an "extended" version of the three-temperature model. It was developed in 2013 by Wienholdt *et al.* to describe magnetization dynamics in complex spin systems such as alloys [23]. The advantage of this model is that it can distinguish between magnetism from different orbitals. We will use it later in Ch. 6 to explain the unusual dynamics seen in Gd. The spin system in this model is represented by the Hamiltonian we derived in Eq. 2.30 yielding two separate heat baths consisting of the 5d and the 4f electons respectively. The rate equations therefore contain the energy flow into the spin system which is given by the inter-atomic and intra-atomic exchange.

$$C_e(T_e)\, \partial_t T_e = G_{ep}(T_p - T_e) + P(z,t) + \partial_z(\kappa \partial_z T_e) - \partial_t(E_d + 0.5\, E_{int}) \tag{2.38}$$

$$C_p(T_p)\, \partial_t T_p = G_{ep}(T_e - T_p) - 0.5\, \partial_t E_{int} \tag{2.39}$$

The last terms in Eq. 2.38 and 2.39 describe the coupling of electrons and phonons to the spin system. E_d includes the inter-atomic exchange as well as the anisotropy and couples in this model solely to the electron temperature. This is justified because the 5d electrons are near the Fermi level and thus directly excited by the laser pulse. The energy E_{int} given by the intra-atomic interaction is shared by the 4f and 5d electrons and thus couples to the phonon and the electron temperature.

The excitation by the laser pulse is modeled by $P(z,t)$ assuming an exponential decay into the bulk. To account for ballistic transport one should use an enhanced optical absorption depth [68, 73]. Further on it is reasonable to include the substrate in the calculation of the absorption since our films are only 10 nm thick and only 38 % of the IR pump pulse is absorbed in the Gd film. Although the optical properties of tungsten and Gd are comparable their heat capacity and thus their equilibrium temperature after excitation differs [71, 74]. It is interesting that, neglecting the heat capacity of the magnetic system, both materials have similar heat capacities. This implies that for a slow magnetic response, i.e. a weak coupling of the 4f spins to the phonon system, the influence of the tungsten substrate should, at first, be negligible.

2.2.2 Landau-Lifshitz-Gilbert (LLG) equation

To consider Langevin dynamics of spins one often uses the stochastic LLG equation. It describes the precessional motion of magnetic moments in a solid. These moments

couple via a phenomenological damping parameter to an effective magnetic field. This damping is of interest, if the temperature of the spin system is not in equilibrium with the electron and lattice temperature. In this case the LLG equation can be used to describe magnetization dynamics. The coupling of the spins to electron or phonon heat bath determines then the effective magnetic field and thus the dynamics.

In the following we will derive the LLG equation by starting with the Ehrenfest theorem. It gives the time derivative of the expectation value for an observable $\hat{A}$:

$$i\hbar \frac{\mathrm{d}\langle \hat{A} \rangle}{\mathrm{d}t} = \left\langle \left[\hat{A}, \hat{\mathcal{H}}\right] \right\rangle + \left\langle \partial_t \hat{A} \right\rangle \tag{2.40}$$

This can be rewritten for the spin operator $\hat{\boldsymbol{s}}$

$$i\hbar \frac{\mathrm{d}\langle \hat{\boldsymbol{s}} \rangle}{\mathrm{d}t} = \left\langle \left[\hat{\boldsymbol{s}}, \hat{\mathcal{H}}\right] \right\rangle \tag{2.41}$$

For a simple spin system the Hamiltonian can be expressed by $\hat{\mathcal{H}} = -g\mu_b/\mu_s\, \hat{\boldsymbol{s}}\boldsymbol{H} = \sum_i \gamma/\mu_s\, \hat{s}_i H_i$ where γ is the gyro-magnetic ratio, μ_s the spin magnetic moment and $\boldsymbol{H}$ the effective magnetic field. We can now use the permutation $[\hat{s}_i, \hat{s}_j] = i\hbar\, \epsilon_{ijk} \hat{s}_k$ and the fact that $[\hat{s}, H] = 0$ to obtain

$$\sum_i [\hat{\boldsymbol{s}}, \hat{s}_i]\, H_i = i\hbar \begin{pmatrix} \hat{s}_z H_y - \hat{s}_y H_z \\ \hat{s}_x H_z - \hat{s}_z H_x \\ \hat{s}_y H_x - \hat{s}_x H_y \end{pmatrix} = -i\hbar\, \hat{\boldsymbol{s}} \times \boldsymbol{H} \tag{2.42}$$

According to the correspondence principle we use $\langle \hat{\boldsymbol{s}} \rangle = \boldsymbol{S}$ since the expectation value of observables can be expressed by classical quantities in the macroscopic limit. This leads to an equation of motion which describes precession of spins.

$$\dot{\boldsymbol{S}} = -\frac{\gamma}{\mu_s}\, \boldsymbol{S} \times \boldsymbol{H} \tag{2.43}$$

If we consider damping of the spin wave movement we need to introduce an additional term containing a damping constant α. This term points towards the magnetic field leading to a realignment. The strength of the damping α is in principal determined by the number of available magnon decay channels. Phenomenologically this is expressed by

$$\dot{\boldsymbol{S}} = -\frac{\gamma}{\mu_s}\, \boldsymbol{S} \times \boldsymbol{H} + \alpha \boldsymbol{S} \times \dot{\boldsymbol{S}} \tag{2.44}$$

Multiplying both sides of Eq. 2.44 with $\boldsymbol{S}\times$ and using the fact that $\boldsymbol{S} \perp \dot{\boldsymbol{S}}$ and $\boldsymbol{S}^2 = 1$ we get

$$\boldsymbol{S} \times \dot{\boldsymbol{S}} = -\frac{\gamma}{\mu_s}\, \boldsymbol{S} \times (\boldsymbol{S} \times \boldsymbol{H}) - \alpha \dot{\boldsymbol{S}} \tag{2.45}$$

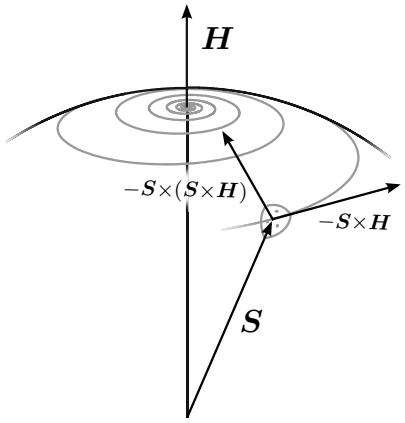

Figure 2.4: Precession and damping of spin movement as described by the Landau-Lifshitz-Gilbert equation.

Substituting this into the last term of Eq. 2.44 will result in the famous Landau-Lifshitz-Gilbert (LLG) equation:

$$\dot{\boldsymbol{S}} = \underbrace{-\frac{\gamma}{(1+\alpha^2)\,\mu_s}\boldsymbol{S}\times\boldsymbol{H}(t)}_{\text{precession}}\underbrace{-\frac{\alpha\gamma}{(1+\alpha^2)\,\mu_s}\boldsymbol{S}\times(\boldsymbol{S}\times\boldsymbol{H}(t))}_{\text{relaxation}} \tag{2.46}$$

This equation describes the precession and the relaxation of spin wave excitations. Note that in our case the magnetic field is time-dependent. It can be calculated by the formula

$$\boldsymbol{H}(t) = -\frac{\partial\mathcal{H}}{\partial\boldsymbol{S}} + \zeta(t) \tag{2.47}$$

if the Hamiltonian of the system is known. Thermal fluctuations in the spin system, like the ones calculated by the E3TM, can be taken into account through the inclusion of a white noise term $\zeta(t)$ which obeys the following equations [75]:

$$\langle\zeta(t)\rangle = 0, \qquad \text{and} \qquad \langle\zeta_i(t)\zeta_j(t')\rangle = 2\alpha\mu_S\frac{k_BT}{\gamma}\delta_{ij}\delta(t-t') \tag{2.48}$$

With this approach, i.e. with the *ab initio* calculation of the spin system Hamiltonian in combination with a phenomenological damping, it is possible to describe magnetization dynamics on a semi-microscopical level.

Chapter 3

Experimental methods

3.1 High-order harmonic generation (HHG)

If laser fields with an intensity higher than $10^{14}\,\mathrm{W/cm^2}$ are applied to a gas it is possible that radiation is emitted with a frequency that is a multiple of the fundamental. These generated high harmonics have comparable properties as the driving laser. The spatial and temporal coherence are of the same scale, but the pulse length is much shorter [76]. The direction of propagation is that of the driving laser and the divergence can even surpass the original one [77]. For reasons of symmetry only odd multiples of the laser frequency can be generated in an atomic gas (inversion symmetry of the scattering atom). This follows directly from the Fourier transformed autocorrelation function of the atomic induced dipole moment [78]. The high harmonic spectrum has an universal shape with a long plateau where harmonics can be generated with comparable intensities. The observed intensity difference of the harmonics within the plateau is the result of macroscopic phase matching. The plateau ends with a sharp cut-off at a system-dependent energy (see Fig. 3.1).

3.1.1 Semiclassical approach

The semiclassical approach leads to the *three-step model*, which divides the problem in three independently treatable steps [79] (see Fig. 3.2). The first step describes the ionization of the atom: the incoming laser field distorts the Coulomb potential of the core and the electron is able to tunnel into the continuum.

In the second step the electron will be accelerated by the driving laser field and the effect of the ion potential can be neglected due to the high field of the driving laser. In this step the path of the electron is calculated classically. When the field changes its sign the electron trajectory can cross the position of the ion again and be absorbed by emitting a photon of the energy

$$E_n = E_{kin} + I_0 \tag{3.1}$$

where I_0 is the ionization energy and E_{kin} the current kinetic energy with respect

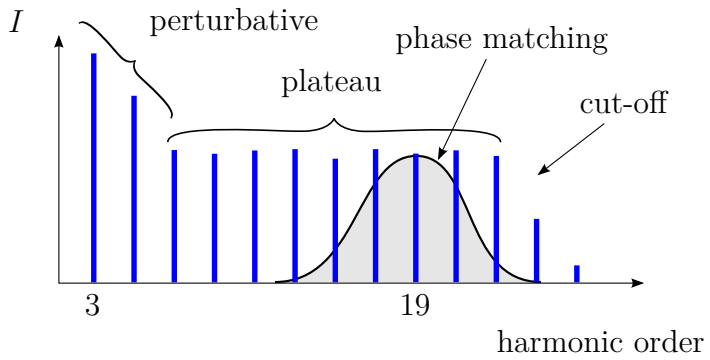

Figure 3.1: *Schematic illustration of a typical high harmonic spectrum. The spectrum starts with the perturbative region in which the intensity of the created harmonics decrease at higher order till the begin of a plateau where the intensity of the harmonics are the same. The plateau ends with a sharp intensity drop at the cut-off energy. The generated harmonics depend on the phase matching which is illustrated here for optimized intensity at the 19th harmonic.*

to the atom. This simple model leads to useful results. It explains the characteristic shape of the harmonic spectra produced by a IR laser (i.e. Ti:sapphire laser at 800 nm) and the empirical cut-off law, which will be shown below.

Step 1: Ionization

The ionization process in an applied external field is described by the adiabatic tunneling parameter γ. It was introduced by Keldysh in 1965 [80].

$$\gamma = \omega \frac{\sqrt{2 m_e I_0}}{e E_0} = \omega \left(\frac{I_0}{e E_0} \right) 2 \left(\sqrt{\frac{m_e}{2 I_0}} \right) \tag{3.2}$$

With the electron mass m_e, its charge[1] e, the external field E_0 and the laser frequency ω. I_0 is still the ionization energy. The significance of the parameter γ is in the classical interpretation of its terms [81]. The first term in Eq. 3.2 can be interpreted as a tunneling barrier with a width of $l = I_0/eE_0$. The second term leads to an electron velocity of $v = \sqrt{2I_0/m_e}$, since I_0 corresponds to the classical kinetic energy of the electron. With the introduction of a tunneling frequency $\omega_t = v/(2l)$ Eq. 3.2 reads:

$$\gamma = 2\omega \frac{l}{v} = \frac{\omega}{\omega_t} \tag{3.3}$$

For $\gamma \ll 1$ the tunneling frequency is much higher than the laser frequency and the electron has enough time to tunnel trough the potential barrier during one laser cycle. Therefore $\gamma \ll 1$ is called the tunneling regime. For $\gamma \gg 1$ the duration of one laser cycle is too short for a reasonable tunneling probability and multiphoton ionization effects dominate. These electrons are lost for a coherent HHG process, because they already start with a kinetic energy of $E_{kin} = n\hbar\omega - I_0$ in the continuum and therefore have uncorrelated initial conditions.

[1] Here e is the electron charge, note that some textbooks use e as elementary charge, which can lead to confusions concerning the sign in formulas.

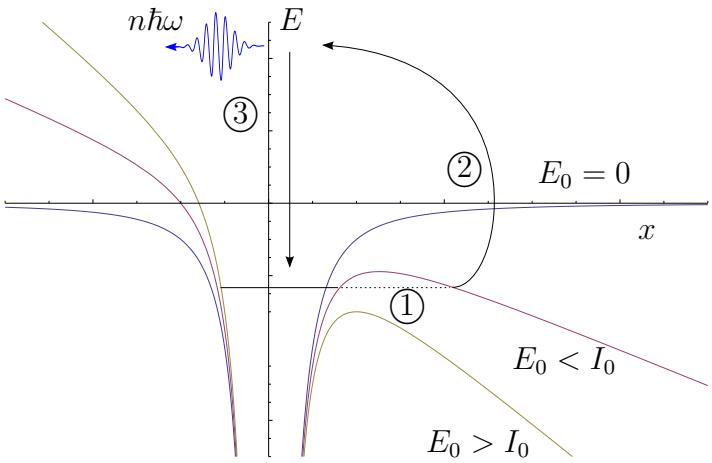

Figure 3.2: *Coulomb potential of the ion with the ionization energy I_0 for different laser intensities at the time of the maximum electric field E_0. The blue line corresponds to the unperturbed core potential. The green line illustrates barrier suppression ionization and the red one shows a tunnel ionization process, a condition in which most high harmonics are generated. Step ①: Ionization of the atom via tunneling. Step ②: Acceleration of the electron in the field of the driving laser. Step ③: Recombination of the electron and emission of bremsstrahlung-like (high harmonic) radiation.*

Step 2: Acceleration

Classically the free electron in the laser field can be described as a charged point particle in an electromagnetic field. With this simple treatment we can predict many measurable features of the HHG process. It is identical to the zero order quantum-mechanical treatment which describes the center of mass of the electron wave. The laser field is simplified to $\boldsymbol{E} = \boldsymbol{E}_0 \cos(\omega t)$. This is a good approximation, because the generation interval of a high harmonic photon is short compared to the pulse length of the driving laser which can therefore be described as a true monochromatic wave (see Fig. 3.3). As a further approximation the electron spin and the magnetic component of the laser field is neglected. With $\boldsymbol{F} = m\boldsymbol{a} = e\boldsymbol{E}$ the equations of motion become:

$$\ddot{x} = \frac{eE_0}{m_e} \cos(\omega t) \tag{3.4}$$

$$\dot{x} = \frac{eE_0}{m_e \omega} \left[\sin(\omega t) - \sin(\omega t_0)\right] \tag{3.5}$$

$$x = \frac{eE_0}{m_e \omega^2} \left[\cos(\omega t_0) - \cos(\omega t) + (t_0 - t)\omega \sin(\omega t_0)\right] \tag{3.6}$$

Step 3: Recombination

To reproduce the cut-off law we have to calculate the maximum kinetic energy the electron can gain from the laser field to generate high harmonics. It is crucial for

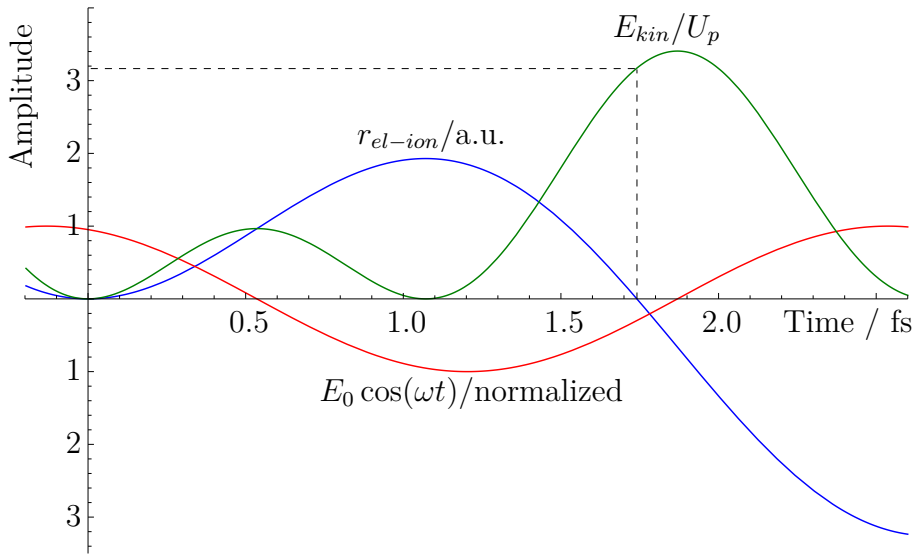

Figure 3.3: *Development of the classical electron movement for the highest possible harmonic of an 800 nm driving laser. The red curve corresponds to the field of the laser at the position of the electron. The blue curve shows the distance between the electron and the ion with the green curve following its kinetic energy. To get the highest harmonic the laser field has to have a phase shift of 0.1 π at the "birth" of the electron (cf. Ref. [82]).*

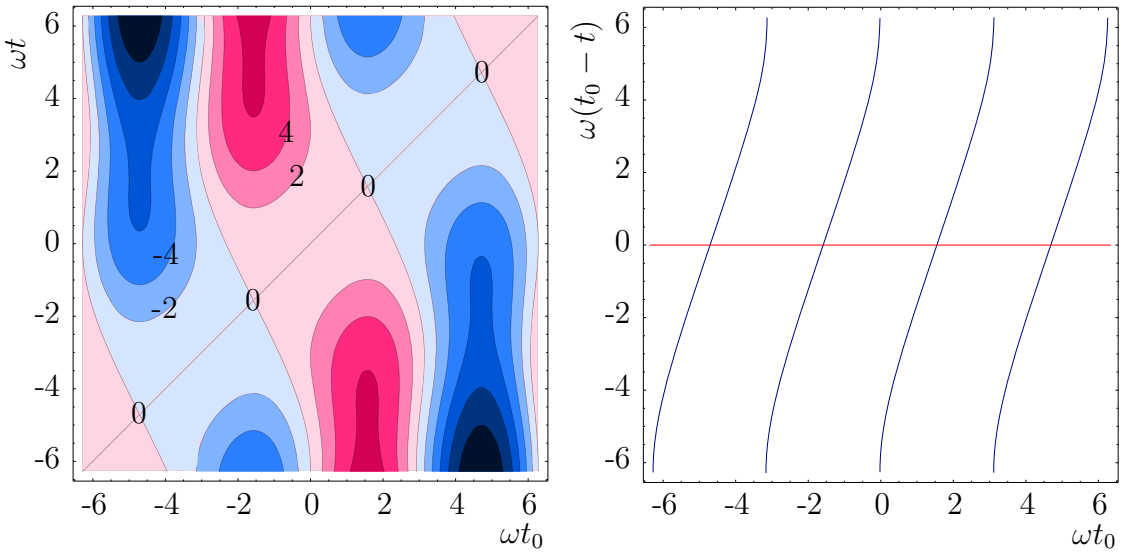

Figure 3.4: *Equation 3.6 plotted as a contour map. Of interest are the zero-lines; there the conditions for recombination are satisfied. On the right only those points (with $x(t_0) = x(t)$) are plotted and the y-axis is transformed to neglect trivial solutions like $t_0 = t$ (red line).*

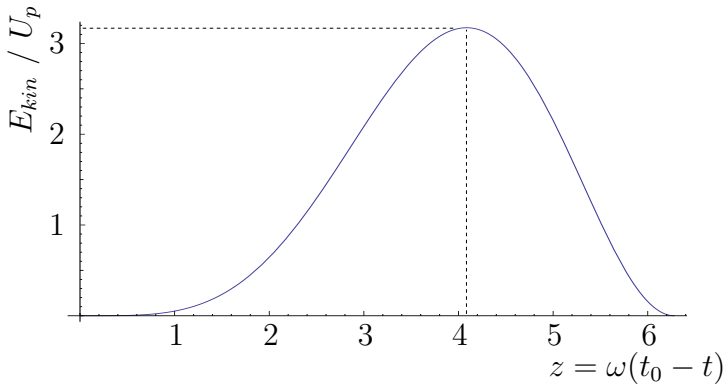

Figure 3.5: *The kinetic energy of the electron in terms of recombination for different time pairs $z = \omega(t_0 - t)$. The maximum of about $3.17 U_p$ is at $z \approx 4.086$, corresponding to a recombination time of $\Delta t = 1.74\,fs$ for a 800 nm driving laser.*

the HHG process that the electron recombines with its parent ion because only then it can contribute to a high order laser-like pulse. If the electron recombines with another ion the emitted photon will have an independent phase and direction and is therefore lost to the coherent process. For recombination the electron has to be close to the parent ion. To find the time pairs (t_0 ionization, t recombination) which satisfy this restrictive condition ($x(t_0) = x(t) = 0$) we use Eq. 3.6, as shown in Fig. 3.4.

With the transformation $\omega t = \omega t_0 - z$ in Eq. 3.6 we obtain a solution for ωt_0:

$$\omega t_0 = \arccos\left(-\frac{|z - \sin(z)|}{\sqrt{2 + z^2 - 2\cos(z) - 2z\sin(z)}}\right) \tag{3.7}$$

With this restriction the kinetic energy can be calculated from Eq. 3.5. Its maximum should give us the empiric cut-off law $E_{max} \approx 3\,U_p + I_0$ [79]. U_p refers to the pondermotive potential, and is defined as:

$$U_p = \frac{e^2 E_0^2}{4 m_e \omega^2} \quad \text{or} \quad U_p = \frac{e^2 A_0^2}{4 m_e c^2} \tag{3.8}$$

It may seem surprising at first that the pondermotive potential is not zero, after all we assume a homogeneously alternating laser field. The reason for this is the short time between ionization and recombination. This lifetime of the free electron is, in general, shorter than one full laser cycle $1/\omega$. If the electron survives exactly one or a multiple of the full cycle the pondermotive potential vanishes. The kinetic energy of the returning electron can be rewritten:

$$\begin{aligned} E_{kin} &= \frac{1}{2} m v^2 = 2U_p \left[\sin(\omega t) - \sin(\omega t_0)\right]^2 \\ &= 2U_p \left[\sin(\omega t_0 - z) - \sin(\omega t_0)\right]^2 \end{aligned} \tag{3.9}$$

Insertion of Eq. 3.7 gives us only solutions which satisfy the condition of recombination, as shown in Fig. 3.5. With this simple model we can verify the cut-off law. The highest possible harmonic can withdraw $3.17\,U_p$ from the laser field plus the ionization energy of the atom, giving:

$$E_{max} = 3.17\,U_p + I_0 \tag{3.10}$$

3.2 Angle-resolved photoelectron spectroscopy

The story of photoelectron spectroscopy started at the end of the 19th century, when Heinrich Hertz and Wilhelm Hallwachs discovered that a metal if exposed to ultraviolet light looses charge [83, 84]. Following experiments showed that this was done by emission of electrons and the kinetic energy of these photoelectrons depend solely on the wavelength of the light and not on its intensity [85]. This so called photoelectric effect was soon explained by Albert Einstein who continued the work of Max Planck on black body radiation, postulating that light always consists of quantized and localized entities who are indivisible and can thus only be absorbed as a whole [86][2]. These quanta of light, called photons have a discrete energy of $E_{ph} = \hbar\omega$ with $\hbar$ being the reduced Planck constant and ω the angular frequency of the light. If an bound electron absorbs such a photon it can escape the attractive potential of the atom leaving the solid with an distinct kinetic energy which is related to its binding strength, making it possible to measure the energy levels of electrons in atoms molecules and solids. Einstein showed that the maximum kinetic energy of the photoelectrons are given by

$$E_{kin,max} = \hbar\omega - \Phi \tag{3.11}$$

with Φ the surface potential or work function, a characteristic constant for the illuminated surface of a material.

Since then, photoemission spectroscopy has proven to be a powerful tool for the investigation of electronic properties of solids. It has greatly developed from normal emission binding energy measurements in the 1960s to high resolution full k-space measurements with third generation synchrotron sources (see Ref. [87] and references therein). A big step in this development was the commercial availability of angle resolving hemispherical analyzers. With full knowledge of the energetic band structure it was possible to examine quasiparticle interactions through their kink-like signatures in the band dispersion near the Fermi level [88]. At the same time spin detectors were combined with energy and angular resolution to obtain knowledge of exchange-split band structures and Fermi surfaces. With this full set of measured quantities, one important piece of information left is the dynamical behavior of the solid upon perturbation, which is especially interesting for correlated materials such as ferromagnets, superconductors, charge-density-wave systems, topological insulators, or heavy fermion systems. To cover quasiparticle interactions in the time domain it is desirable to operate on the sub-picosecond timescale. In recent years this challenge has been tackled by several complementary methods including measurements with free electron laser sources, femtosecond beam slicing with conventional synchrotron sources, and the *table top* approach using a femtosecond laser-based monochromatized high-order harmonic light source, as presented in this thesis.

Let us briefly recall the theoretical basics of photoelectron spectroscopy. If a solid absorbs a photon with an energy $\hbar\omega$ that is higher than its surface potential Φ, it

[2] Einstein was awarded with the Nobel prize in 1921 for this work.

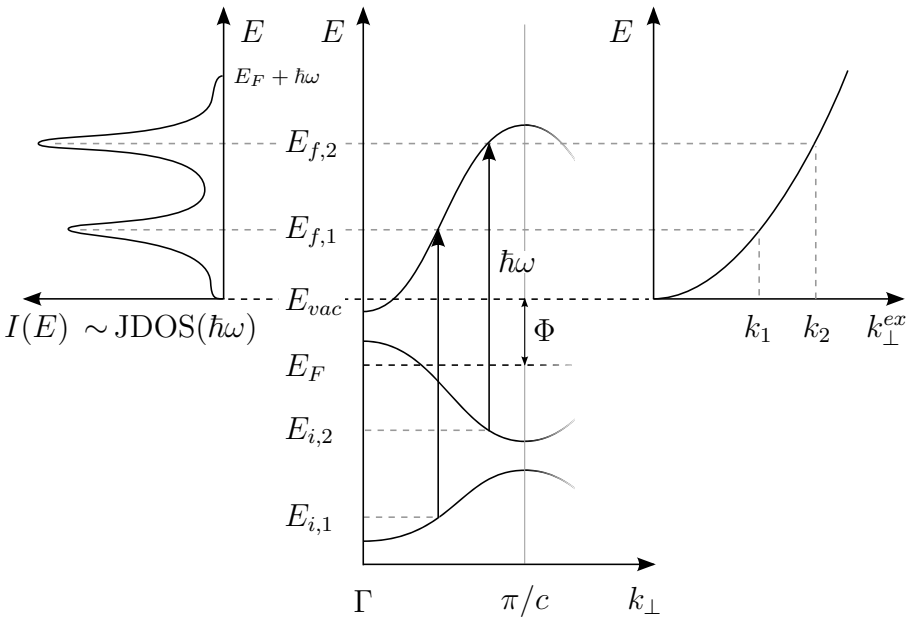

Figure 3.6: Schematic illustration of the photoemission process in the case of normal emission. *The reduced zone scheme in the middle shows the possible transitions $\langle f| \mathcal{H}_{\hbar\omega} |i\rangle$ in the crystal for a given photon $\hbar\omega$ as described by Fermis golden rule. The negligible photon momentum leads to vertical transitions $k_i = k_f$. To overcome the crystal potential the final state $|f\rangle$ has to be above the vacuum level E_{vac}. As shown on the left, the kinetic energy of the photoelectrons is defined by the joint density of states (JDOS) between $|i\rangle$ and $|f\rangle$, which prevents a direct determination of $|i\rangle$ by the measurement. After leaving the crystal surface the electrons can be treated as free particles and obey $E = \frac{\hbar^2 k^2}{2m}$ as shown on the right.*

is possible that an electron will leave the solid with a kinetic energy of:

$$E_{kin} = \hbar\omega - E_b - \Phi \tag{3.12}$$

Where E_b is the binding energy of the electron[3] and the work function is defined as the difference between the vacuum energy[4] E_{vac} and the Fermi energy[5] E_F. The emission angle and kinetic energy of the photoelectron can now be measured.

It is practical to divide the photoemission process into several steps. First the absorption of the photon with the initial- final state transition of the electron. Second the transmission of the electron to the surface and the refraction into the vacuum. And third the detection of the electron.

First step: absorption Let us consider a crystal in which the photon is absorbed. An electron is then excited from its initial state $|i\rangle$ to an unoccupied final state $|f\rangle$.

[3] E_b is usually described in the one electron approximation. This approximation is suitable for weakly bound electrons, it neglects chemical shifts, relaxation transitions and the energy difference due to the remaining photo-hole.

[4] The vacuum energy marks the barrier between bound and unbound states.

[5] The Fermi energy is the energy of the highest occupied state in a metal at 0 K.

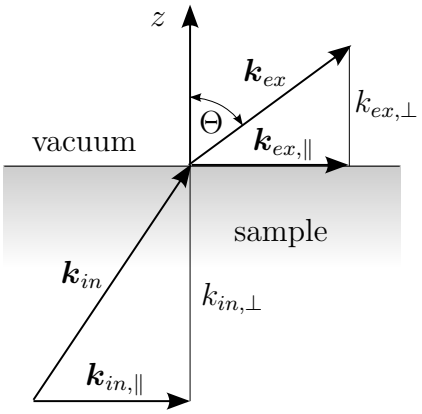

Figure 3.7: *Refraction of a photoelectron through the surface. The wave vectors of the electron are displayed.* $\boldsymbol{k}_{in}$ *corresponds to the excited electron in the sample and* $\boldsymbol{k}_{ex}$ *to the free electron after it left the surface.* $\boldsymbol{k}_{\parallel}$ *is to a good approximation conserved but* $k_{\perp}$ *is reduced by the surface potential* Φ*.*

Both initial and final state have to fulfill Blochs theorem i.e. their eigenstates have a basis of wave functions of the form $\Psi(\boldsymbol{r}) = e^{i\boldsymbol{k}\boldsymbol{r}}u(\boldsymbol{r})$ i.e. a plane wave multiplied by a lattice periodic function $u(\boldsymbol{r})$. During this process energy and momentum are conserved (no other scattering partner are involved and the electron absorbs the whole photon energy). Thereby the momentum of the photon can be neglected since its contribution is very small[6] and we have free choice of the direction of incidence for the photons. This leads to a vertical transition in the reduced zone scheme (see Fig. 3.6) which implies that the electron wave vector stays the same with the possible exchange of a multiple of the reciprocal lattice vector $\boldsymbol{G}$. It is therefore $\boldsymbol{k}_f = \boldsymbol{k}_i + a\boldsymbol{G}$ with $a \in \mathbb{Z}$. For $a = 0$ the excitation is within the first Brillouin zone. The transition $|i\rangle \rightarrow |f\rangle$ is formally described by Fermis golden rule[7]:

$$\mathcal{W}_{if} = \frac{1}{h} \left|\langle f| \mathcal{H}_{\hbar\omega} |i\rangle\right|^2 \delta\left(E_f - E_i - \hbar\omega\right) \tag{3.13}$$

with the transition probability $\mathcal{W}_{if}$ and the perturbation Hamiltonian $\mathcal{H}_{\hbar\omega}$. Fermi's golden rule provides the conservation of energy by the δ distribution for $t \rightarrow \infty$. The density of the electrons in the final state $|f\rangle$ is given by:

$$I_f(E_f, \hbar\omega) \sim \sum_{f,i,\boldsymbol{G}} \left|\mathcal{M}_{fi}\right|^2 \cdot \bar{n}(E_i) \cdot \delta\left(E_f - E_i - \hbar\omega\right) \delta\left(\boldsymbol{k}_f - \boldsymbol{k}_i - a\boldsymbol{G}\right) \tag{3.14}$$

with the transition matrix $\mathcal{M}_{fi} = \langle f| \mathcal{H} |i\rangle$ and the occupation of the initial state given by the Fermi Dirac distribution $\bar{n}(E_i)$. Electrons in a final state with $k_{\perp} > 0$ will propagate towards the surface which brings us to step two.

Second step: transmission The excited electron now propagates through the crystal and can undergo scattering events. The mean free path thereby is strongly correlated with the kinetic energy of the final state leading to an *universal curve*

[6] A 36 eV photon has a wave vector of only $0.018\,\text{Å}^{-1}$.

[7] Fermis golden rule was derived by Paul Dirac and Gregor Wentzel in 1927 [89, 90]. Fermi included it in his 1950 textbook about nuclear physics as *Golden Rule No. 2* making it famous [91].

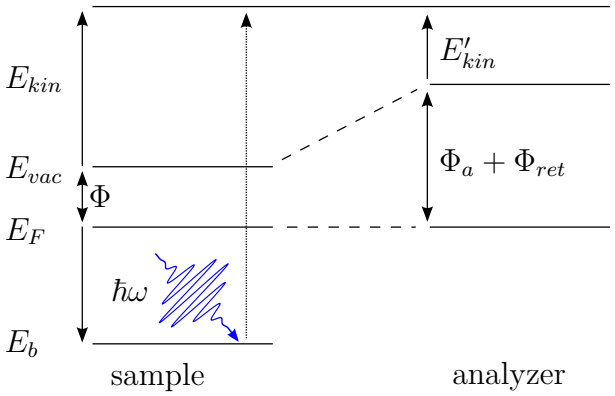

Figure 3.8: *A schematic of the photoemission process. An electron with the binding energy E_b absorbs a photon and leaves the solid with the kinetic energy $E_{kin} = \hbar\omega - E_b - \Phi$. Due to the different potentials at the sample and analyzer, the electron has to overcome an electric field to be detected with the kinetic energy of $E'_{kin} = \hbar\omega - E_b - (\Phi_a + \Phi_{ret})$.*

which applies for all metals [92, 93]. The processes which restricts the path length in photoemission from single-crystalline metals is mainly electron-plasmon scattering [94]. With the photon energies used in this work (34 - 41 eV) we only probe the first 2 - 3 monolayers allowing the study of surface and bulk states.

When an electron reaches the surface it has to overcome the crystal potential Φ which results in a refraction of the electron wave at the crystal vacuum interface. We thus have to find a relation between the final state wave vector in the crystal $\boldsymbol{k}_{in}$ and the vacuum wave vector $\boldsymbol{k}_{ex}$ outside the sample in order to reconstruct the band structure. We know that the component of the wave vector which is parallel to the surface is only altered by the reciprocal lattice vector which describes diffraction at the surface $\boldsymbol{k}_{in,\parallel} = \boldsymbol{k}_{ex,\parallel} + a\boldsymbol{G}_{\parallel}$. At zeroth diffraction order we have $a = 0$ and $\boldsymbol{k}_{in,\parallel} = \boldsymbol{k}_{ex,\parallel} = \boldsymbol{k}_{\parallel}$. In contrast the component perpendicular to the surface changes considerably, because the electron is refracted by the surface potential Φ; see Fig. 3.7. For a free electron we know the dispersion relation:

$$E_{kin} = \frac{\hbar^2 k_{ex}^2}{2m_e} = \frac{\hbar^2}{2m_e}\left(k_{\parallel}^2 + k_{ex,\perp}^2\right) \tag{3.15}$$

and can now, with the information of the emission angle, determine the components of the wave vector $\boldsymbol{k}_{ex}$:

$$\boldsymbol{k}_{\parallel} = \sin(\Theta) \cdot \sqrt{\frac{2m_e}{\hbar^2} \cdot E_{kin}} \tag{3.16}$$

Third step: detection The measured kinetic energy of the electrons depend in general on the photon energy, the binding energy, and the work functions of the sample and the analyzer as illustrated in Fig. 3.8. If we keep the wavelength of the incoming photons constant and neglect matrix element effects then the measured photoemission spectrum will be proportional to the *joint density of states* (JDOS). The left side of Fig. 3.6 illustrates this. To get the density of only occupied states one needs to vary the photon energy for a fixed measured electron energy. This

way the final state $|f\rangle$ stays the same and the photon energy scans the initial state $|i\rangle$.[8]

In our experiment we have to choose a photon energy of about 36 eV to probe the Δ_2-like bands at the Γ_2-point in the fourth Brillouin zone (cf. Fig. 1.1)

3.3 Magnetic linear dichroism

In the literature *magnetic dichroism* (MD) designate effects, where the interplay of light and matter depends on the magnetization. An important factor in MD is the measurement geometry and the polarization of the light. In the past a variety of methods have been suggested and used to measure MD [62, 95–97]. In general MD can exist if there is no space-symmetry operation which reverses the magnetization without changing the system otherwise [62]. The geometry specifies the kind of dichroism that one can expect to see, e.g. dichroism that is sensitive to unidirectional (Fig. 3.9 d - f) or uniaxial (Fig. 3.9 g) magnetic order. Despite this difference MD can be caused by two different physical effects. The first is called atomic dichroism and stems from the interference of electron waves with different symmetry which are emitted from the same atom. The second is diffraction dichroism and has its origin in the interference of the emitted electron wave that scattered on the atomic potentials of the different lattice sites. To avoid confusion we give an overview over the most common methods and geometries to measure MD:

MCD - In *magnetic circular dichroism* the photoelectron spectrum of magnetic states are measured using light with circular polarization (Fig. 3.9 e). Magnetic contrast is achieved by changing either the circularity of the light or the magnetization direction. The best geometry for MCD is coplanar with the magnetization (anti-)parallel to the propagation direction of the incident light. In MCD one measures photoelectrons from magnetic states.

XMCD - *X-ray magnetic circular dichroism* is based on the same physical principles as MCD, using higher photon energies. To obtain XMCD one does not necessarily need to detect the photoelectrons or the corresponding sample current, but can instead measure the absorption or reflectivity of the sample. By choosing this approach one avoids the influence of space charge on the signal which is especially critical in time-resolved measurements. To measure the magnetization with XMCD one needs to tune the photon energy over the absorption edges of a magnetic transition, i.e. normally the transition from an occupied unpolarized to an unoccupied spin-polarized state. The advantages of this method are that one does not need an electron energy analyzer and that the sample does not have to be single crystalline. A comprehensive article about XMCD can be found in Ref. [98].

MLD - In *magnetic linear dichroism* one usually uses p-polarized light to measure the dichroism. The MLD-signal is then obtained by changing the magnetization direction. Valid MLD geometries have to be chiral but are not allowed to be

[8] Analogue, the DOS for unoccupied states can be measured with simultaneous variation of $\hbar\omega$ and E_{kin} by the same amount.

completely orthogonal. Fig. 3.9 d shows such a geometry. In earlier publications the term MLD was only used to describe the asymmetry between s- and p-polarized light, a geometry which is identical to Fig. 3.9 g and does not depend on the angle θ. This particular geometry is sensitive to the general spin alignment and can be used to measure *uniaxial* samples, that includes also samples without net magnetization such as, e.g., antiferromagnets. The geometry in Fig. 3.9 d on the other hand requires *unidirectional* magnetic systems (ferro- or ferrimagnets). It is sensitive to the net magnetization along the specified direction and depends on the angle θ. As a consequence this geometry was called MLDAD instead, which stands for *magnetic linear dichroism in the angular dependence* [97]. Nowadays the term MLD is commonly used for both cases, and the experimental geometry is typically specified in a figure; as we will do throughout this thesis. MLD can also be measured with unpolarized light, as it is a combination of s- and p-polarized light. The photoelectrons from the s-component do not contribute to the MLD signal because such an excitation process is invariant under magnetization reversal (see Fig 3.9 g compared with d and f), and since the absorption is usually less for s-polarized light, the MLD signal is similar to measurements with solely p-polarized light.

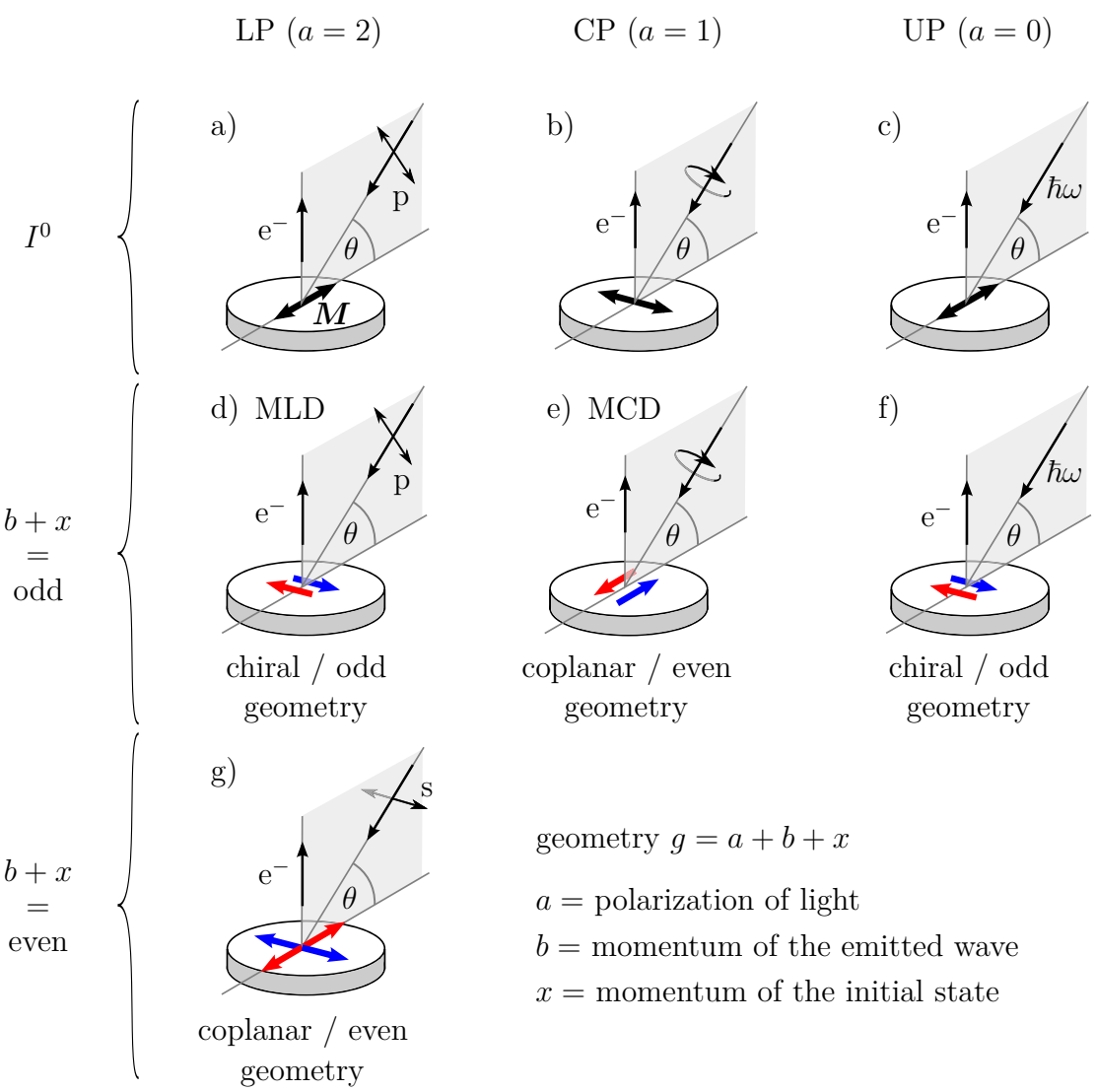

Figure 3.9: Common measurement geometries of atomic dichroism for an in-plane magnetized sample. *The first row shows geometries to measure the nonmagnetic spectrum I^0 for the respective light polarizations. Bold arrows show the magnetization direction where double arrows (⇔) indicate that the spectrum is independent on the sign of $\boldsymbol{M}$. The second row shows geomeries for $b + x$ = odd. The normalized difference of the "blue" and "red" measurement give (linear combinations) of the fundamental spectra I^x. In the case of even wave emission ($b = 0,2,4$) the geometries d)-f) allow the measurement of odd fundamental spectra which reflect the orientation of the magnetic moment and are proportional to the magnetization. In that case the geometry g) probes even fundamental spectra which reflects general spin ordering. Note that g) is measured with s-polarized light and the two geometries are invariant under magnetization reversal. In fact from a) and c) follows that the "red" geometry in g) gives the isotropic spectrum I^0. To measure the MCD of e) one can also change the circularity of the light instead of the magnetization direction. For maximum MCD the angle between the incident light and the magnetization direction should be small. For maximum MLD in the geometry d) the angle θ should be 45^o.*

3.3.1 Atomic dichroism

In this section we want to have a look at the origin of atomic dichroism using a theory developed by Thole and van der Laan in a series of publications [99–102][9]. Our goal is to investigate the special case of Gd 4f MLD in chiral measurement geometry[10]. A rigid calculation of atomic dichroism is quite tedious. We therefore are going to restrict ourselves to a brief introduction and a qualitative analysis of the outcome following the above mentioned publications together with Ref. [62] and [103]. Thole and van der Laan give a general expression for the angular-dependent photoemission intensity:

$$J^a(\boldsymbol{P},\boldsymbol{k},\boldsymbol{M}) = \frac{1}{4\pi}\sum_x I^x \sum_b U^{abx}(\boldsymbol{P},\boldsymbol{k},\boldsymbol{M}) \cdot \sum_{c\,c'} A^{cc'}_{abx} R^c R^{c'} e^{i(\delta_c - \delta_{c'})} \tag{3.17}$$

where R^c is a radial dipole matrix element of the continuum final state with momentum $c = l \pm 1$. The phase difference of the two final state channels c and c' is given in the last term; $A^{cc'}_{abx}$ is a numerical factor. The fundamental spectra I^x are thereby linear combinations of the primitive spectra [100] and give the probability of removing an electron with orbital momentum x. Within the framework of a multipole expansion x ranges from 0 to $2l$ (in Gd $x = 0,1,...,6$). x is also equal to the number of nodes in the corresponding fundamental spectra (cf. Fig. 3.10 c). Odd values of x stand for antisymmetric and even values for symmetric linear combinations. The different I^x are specified as: the isotropic spectrum I^0, the dipole or orbital spectrum I^1, the anisotropic or quadrupole I^2, octupole I^3, and so on[11]. U^{abx} comprises a combination of spherical harmonics and describes the angular interaction of the different momenta ($\boldsymbol{P}, \boldsymbol{k}$, and $\boldsymbol{M}$) represented by the indices abx which stand for a: the polarization of the light (with $a = 0, 1, 2$ for un-, circular-, and linear- polarized light, respectively), b: the momentum of the emission wave, i.e. its angular distribution with $b = 0, 1, 2, ...$ for $s, p, d, ...$ wave emission, and x: the above introduced moment from the atomic shell. In detail U^{abx} is defined as:

$$U^{abx} = \sum_{\alpha\beta\xi} n^{-1}_{abx} \begin{pmatrix} a & b & x \\ -\alpha & -\beta & -\xi \end{pmatrix} \mathcal{Y}^\alpha_a(\boldsymbol{P}) \mathcal{Y}^\beta_b(\boldsymbol{k}) \mathcal{Y}^\xi_x(\boldsymbol{M}) \tag{3.18}$$

with $\mathcal{Y}^m_l$ being normalized spherical harmonics, and n_{abx} an additional normalization factor (see [101] for details).

Let us consider the case of Gd where Russell-Saunders coupling is a good description [64]. The 4f ground state is denoted as ${}^8S_{7/2}$ with $L = \sum_i l_i = 0$ and $S = \sum_i s_i = 7/2$ we get a total momentum $J = S + L$ of 7/2. In the final state only 6 electrons are left in the 4f shell giving rise to only one possible configuration with $L' = 3$ and $S' = 3$. The distribution of the emitted electron wave has a symmetry depending on the angular momentum difference from initial to final state. Simplified, the

[9] Especially noteworthy is the 1995 article by van der Laan [102].

[10] i.e. the polarization of the incidence light $\boldsymbol{P}$ and the electron emission vector $\boldsymbol{k}$ are coplanar and perpendicular to the magnetization direction $\boldsymbol{M}$ as shown in Fig. 3.9 d and 3.10 a.

[11] Note that the index convention is adopted from [101, 102] and differs slightly from earlier publications.

emitted continuum waves c can be expressed through $c = |L - L'| \pm l_{ph}$ with l_{ph} being the momentum of the absorbed photon. We have therefore two allowed emission channels with $c = 3 \pm 1 = 2, 4$. Analogue to the atomic orbital notation they are called d-wave and g-wave emission as mentioned above. We can now specify Eq. 3.17 with $a = 2$; $b = 2, 4$; $c = 2, 4$; $c' = 2, 4$ and the convenient notation $R^c R^{c'} e^{i(\delta_c - \delta_{c'})} = R^{cc'}$:

$$\begin{aligned} 4\pi J_{MLD} = \sum_{x=\text{odd}} I^x [&A^{22}_{22x} U^{22x} R^{22} + U^{22x} A^{24}_{22x} R^{24} + U^{22x} A^{44}_{22x} R^{44} \\ &+ U^{24x} A^{22}_{24x} R^{22} + U^{24x} A^{24}_{24x} R^{24} + U^{24x} A^{44}_{24x} R^{44}] \end{aligned} \tag{3.19}$$

Atomic dichroism is caused by interference of different waves, thus we neglect terms with $c = c'$. The summation is only over odd values of x since the I^{odd} represent the antisymmetric linear combinations of the primitive spectra that define the MLD signal ($a + b + x$ needs to be odd in a chiral geometry [101]). In addition b has to be in the range of $|a - x|, ..., a + x$ to obey angular momentum conservation [102], nullifying functions like U^{241}. Using the values for $A^{cc'}_{abx}$ given in [101] we get:

$$\begin{aligned} 4\pi J_{MLD} = &I^1 \frac{45}{14} U^{221} R^2 R^4 \sin\delta \\ &+ I^3 \left(-\frac{5}{6} U^{223} - \frac{2}{3} U^{243} \right) R^2 R^4 \sin\delta \\ &+ I^5 \left(-\frac{3}{14} U^{245} - \frac{13}{42} U^{265} \right) R^2 R^4 \sin\delta \end{aligned} \tag{3.20}$$

Explicit calculation of the angular functions U^{abx} yield a simple expression [62]:

$$J_{MLD} = -\frac{1}{4\pi} \left(\frac{27}{14} I^1 + \frac{3}{4} I^3 + \frac{15}{112} I^5 \right) R^2 R^4 \sin(\delta)\, \sin(2\alpha) \tag{3.21}$$

with δ being the phase difference between c and c'. The overall signal scales with $\sin(2\alpha)$ with α being the angle between $\boldsymbol{k}$ and $\boldsymbol{P}$. From this it follows that the MLD signal vanishes for a completely orthogonal geometry and is best for $\alpha = 45°$. It further follows from Eq. 3.21 that for the case considered here, i.e. for chiral MLD ($\boldsymbol{k} \times \boldsymbol{P} \| \boldsymbol{M}$), the relative intensities of the magnetic fundamental spectra are not angular-dependent and have always an I^1 contribution of 70 % in the Gd 4f MLD spectrum. It can be shown that I^1 is directly proportional to the magnetization [62], and as a consequence of Eq. 3.17 all I^x with $x =$ odd are proportional as well (in the case of Gd this is directly obvious from Eq. 3.21). We will therefore call the spectrum obtained by a chiral MLD measurement (or a coplanar MCD) the magnetic spectrum.

Sometimes the spectrum I^1 is called MCD and I^2 MLD; this terminology should be avoided since it is only true for photoemission from the p-shell ($c = 0, 2$) in a coplanar geometry (Fig. 3.9 e and g). In this particular case MCD measures only I^1 and MLD only I^2. In general, observation of the spectra $I^{2,4,\cdots}$ requires splitting of the different orbital components $|m_l|$ which is, in absence of an electrostatic field, a measure of the general spin alignment along the direction specified by the geometry [102]. Note that spin *alignment* can persist even if there is no net magnetization as, e.g. in the case of antiferromagnetism. In contrast the odd spectra measure the *orientation* of the spins, i.e. the magnetization as mentioned above.

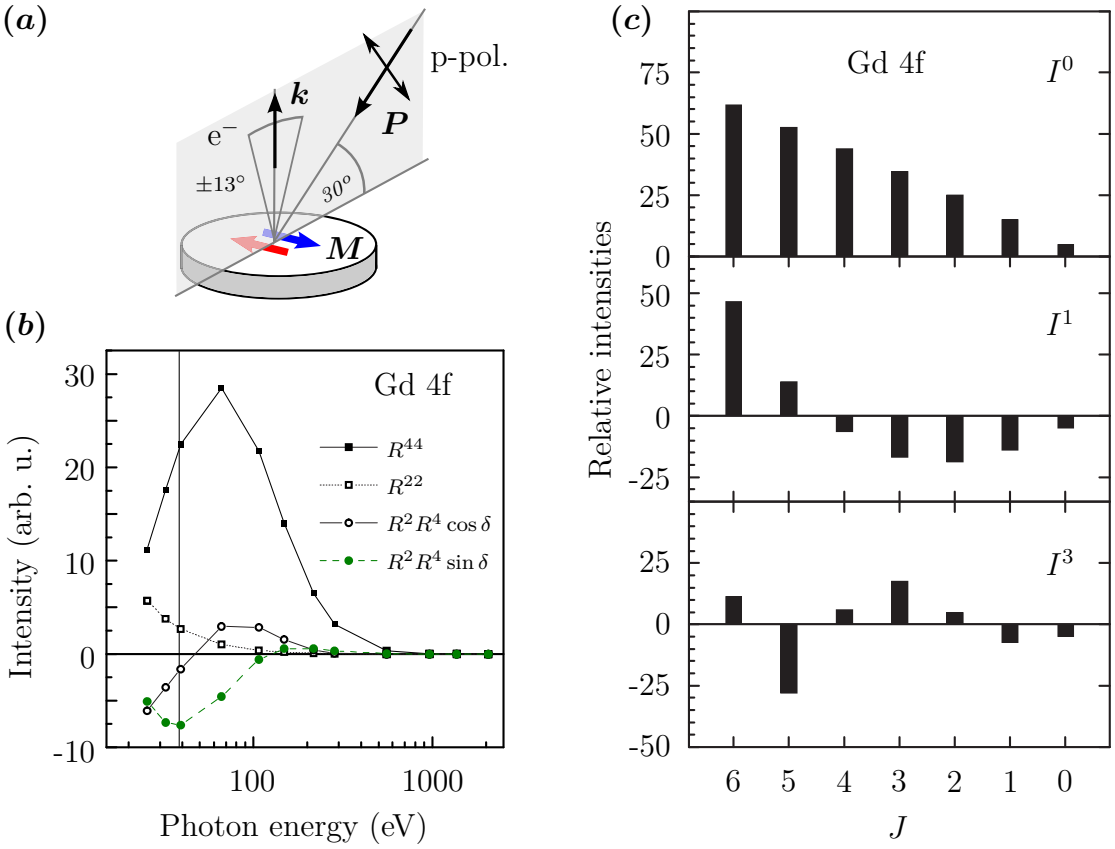

Figure 3.10: ***(a)*** *Chiral geometry used for MLD. The light polarization* $\boldsymbol{P}$ *and the electron emission vector* $\boldsymbol{k}$ *are coplanar with respect to each other and perpendicular to the magnetization* $\boldsymbol{M}$*. Note that* $\boldsymbol{k}$ *and* $\boldsymbol{P}$ *are not allowed to be perpendicular to measure MLD.* ***(b)*** *Calculated radial transition matrix elements of the Gd 4f state from Ref. [62] using a Hartree-Fock approach [104]. At our photon energies the* $f \rightarrow g$ *transition described by* R^{44} *dominates over* $f \rightarrow d$ *(*R^{22}*). The solid line at 36.8 eV marks the photon energy used in Ch. 6 where the ratio of g- vs d-wave excitation is 8:1. At that energy atomic dichroism stems mainly from the sine component of the d- and g-wave interference (green dots).* δ *denotes the phase difference between* R^2 *and* R^4*.* ***(c)*** *The most intense fundamental spectra of the Gd* ^7F_J *photoemission multiplet consisting of the isotropic spectrum* I^0 *the dipole spectrum* I^1 *and the octupole spectrum* I^3*, from Ref. [62].*

3.3.2 Diffraction dichroism

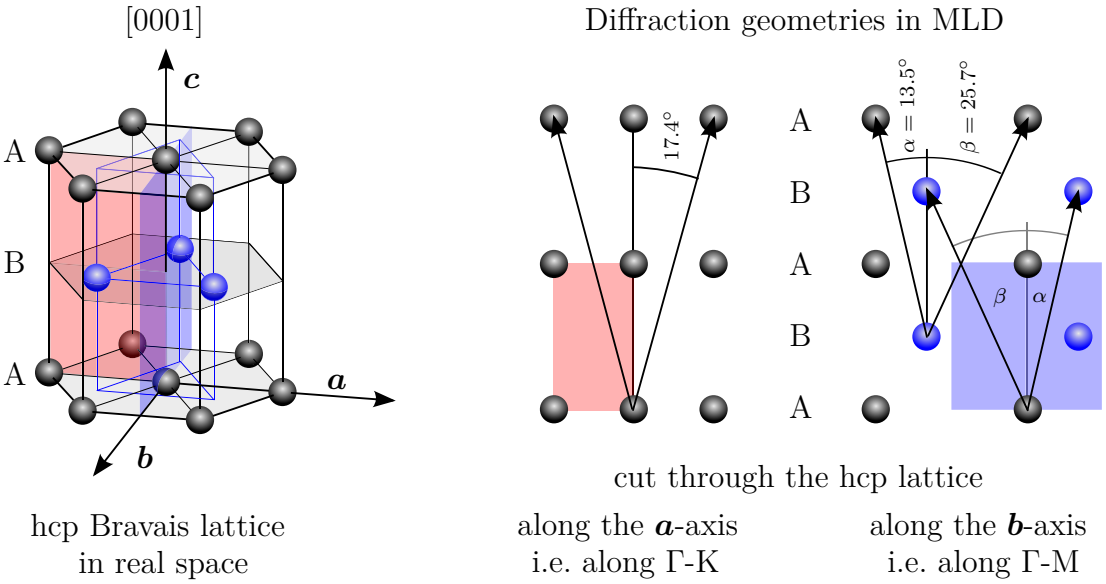

Figure 3.11: High symmetry planes for diffraction dichroism. *The hcp Bravais lattice of Gd and Tb allows for electron emission in two high symmetry planes, one along the* ***a****- and one along the* ***b****-axis. The unit cells of these planes are marked in red and blue respectively. The detected electrons in the red plane show strong diffraction dichroism with a high angular symmetry [105]. The detected electrons in the blue plane show only moderate diffraction dichroism with an angular dependence that is determined by α and β.*

Besides the above discussed atomic origin, magnetic dichroism can also occur due to scattering of photoelectrons with the lattice potential on their way to the surface [106]. The MLD signal then originates from interference of identical electron waves scattering from different lattice sites. That is why, unlike atomic dichroism, diffraction depends strongly on the emission angle and can even, in some circumstances, overcome the atomic part. In fact from the calculation in Fig. 3.10 (b) we can expect diffraction of g-wave emission (R^{44}) to determine the whole MLD signal. This calculation was confirmed by measurements of Krupin who reported dominating diffraction dichroism in Gd MLD using 60 eV photons [105]. In close agreement with the theoretical ratio $^{\text{diff.}}/_{\text{at.}}$ of $^{5}/_{1}$ at this photon energy, he measured $^{4}/_{1}$.

There are some notably differences between our setup and the one used by Krupin. Except the lower photon energy (≈ 36 eV vs 60 eV), we measure along the Γ - M crystal plane whereas Krupin measured along Γ - K (see Fig. 3.11). This results in a different symmetry, while in the Krupin setup the dominant diffraction leads to a sign reversal when scanning from positive to negative angles, we only see a moderate modulation of the dichroism signal due to diffraction.

Figure 3.12 shows the angular dependence of MLD in Gd along Γ - M. The signal keeps its sign but is weaker at higher emission angles. A quantitative analysis is given in Fig. 3.13 where the integral of the MLD signal is plotted. The graph

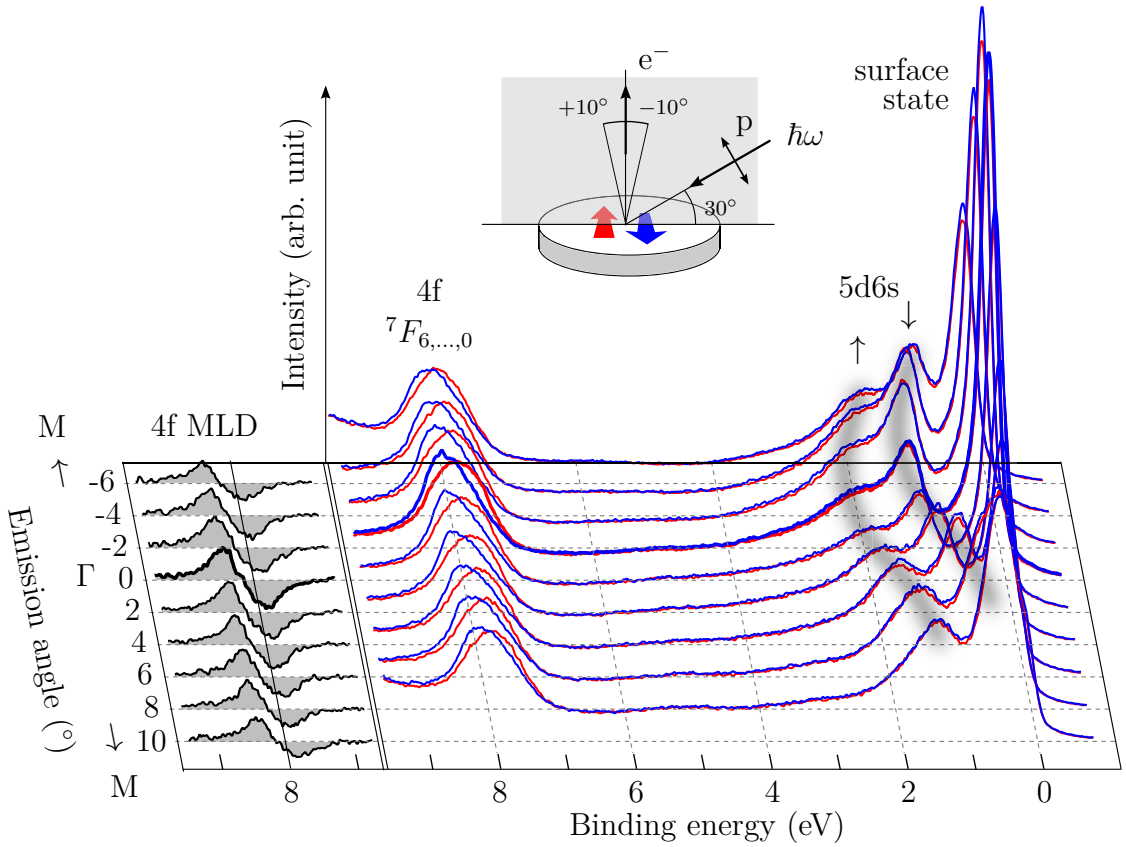

Figure 3.12: Static ARPES of a magnetized Gd film showing diffraction in the angular dependence of the 4f magnetic linear dichroism. *The photon energy was 36.2 eV. The normalized MLD signal $(I_n - I_p)/(I_n + I_p)$ is shown on the left. The dispersing 5d6s bands on the right are exchange split into majority ↑ and minority ↓ component.*

shows the angular dependence of gadolinium and terbium which is sine-like in both cases and can phenomenologically be described by the superposition of two curves depending on the dominant angles α and β as defined in Fig. 3.11

$$A_1 \sin\left(\frac{\gamma+\phi}{\alpha}\right) + A_2 \sin\left(\frac{\gamma+\phi}{\beta}\right) + I_{at.} \tag{3.22}$$

where γ is the emission angle, ϕ an arbitrary phase shift and $I_{at.}$ the atomic contribution which is angle independent. The solid lines in Fig. 3.13 are fits from this model. In Gd the fit reflects the theoretical angles ($\alpha = 13.5°, \beta = 25.7°$) with $\alpha = 13°$ and $\beta = 28°$ reasonably well. In Tb only the fitted α is with 13° as expected[12] but β is with 54° twice as big as expected. Another difference is the ratio A_2/A_1 which is two for Gd and one for Tb.

From the fitted values of A_1, A_2 and $I_{at.}$ we can estimate the contribution of diffraction dichroism. In Gd the ratio $(A_1 + A_2)/I_{at.}$ is with $^3/_5$ twice as big as in Tb with $^3/_{10}$ but in both cases atomic dichroism dominates. This is contrary

[12] The theoretical values for Tb are basically the same as for Gd: $\alpha_{Gd} = 13.5°$, $\alpha_{Tb} = 13.6°$, $\beta_{Gd} = 25.7°$ and $\beta_{Tb} = 25.8°$.

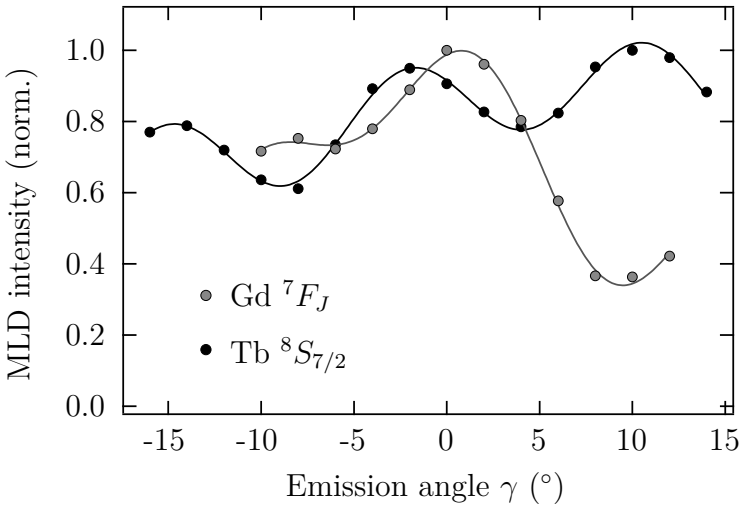

Figure 3.13: Normalized MLD vs emission angle. *The MLD signal stems from the unresolvable $^7F_{0,\ldots 6}$ multiplet of Gd and the $^8S_{7/2}$ high spin final state in Tb. Diffraction dichroism leads to an γ - dependent modulation of the MLD signal. Solid lines are the corresponding fits as explained in the text.*

to the aforementioned calculation from Starke [62], shown in Fig. 3.10 (b) which would suggest dominating diffraction at our photon energies. These calculations are confirmed by experiments from Krupin [105] who measured along the Γ - K direction. We can therefore conclude that the chosen crystal plane in our setup seems to suppress diffraction dichroism. For an in-depth investigation of this matter, simulations of multiple electron scattering (as e.g., in [107]) with the additional inclusion of multiplet calculations are needed.

Chapter 4

Setup and sample preparation

4.1 Instrumental setup

This section is an adaption of the author's work "A high-order harmonic generation apparatus for time- and angle-resolved photoelectron spectroscopy" published in Review of Scientific Instruments 84, 075106 (2013) [III]. Note that the beamline design describes work done by the co-authors of that paper, O. Schwarzkopf and P. Wernet. The section about space charge is revised and significantly extended.

With the increasing availability of reliable femtosecond lasers, HHG has developed into a versatile source of XUV radiation. In addition, high-order harmonic radiation retains many desirable properties of the laser used to generate it. For use as a spectroscopic light source, the most important of these are the spatial and temporal coherence, which lead respectively to the formation of a collimated beam of femtosecond XUV pulses.

Most high-order harmonic generation experiments are used for their femtosecond time resolution to investigate electron dynamics in atoms and molecules in the gas phase [108]. In contrast only a few experiments have been optimized for the investigation of dynamics in solids [109, 110], and only some of those look at transient band structures [111–115]. Our objective is to combine the power of ARPES with the fs time resolution and extreme-ultraviolet (XUV) photon energies available through HHG, the latter allowing access to high electron momenta to probe the whole Brillouin zone. Photoelectrons generated at these photon energies have mean free paths in the material of only a few Ångstrom, so this technique is inherently surface sensitive and probes the first few sub-surface layers to yield information on the bulk band-structure. Since the native bandwidth of even a single harmonic generated by a 40 fs near-infrared laser pulse is on the order of 0.25 - 0.5 eV [116], it is desirable to select a fraction of the bandwidth. To this end we have designed and built a monochromator beamline delivering a bandwidth as small as 90 meV at 35.6 eV, while maintaining an overall time resolution better than 150 fs and sufficient photon flux for reasonable measurement times.

Apparatuses for time-resolved photoemission studies at surfaces have been presented by several authors with distinct objectives. The main differences between

the setups are the repetition rate of the laser and the photon-energy selection, which is the primary focus of this section. Currently there are several different approaches for wavelength selection, most common are single grating [116–118] and double grating [112, 119, 120] monochromators. Generally single grating arrangements have a higher transmission while double grating arrangements deliver shorter pulses by compensating the tilt of the wave front incurred by diffraction from a single grating. Both approaches can be modified to make use of conical diffraction to achieve higher transmission [121, 122]. An alternative approach is to employ multilayer mirrors whose coating is tailored to reflect a fixed single harmonic from the frequency comb delivered in HHG [114, 123, 124], or to select a broad bandwith close to the high-energy cutoff for attosecond spectroscopy [111].

4.1.1 Beamline design

Our approach seeks a compromise between energy and time resolution, while maintaining flexibility (i.e. wavelength tuneability), a high optical throughput and reduced optical complexity. We therefore opted for a design based on a single-grating monochromator, with the grating mounted conventionally. Since the overall energy resolution of a monochromator is partially determined by the convolution of the input and output slits, it is desirable to have a mirror between the XUV source and the entrance slit of the monochromator to focus the XUV on the entrance slit. Otherwise the HHG source is effectively the entrance slit, and increasing the resolution by reducing its size (by making the IR focus smaller) may have undesirable consequences for HHG efficiency. Therefore, we included a mirror before and after the monochromator. To obtain a high reflectivity, the mirrors and grating are designed for grazing incidence and are therefore toroidal. Our design also makes use of extensive differential pumping along the length of the beamline. From 10^{-3} mbar at the HHG source, a pressure of better than $3 \cdot 10^{-11}$ mbar can be maintained indefinitely in the photoemission chamber, allowing for long measurement times without sample degradation.

To reach the desired performance, the optical design was optimized by modeling and ray tracing. The results are shown in Fig. 4.1. An overview of the apparatus is depicted in Fig. 4.2. The overall efficiency of the beamline was obtained with the REFLEC code [125], taking into account the incidence angles and the micro-roughness of the optical surfaces, as well as the specified shape of the grating profile (Fig. 4.1). Geometrical effects (e.g., losses at the slits) and the transmission of the IR filtering aluminium foil are not included. An efficiency of 10 % or better could be achieved over the whole energy range. Starting with a 1.5 mJ IR pulse ($\hbar\omega = 1.6$ eV) at a pulse repetition rate of 10 kHz we obtain 10^{10} to 10^{11} photons/s in a single harmonic. The spot size at the sample position has a FWHM diameter of about 130 µm.

Simulations using the RAY code [126] yielded the spectral and temporal widths of the transmitted harmonic pulses as shown in Fig. 4.1 (b) and (c). They where obtained by end-to-end simulations of trajectories originating from a model of the HHG source. The spectral width in Fig. 4.1 (b) includes both the monochromator

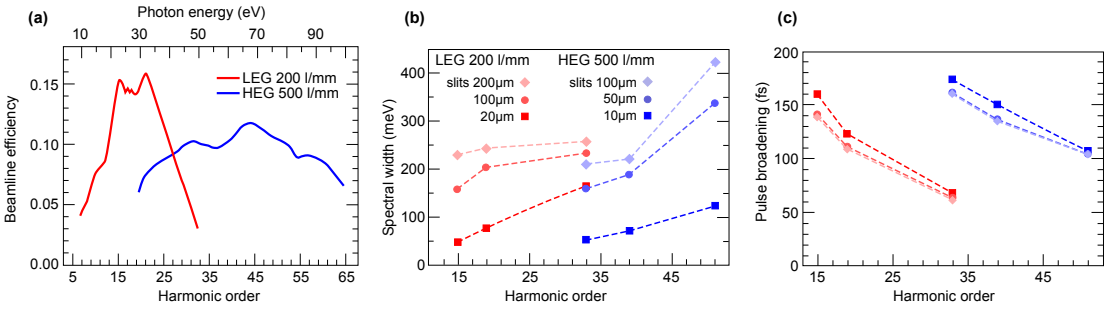

Figure 4.1: *Calculated performance of the monochromator beamline. (a) Beamline optical transmission (efficiency), which is dominated by the grating reflectivity. The lower scale gives the harmonic order in terms of the fundamental IR beam (800 nm), the corresponding photon energy is indicated on the upper scale. (b) Spectral width as a function of harmonic order for a range of slit widths and the appropriate grating. The plotted values include both the monochromator band pass and the inherent width of the respective harmonic. (c) Temporal broadening due to the grating shown for the same parameters as (b).*

band pass and the inherent spectral width of the respective harmonic, which was assumed to have a Lorentzian profile with a width of 250 meV (for all harmonics up to order 39), as estimated from the width of photoelectron lines obtained with a HHG setup at Helmholtz-Zentrum Berlin [127]. For the 51st order, a width of 420 meV was assumed [128]. These considerations demanded the inclusion of two exchangeable gratings to reach the desired energy resolution across the whole expected HHG spectrum. The low energy grating (LEG) for photon energies 15 - 40 eV has 200 lines/mm. The high energy grating for 35 - 110 eV photons has 500 lines/mm. For slit openings $\geq 100\,\mu$m, the monochromator acts more or less as a harmonic filter, i.e. the complete selected harmonic is transmitted and maximum flux is achieved. Reducing the slit size yields better energy resolution, at the price of lower photon flux.

The calculated temporal pulse broadening of the harmonic by the grating is shown in Fig. 4.1 (c). As the temporal broadening is mainly determined by the number of illuminated grooves of the grating, i.e. the tilt of the wave front, it depends both on the divergence of the incoming harmonic beam and the angle of incidence on the grating. Therefore the broadening is energy (i.e. harmonic order) dependent, but for all harmonics lies in the range of 100 - 150 fs according to our ray tracing.

An analytic expression for the pulse broadening may be found in Ref. [129]. To first order pulse broadening stems from the lateral dispersion and is determined by the available bandwidth at each point of the exit slit, i.e. the energy resolution of the monochromator grating $\Delta\lambda = N \cdot \lambda$, where N is the number of illuminated lines. For illustration we calculate the temporal broadening at 35.6 eV due to the LEG. The monochromator entrance arm is 331 mm long so, assuming a divergence of the harmonics of 4 mrad full width half maximum (FWHM), the spot size at the grating is 1.3 mm. This is elongated to 4 mm by the grazing incidence angle of 19°. Thus 800 lines of the 200 lines/mm grating are illuminated, leading to a delay of $800 \cdot \lambda/c \approx 100$ fs, where the wavelength equals $\lambda = 34.4$ nm and c is the speed

Table 4.1: *Optical parameters of the monochromating XUV beamline. All optical elements are toroidal and gold coated to a depth of 40 nm for optimal reflectivity.*

Optical element	mirrors	LEG	HEG
Long radius	9567 mm	1000 mm	1000 mm
Short radius	104.5 mm	104.9 mm	104.9 mm
Deviation angle	168°	142°	142°
Slope error rms*	≤ 2” / ≤ 5”	≤ 1” / ≤ 5”	≤ 1” / ≤ 5”
Microroughness rms	≤ 0.5 nm	≤ 0.5 nm	≤ 0.5 nm
Line density	...	200/mm	500/mm

* long axis / short axis

of light. As the bandwidth $\Delta\lambda$ will always pass through the monochromator, the slit size sets the energy resolution but only little affects the pulse broadening (cf. Fig. 4.1).

The frequency shift across the beam profile (spatial chirp) of a pulse diffracted off the grating leads to group velocity dispersion. This second order pulse broadening scales with $\lambda^3 \cdot N^2$ and is moderate in our setup (≈ 8 fs at $\hbar\omega = 35.6$ eV) [129]. Group velocity dispersion likewise causes a frequency chirp of the pulse which we estimate to 30 meV over the 100 fs pulse duration at the sample position. The chirp leads to a small broadening of the ARPES spectra compared to the overall energy resolution of the experiment of about 200 meV.

4.1.2 Beamline realization

The layout of the beamline can be seen in Fig. 4.2, along with the other components forming the complete tr-ARPES experiment. Technical details of the XUV optics are presented in Table 4.1.

The HHG process occurs in the gas cell. From there the XUV radiation co-propagates with the IR beam through two 2 mm diameter fixed apertures, which form a differential pumping stage between the gas cell chamber and the rest of the beamline. The apertures can also be used for coarse alignment and reduce the IR intensity. The rest of the IR radiation is blocked after the apertures by a 150 nm thick aluminium foil supported by a Ni mesh (Luxel Corp.) to protect the entrance slit of the monochromator and prevent the grating from heating. The measured transmission of the Al filter at 35.6 eV is about 50 % and rises with higher photon energies. It is mounted on a CF40 gate valve, which aids the differential pumping of the beamline and can be opened for alignment with the IR beam or a co-propagating HeNe laser beam. As Fig. 4.2 shows, after the Al filter, the XUV beam is focused at the entrance slit of the monochromator by a grazing-incidence toroidal mirror (Winlight). Located 1 m from the gas cell with a 500 mm focal length, the mirror relays a 1:1 image of the HHG source to the monochromator entrance slit. The monochromator grating relays an image of the entrance slit to the exit slit, and the second identical toroidal mirror images the monochromator

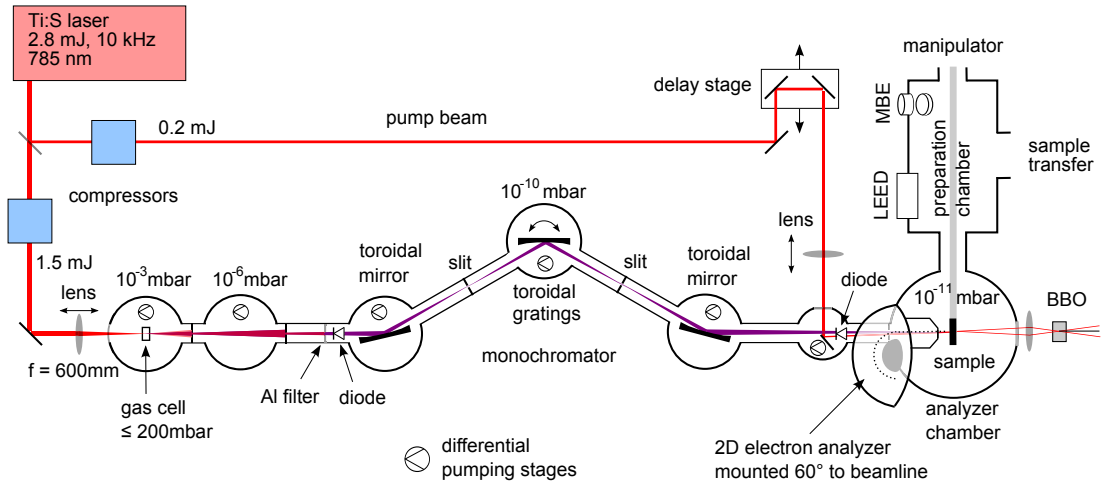

Figure 4.2: *Layout of the IR-pump – XUV-probe tr-ARPES experiment. Approximately 90 % of the Ti:S laser output is used for HHG, while the remaining 10 % is used for pumping the sample. Both beam paths have their own computer-controlled compressors for pulse duration control and a λ/2 - plate in combination with a polarizer for power control. HHG occurs in the gas cell, typically in Ar. XUV sensitive photodiodes are located just after the Al filter and after the second toroidal mirror. The IR pump beam is introduced into the beamline after the second toroidal mirror. A BBO crystal behind the analyzer chamber is used to find the temporal overlap of the pump pulse and an IR pulse allowed to pass through the beamline.*

exit slit onto the sample.

The monochromator itself is a customized Jobin-Yvon JY-VTM-EUV toroidal grating monochromator (entrance arm length 331 mm, exit arm length 320 mm) equipped with slits adjustable under vacuum for photon energy and bandwidth selection. The monochromator houses the two custom-made laminar toroidal gratings, which can be exchanged under vacuum.

Following the design of large grazing-incidence mirrors in synchrotron beamlines, we use a five-axis, six-strut arrangement with well proven reliability to support and adjust the two toroidal mirrors [130]. The chambers housing the optical elements are on heavy granite blocks, and mechanically decoupled from the surrounding beamline by bellows. Together with the computer controlled monochromator, this ensures easy and reliable user operation of the beamline. For alignment purpose and for assessment of the harmonic photon flux, two XUV sensitive photodiodes (AXUV100, International Radiation Detectors Inc.) can be introduced into the beamline before or after the monochromator (see Fig. 4.2)

The vacuum chambers housing the mirrors and gratings are each pumped with a vibrationally-isolated turbo-molecular pump (Pfeiffer, TMU 261P), leading to effective differential pumping along the beamline. Together with an ion-getter pump attached to the last chamber we reach ultra-high vacuum (UHV) conditions with a base pressure of 10^{-10} mbar in the beamline and 10^{-11} mbar in the analyzer chamber.

4.1.3 The laser system

In order to minimize space-charge effects due to electron-electron repulsion in photoemission from solid surfaces (see Ch. 4.2), it is desirable to release approximately one electron into the spectrometer with each probe pulse. This calls for a high repetition rate laser source. On the other hand, HHG is typically and most conveniently achieved with $> 0.5\,\mathrm{mJ}$ pulses. This combination rapidly leads to high average power lasers. A reasonable compromise between repetition rate and pulse energy can be achieved with Titanium Sapphire (Ti:S) chirped-pulse amplifiers (CPA) running at 10 kHz and 1 - 2 mJ energy per pulse.

The laser chosen for our experiment is a commercial Ti:S CPA laser system (Red Dragon, Kapteyn Murnane Labs). The laser comprises a prism-compensated Ti:S oscillator running at 80 MHz followed by three helium-cooled multipass amplifier stages. Each stage is pumped at 532 nm by a 10 kHz Q-switched Nd:YAG laser (Photonics Industries, DM100-532) operating at 85 W. We have introduced a spatial filter (a 1:1 Newtonian telescope with a 200 µm diameter diamond pinhole at the focus) between the first and the second amplifier stage to avoid hot spots in the beam profile after the multipass amplifier. This incurs a power loss of $\approx 10\,\%$ but reliably avoids damage to the subsequent amplifier crystals. After two separate grating compressors in the pump and probe beam-paths with about 60 % transmission the laser delivers 17 W at 10 kHz 1.7 mJ/pulse) with a center wavelength of 785 nm and a pulse duration of 40 fs, as measured with frequency-resolved optical gating.

Approximately 10 % of the laser output is split off to excite (pump) the sample. It passes through a separate compressor, as shown in Fig. 4.2, allowing the pump pulse to be stretched to arbitrary durations without affecting the HHG process.

4.1.4 High-order harmonic generation

Since HHG is a highly nonlinear process, it is sensitively dependent on a number of experimental parameters. In addition to the laser wavelength, the pulse energy and duration, we must also optimize the beam profile, the focusing geometry, the interaction length and the gas pressure (and type).

To optimize focusing we tested different arrangements and found the best results using a lens with a focal length of 600 mm. The exact position of the focus is known to influence the harmonic generation efficiency through the Gouy phase [131], and its optimum depends on the pump pulse intensity and the gas pressure. For our experiments the best results were achieved by positioning the focus just behind the gas cell in the beam propagation direction, towards the monochromator (at 1.5 mJ, 40 fs, and 100 mbar argon). It is noteworthy that any form of astigmatism in the IR focus at this point significantly reduces the harmonic yield.

The optimum length of the cell depends on the laser intensity and therefore on the focal length of the lens, the laser pulse energy, and pulse length. We have tested a number of different types of gas cells with an interaction length between 2 and

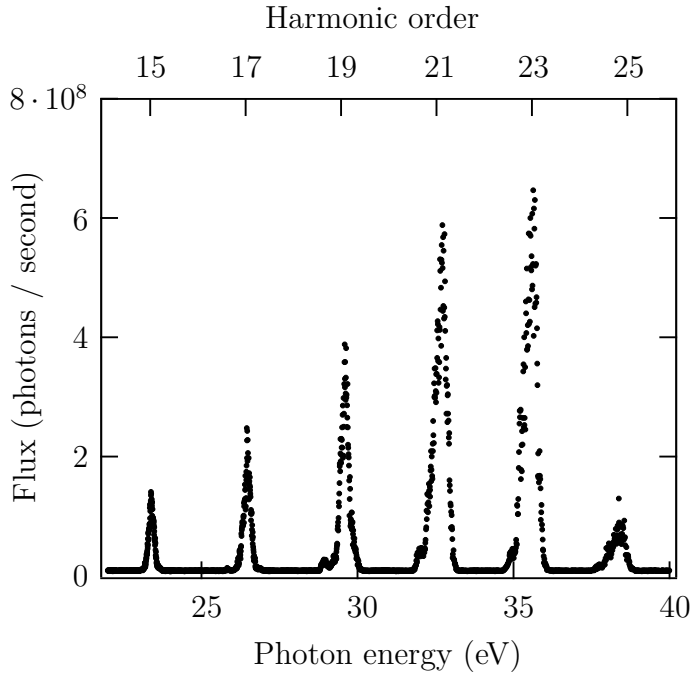

Figure 4.3: *A high-order harmonic spectrum generated in argon at 110 mbar by a 1.5 mJ, 40 fs pulse with a center wavelength of 785 nm. The spectrum was measured by recording the current from an XUV sensitive photodiode just before the sample position while scanning the monochromator grating. The slit size of the entrance and exit slits was adjusted for a monochromator resolution of 210 meV at harmonic 23. The FWHM bandwidth of harmonic 23 is 500 meV.*

15 mm with walls of stainless steel and copper between 20 - 200 µm thick. The best was found to be a simple stainless steel tube (⌀ 3×0.2 mm) with one end connected to the gas supply by compression fittings and the other flattened and folded over to seal it. The focused IR beam burns through the gas cell wall ensuring the holes have the correct diameter (≈ 150 µm) and are perfectly aligned to the beam.

The argon pressure for the gas cell is computer controlled (MKS 640) and can reach up to 200 mbar. The tuneability of this pressure is important since it has a strong influence on the spectrum of the generated harmonics. Depending on the laser intensity we have found an Ar pressure of 50 - 100 mbar to give the highest harmonic yield. During operation the pressure outside the cell stays below $5 \cdot 10^{-3}$ mbar, corresponding to a pressure gradient of about five orders of magnitude, due to the small holes in the cell walls. The gas cell chamber is pumped by a turbo-molecular pump (Pfeiffer TMU 512P 500 l/s) backed by a piston pump (Leybold Ecodry M15).

Many parameters of the beamline that must be optimized are controlled by a lab-written software: the gas cell pressure, the grating separation of both compressors (and therefore the IR pulse lengths), the power of the pump and HHG drive pulses and monochromator grating angle, i.e. the XUV wavelength of the probe pulse. The pump and HHG drive IR pulses are characterized and optimized before each experiment using frequency-resolved optical gating. A typical XUV spectrum using the optimized parameters described above is shown in Fig. 4.3.

4.1.5 ARPES endstation

The endstation comprises three chambers separated by gate valves (see Fig. 4.2): A μ-metal analyzer chamber (VG Scienta), a sample preparation chamber and a sample garage.

The μ-metal chamber reduces the earth's magnetic field to values below 50 nT. It houses a hemispherical display-type photoelectron analyzer (Specs Phoibos 100) for ARPES. We use a peltier-cooled camera (PCO, sensicam qe) to monitor the count rates. This guarantees negligible thermal noise relative to the CCD readout noise, thus enabling measurements with exposure times of up to several minutes at each pump probe delay. To calibrate the count rate we operate the camera with a short exposure time and high readout repetition rate, which makes it possible to count single electrons. The analyzer chamber is pumped by an ion getter pump and a titanium sublimation pump, in addition to the turbomolecular pump on the preparation chamber. A further getter pump attached near the electron detector ensures low presssure throughout the analyzer. Together with the differential pumping along the beamline, these pumps allow a routine base pressure of 10^{-11} mbar, thus fulfilling the special vacuum conditions required for the study of bulk and surface electronic structures of reactive samples such as lanthanide metals.

The preparation chamber is designed for sample growth and characterization. It houses a LEED device, a sputter gun, a quadrupole mass spectrometer, a coil with an iron core to magnetize samples, gas inlets, a quartz balance for monitoring the sample growth and evaporators for molecular beam epitaxy. Attached to the preparation chamber is a differentially pumped double stage load-lock and sample garage. They facilitate quick sample exchange without breaking the vacuum in the main chambers.

A cryogenically coolable sample manipulator (Vab GmbH) carries two different samples between the preparation and analyzer chambers on a copper extension built in-house. A fixed W(110) single crystal, as a substrate for the growth of thin-film samples such as Gd, and a holder for exchangeable samples. Both samples can be heated by electron bombardment. The tungsten crystal can be heated to 2100 K while its temperature is monitored by a type C thermocouple inserted into a small hole drilled in the side of the crystal. The temperature of the exchangeable sample is measured with a type K thermocouple. In addition the temperature of the whole manipulator head is monitored by type E thermocouple to prevent overheating of the copper parts when heating with a built-in Thermocoax heater.

4.1.6 ARPES: beamline energy resolution

We have performed a number of experiments specifically to test the performance of the beamline against its design specifications. Both, a high energy and temporal resolution is needed for the magnetization experiments in Ch. 5 and 6. As stated above, the bandwidth of a single harmonic at a central energy of 35.6 eV generated by a 30 - 40 fs IR pulse is typically 500 meV. Since for a monochromator grating

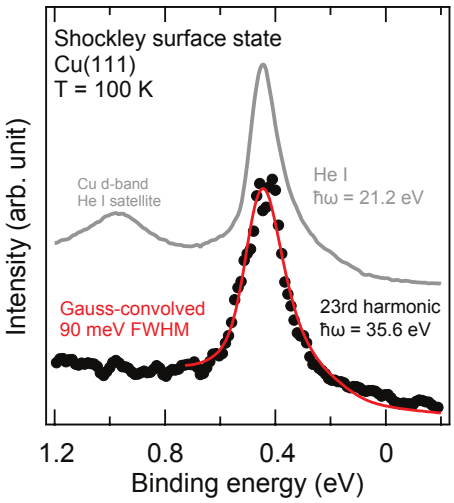

Figure 4.4: *Photoelectron spectra of the Cu(111) surface state at 100 K measured with the He I_α line at 21.2 eV photon energy (top) and with high-order harmonic radiation at 35.6 eV (bottom) with comparable analyzer settings. The broad peak at ≈ 1.0 eV binding energy stems from the Cu d-band excited with the He-I satellite. The He I_α data is limited by the analyzer resolution. The solid red line is a convolution of these data with a Gaussian (without the satellite), which gives an energy bandwidth of 90 meV (FWHM) for the high-order harmonic radiation.*

with a given line density and beam size the convolved widths of the entrance and exit slits determine the transmitted photon bandwidth, to reduce this to 150 meV the monochromator slits must be closed to typically 20 µm.

To measure the overall energy resolution of the experiment, we turn to the well known surface state of the Cu(111) surface. Following cycles of Ar^+ sputtering and annealing to prepare the Cu surface, we performed ARPES measurements using He I_α radiation from a discharge lamp and compared the results to ARPES with the 23rd harmonic ($\hbar\omega = 35.6$ eV). The spectra in Fig. 4.4 were obtained by integrating the ARPES data over 0.1 $Å^{-1}$ range of $k_{||}$. Since the linewidth of radiation from the He lamp is a few meV, the observed linewidth of the surface state is dominated by the intrinsic resolution of the electron analyzer. For the data recorded with XUV from HHG the observed linewidth is then a convolution of the monochromator energy resolution (i.e. the XUV bandwidth) and the analyzer resolution. We are therefore able to use this measurement to establish the monochromator resolution for 10 µm slit size, which was found to be approximately 90 meV at 35.6 eV photon energy.

4.1.7 XUV photon flux

The XUV flux depends on many parameters of the HHG process, but for our experiments, where better energy resolution is desirable, the monochromator plays a dominant role. To achieve the resolution discussed above, we must forgo considerable flux. While this may appear to be a limitation, high fluxes lead to space-charge distortion of ARPES spectra (see discussion below). For the 23rd harmonic at 35.6 eV with the XUV photon bandwidth set to 150 meV, we typically have a flux of $3.6 \cdot 10^7$ photons/second reaching the sample. This leads to approximately one electron *detected* per XUV probe pulse and space-charge distortion from the XUV can be neglected.

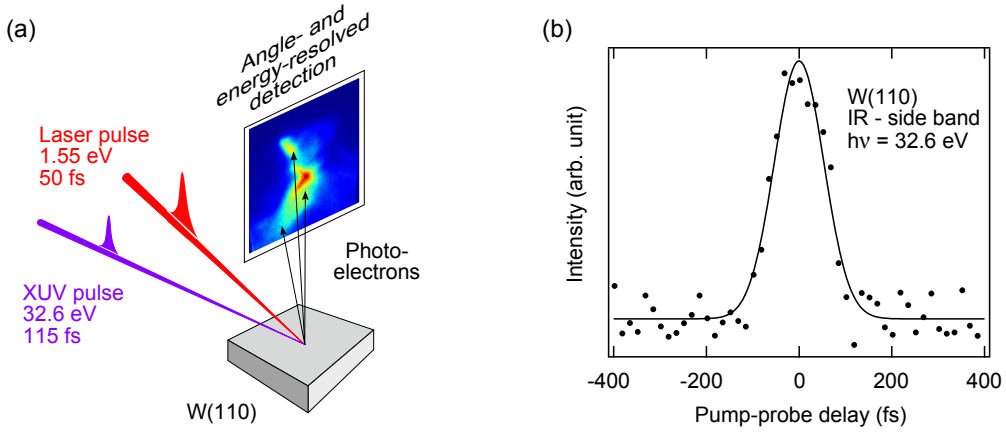

Figure 4.5: *(a) IR pump - XUV probe arrangement for tr-ARPES. The IR and XUV beams impinge on the sample with a small angle between them in the horizontal plane ($\angle_{IR\text{-}XUV} \approx 1°$). The incidence plane forms an angle of 60° to the surface normal. Photoelectrons are detected along the surface normal. (b) Cross-correlation measurement between 50 fs IR and XUV at 32.6 eV. The monochromator was set to 150 meV photon-energy resolution. The vertical axis shows the population of electrons lifted transiently above the Fermi level of the W(110) crystal by side-band formation. It gives a cross-correlation of the IR and XUV pulses, which is fitted to a Gaussian of FWHM 125 fs (solid line). Deconvolution from the IR pulse yields an XUV pulse duration of ≈ 115 fs FWHM.*

4.1.8 Time-resolved ARPES: time resolution

For time-resolved photoemission studies the spatial overlap of the pump and probe beams is critical. To achieve this, we image the XUV and IR spots on a phosphor-coated plate in the exchangeable sample holder with a high resolution camera. This also allows the IR and XUV spot sizes to be measured.

Temporal overlap between the IR and XUV is achieved by crossing an attenuated IR beam that has traveled along the beamline with the attenuated pump beam in a β-barium-borate (BBO) crystal (see Fig. 4.2). To allow the fundamental to traverse the beamline, the Al filter is removed, and the monochromator grating set to zero order. Both pump and probe beams then pass through the analyzer chamber and out of a window, and are then focused into the BBO crystal at a small angle. The pump-probe delay is then scanned until a second harmonic signal from the crossed beams is observed spatially located between them. Even though the pump and probe beam paths are 10 m long after their separation, we could not observe jitter in the pump probe delay within the time resolution of 125 fs given by the XUV pulse length.

Having found the pump-probe spatial and temporal overlap we can perform tr-ARPES to evaluate the temporal resolution. Cut to 150 meV, the bandwidth at 35.6 eV would support a transform-limited pulse duration of approximately 12 fs FWHM, assuming a Gaussian spectrum. The broadening of the XUV pulse by the monochromator was calculated to be in the order of 100 fs, as discussed

above and shown in Fig. 4.1 (c). To measure the actual XUV pulse duration, we performed a time-resolved ARPES measurement on the W(110) crystal in the geometry shown in Fig. 4.5 (a). The crystal was pumped by a *p*-polarized 50 fs IR pulse and probed with the XUV at 32.6 eV. In the proximity of the sample surface, outgoing photoelectrons excited by the XUV can exchange energy with the electric field of the IR pulse. The exchanged energy is a multiple of the IR photon energy, leading to the formation of sidebands in the photoelectron spectra [132, 133]. The sideband amplitude as a function of time is shown in Fig. 4.5 (b), and represents a cross-correlation function between the IR and XUV pulses from which the XUV pulse duration can be recovered [134]. This measurement indicates that our XUV pulse duration is approximately 100 fs, giving an overall time resolution for pump-probe experiments of 125 fs FWHM.

4.2 Space-charge effects in tr-ARPES

Space-charge distortion of ARPES spectra occurs when a cloud of low-energy electrons is formed at the sample surface, either through secondary electron generation from scattered XUV-excited high energy electrons, or by IR-excited electrons just above the vacuum level. The outgoing photoelectrons experience acceleration by the electric field of this cloud that is dependent on their emission time and energy. This leads to energetic shifting and broadening of the photoemission spectral features and is thus a severe restriction for measurements with already moderate resolution. Space-charge is known to be a problem in time-resolved photoemission studies from solid surfaces, especially for experiments with high pulse energies, typically at low repetition rates [133, 135, 136].

We observe space-charge effects in our experiment from both the IR and XUV excitation, and both can significantly distort the spectra. Fig. 4.6 (a) shows the effects of space-charge generated by photoelectrons excited by the XUV pulse. The data are extracted from changes in the width and energetic position of the gadolinium surface state as a function of the XUV flux. As shown in the figure, XUV space-charge effects become observable when the flux from the monochromator is higher than $\approx 10^4$ photons/pulse ($\hbar\omega = 35.6$ eV). With our usual fluences of ≤ 4000 photons/pulse XUV space-charge effects can be neglected. As Fig. 4.6 confirms, XUV space-charge distortions are approximately linear over a wide fluence range [135]. At a flux of about 10^5 photons/pulse the XUV induced space-charge shifts the spectrum by 200 meV, and is accompanied by a decline of the energy resolution by an additional 300 meV FWHM. Broadening of the spectra by XUV space-charge comprises three effects: first the acceleration of the electron by the space-charge cloud which depends on the emission velocity, second the emission time[1] within the XUV pulse length, and third pulse-to-pulse fluctuations in the HHG process which alters the magnitude of the first two since in the data recording process we would integrate over spectra that have experienced different energy shifts. It is for this reason that the broadening in Fig. 4.6 (a) is larger than the energetic shift, in

[1] With a 100 fs XUV pulse the distance between fist and last emitted electron is on the order of 300 - 350 nm for a kinetic energy of 26 - 35 eV.

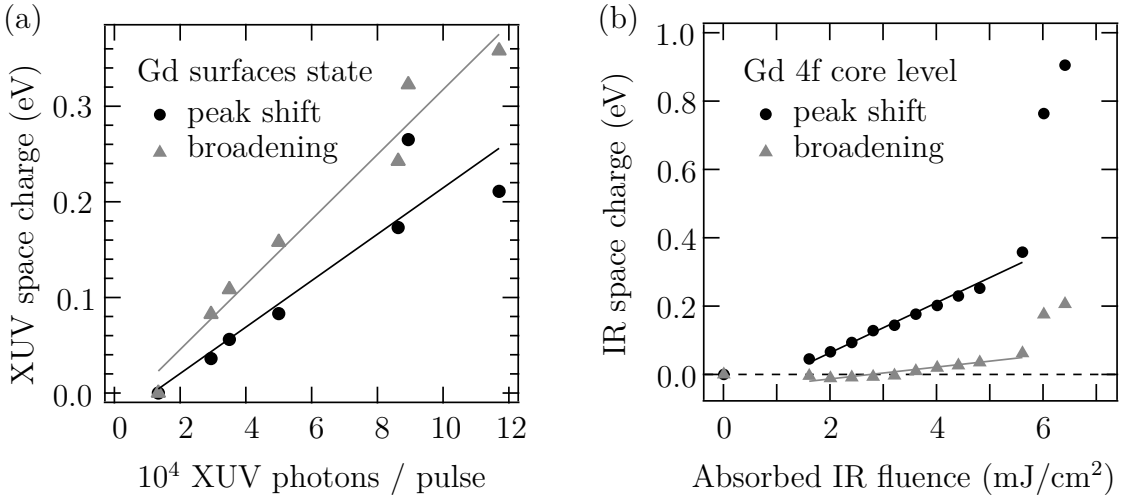

Figure 4.6: *Space-charge shift (circles) and broadening (triangles) of the spectra as measured from changes to the Gd(0001) surface state and the Gd 4f core level. (**a**) Probe pulse space charge of the harmonic radiation. (**b**) The contribution of the IR pump pulse depends on the pump-probe delay. The data shown here is recorded at 4 ps pump-probe delay where it reaches a maximum.*

contrast to the equivalent results for IR-induced space-charge distortions, which are discussed next.

Space-charge distortion from electrons excited by the IR pump pulse is more complicated because it is delay-dependent. In dynamical spectra its compensation requires a spectral feature that does by its nature not move. In our Gd(0001) measurements the 4f level, with a binding energy of 8.2 eV, cannot be excited by the IR pump pulse. The extent of the IR space charge is shown in Fig. 4.6 (b) as a function of absorbed fluence[2]. The chosen pump-probe delay was 4 ps since the space-charge shift reaches a maximum at that delay. At low fluences there is a linear increase in the peak shift and a small linewidth broadening with a sudden rapid increase at about 6 mJ/cm^2. To excite an electron from the Fermi energy to the vacuum level requires, for Gd with a preparation-dependent work function of 3.0 - 3.7 eV, at least two 1.6 eV photons, so this curve can be interpreted as a non-linear increase in multi-photon absorption.

Figure 4.7 shows the time dependence from -1 to 500 ps pump-probe delay for an absorbed fluence of 3.5 mJ/cm^2. Besides the large drop at longer timescales > 10 ps, the shift changes significantly when going from negative to positive pump-probe delays. In the case of negative delays the *space-charge cloud* (SCC) is generated after the probed electron has left the surface of the solid leading to a shift of the spectrum towards higher kinetic energies since the probed electron is accelerated by the electric field of the SCC behind it. The shift depends on the surface quality and the laser fluence, and is usually in the order of 200 to 300 meV in gadolinium. At, and just after t_0, the shift does not change. At positive pump probe delays

[2]The absorbed fluence in Fig. 4.6 (b) differs from what was published in [III], because of an error in the determination of the spot size. Note, however, that space charge depends strongly on the surface quality of the sample and can differ by a lot.

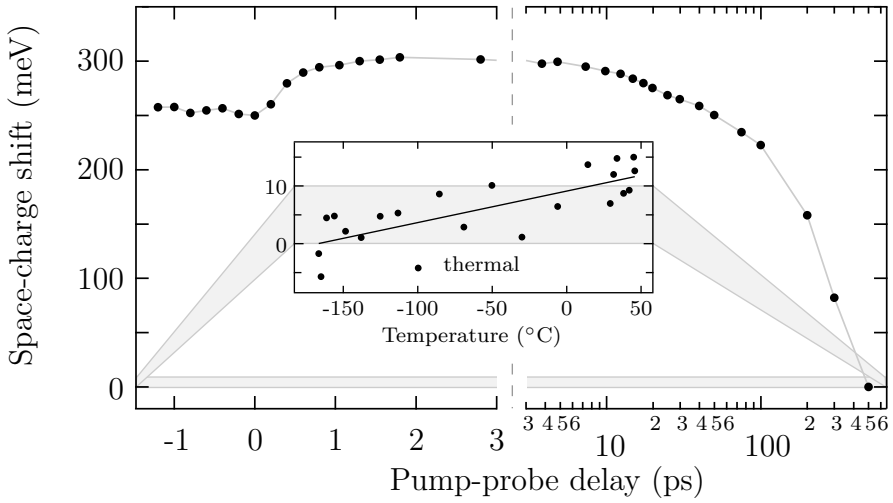

Figure 4.7: *Position of the Gd 4f level as a function of pump-probe delay. The shift originates from space charge induced by the 300 fs IR pump pulse and has to be subtracted from the band positions measured by tr-ARPES. The absorbed fluence is 3.5 mJ/cm². At 500 ps pump-probe delay the IR-induced space charge has decayed.* ***Inset:*** *Position of the 4f photoemission line as a function of temperature. It was measured using He I_α radiation to exclude XUV space charge. Thermal expansion of the lattice leads to a shift in the order of 5 meV/100 K and can be neglected. Gray stripes indicate a shift of 10 meV for better comparison of thermal vs. space-charge shift.*

the spectrum shifts to even higher energy. This shift persists until about 40 ps where it is back to the level before t_0 and decreases further up until about 500 ps where pump induced space charge is basically decayed. The explanation of delay-dependent space charge is quite complicated and has contributions from different origins. First of all, the effect changes after t_0 since at positive pump probe delays > 0.3 ps the electron has to travel through the already generated electron cloud. In the case of a static SCC the electron would first be decelerated while overcoming the potential of the cloud and then accelerated by the same amount. However, the effect is much more complicated since the interaction of the electron cloud and the detected photoelectron is dynamic. Part of the SCC is also leaving the surface in the direction of the analyzer. The probed electron which was decelerated while piercing through the SCC is now *surfing* on the high energy tail of the SCC potential leading to a longer exchange in kinetic energy. The electron could therefore be shifted to even higher energies, decelerating the SCC behind it. Even though possible, this effect seems to be unplausible since – in our measurement – the electrons of the SCC have a much lower kinetic energy than the detected ones. A more reasonable explanation of the shift around t_0 involves the temperature dependency of the work function. In Gd, heating of the lattice results in a reduction of the work function of about 0.4 meV/K [43]. This leads to an expected reduction of the work function from 3.72 eV to about 3.60 eV. It is somewhat puzzling, that this change should have such an influence on the observed IR space charge, because in both cases one needs at least three IR photons for the emission of electrons ($\hbar\omega = 1.6$ eV). In addition, the delay-dependent IR space charge can be influenced

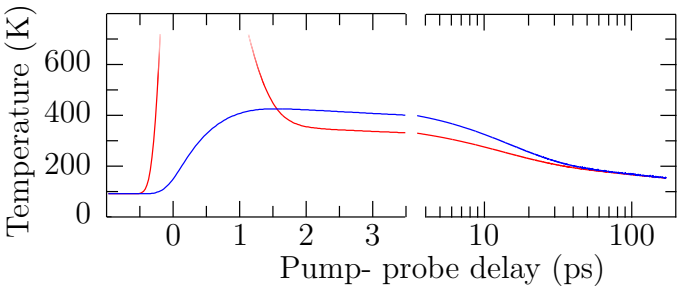

Figure 4.8: Calculated sample temperature after IR excitation. *The electron (red) and the phonon temperature (blue) as a function of pump-probe delay for an absorbed IR fluence of 3.5 mJ/cm^2 (300 fs pulse length). The electron system is excited and reaches a maximum temperature of about 2300 K. Subsequent electron phonon scattering lead to a thermal equilibration with a lattice temperature of 400 K. The slight mismatch between the two temperatures from 1.5 to 40 ps is due to the higher heat conductivity of the electrons. This calculation was done by S. Wienholdt and coworkers using the E3TM.*

by the secondary electrons from the XUV pulse. A conclusive description, that takes all these effects into account, is still lacking.

To compensate space charge-effects we need to make sure that we can neglect static shifts of the bands due to the changing lattice temperature. To this end, we measured the binding energy of the Gd 4f state without IR radiation as a function of temperature. Thermal expansion of the lattice only leads to a shift of about 5 meV/100 K (see inset in Fig. 4.7). The calculated maximum lattice temperature for $F_{abs} = 3.5\,\mathrm{mJ/cm^2}$ is 292 K [137] which corresponds to a thermal shift of 10 meV. In this calculation, the low lattice temperature is a consequence of the high magnetic heat capacity at the Curie temperature [71]. A more careful analysis however needs to take the remarkably slow 4f demagnetization[3] into account, since the 4f spin order is mainly responsible for the magnetic heat capacity. Such an analysis is shown in Fig. 4.8 and gives a maximum lattice temperature of about 400 K which corresponds to a still small thermal shift of 15 meV. Note that the residual exchange splitting is not a good measure of the lattice temperature at ultrafast timescales. For this dataset its minimum value is 640 meV which would correspond to a temperature of only 200 K [42] in contrast to the calculations. Besides the arguments given above, the space-charge origin of the shift becomes evident if compared to the dynamics seen in Tb. Due to its higher work function IR space charge is much smaller there and can be neglected.

We therefore correct all time-dependent spectral shifts to those of the 4f level to eliminate IR space-charge shifts. This way we can be certain that space-charge effects are not responsible for the dynamics discussed in Ch. 5. Figure 4.9 shows an example of such a corrected dataset. It includes the binding energies of the surface state and exchange split valence bands as a function of pump-probe delay before (circles) and after (dots) the correction. It should be noted that the corrected positions in the quasi-static region after about 2 ps pump-probe delay coincide

[3] This is discussed to its full extend in Ch. 6 (page 85 ff.).

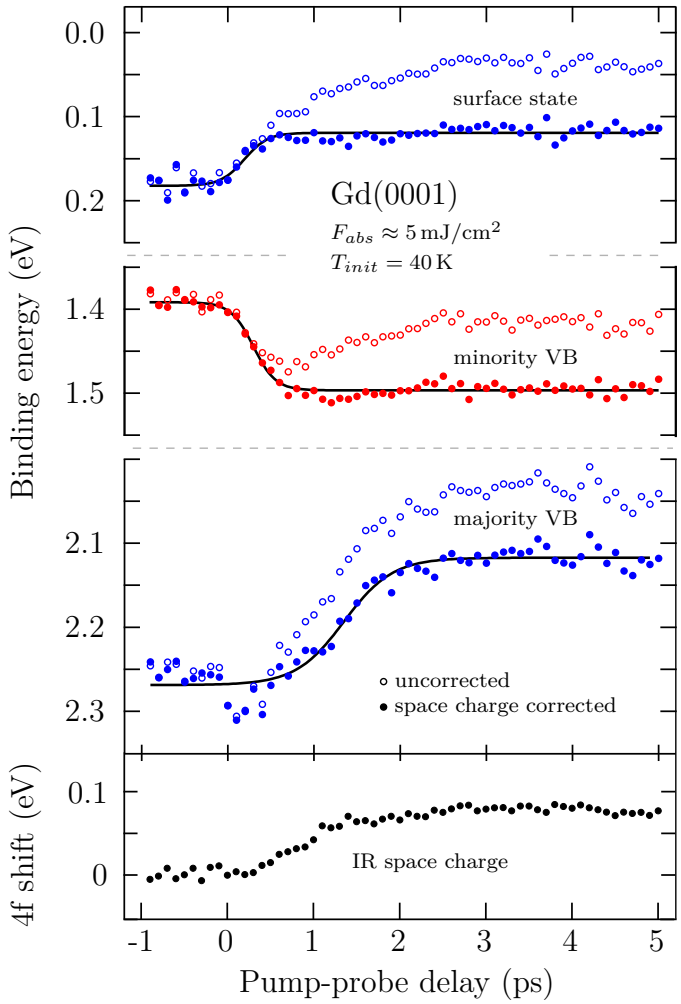

Figure 4.9: Gd band positions corrected and uncorrected as a function of pump-probe delay. *Circles show the energetic positions of the states without the inclusion of time-dependent space-charge effects. Dots mark the band positions after correction to the 4f state. The 4f shift (black dots) is normalized to the value before t_0. The solid lines are sigmoid fits and serve as a guide to the eye.*

with the binding energies known from static measurements for the corresponding valence band exchange splitting [42]. Since Gd has a work function of 3.7 eV only multi-photon absorption can lead to IR space charge. This puts an upper limit on the IR intensity we can employ to demagnetize the sample if we are to retain sufficient energy resolution. Thus a balance must be struck between time resolution and pump pulse fluence: a shorter or longer pulse duration with less or more pulse energy respectively.

4.3 Sample preparation

Lanthanide metals are extremely reactive, which makes the investigation of pure single crystals challenging. Even under UHV condition with a base pressure below $2 \cdot 10^{-11}$ mbar a clean sample is affected by adsorbates within a few hours. The preparation of well-defined samples thus requires special attention. Since clean bulk single crystals of Gd and Tb are almost impossible to prepare [138], one is restricted to the study of thin films grown by molecular beam epitaxy. Tungsten was found to be a good choice of substrate, because it is easy to handle and has a high melting point, which is necessary to stand the high temperatures during heating; but mainly because Tb and Gd grow as high quality films on the (110) surface of tungsten [139]. This has several reasons: the pseudo-hexagonal W(110) surface matches to the (0001) surface of Gd and Tb quite well, in fact the lattice mismatch is found to relax within five monolayers and they grow thereafter with their own lattice constant [140]. Another advantage is the high surface energy of W(110) which favors a layer-by-layer growth of the lanthanides and prevents the formation of intermetallic alloys.

4.3.1 The substrate

A clean substrate is crucial for a good growth of the lanthanides. The commercially available tungsten samples are contaminated with carbon, and need to be treated before usage as a single crystal substrate. Carbon impurities tend to diffuse to the surface and form a superstructure, which interferes with the epitaxial growth of the lanthanides. The first step of sample preparation is therefore the removal of carbon atoms. Since it is hardly possible to clean the whole crystal, one is restricted to purify the uppermost layers, which is sufficient. The cleaning is done by heating the crystal in an oxygen atmosphere, to oxidize the carbon. Carbon-oxides are weakly bound to the tungsten surface and already desorb during that process if heated over a critical temperature. Depending on the condition of the bought sample this cleaning process can be quite time-consuming (50 - 300 h).

Many studies have been published concerning the best procedure to clean tungsten, e.g. [141–143]. We have tried several methods and get the best result by heating the sample up to 1800 K in an oxygen atmosphere of $5 \cdot 10^{-8}$ mbar followed by a short *flash* up to 2100 K under UHV condition to force the stronger bound tungsten-oxides to desorb. The duration of one heating cycle depends on the purity of the sample. If the sample is relatively clean it is enough to heat it once for 10 minutes before flashing, while a strongly contaminated sample should be alternately heated for one hour then flashed. One has to determine the quality of the sample to consider further steps of preparation. Since both, LEED and ARPES are highly surface sensitive techniques, they are both suited to testify the sample quality. Figure 4.10 shows the LEED picture and corresponding ARPES spectrum of the sample at each step of a cleaning cycle.

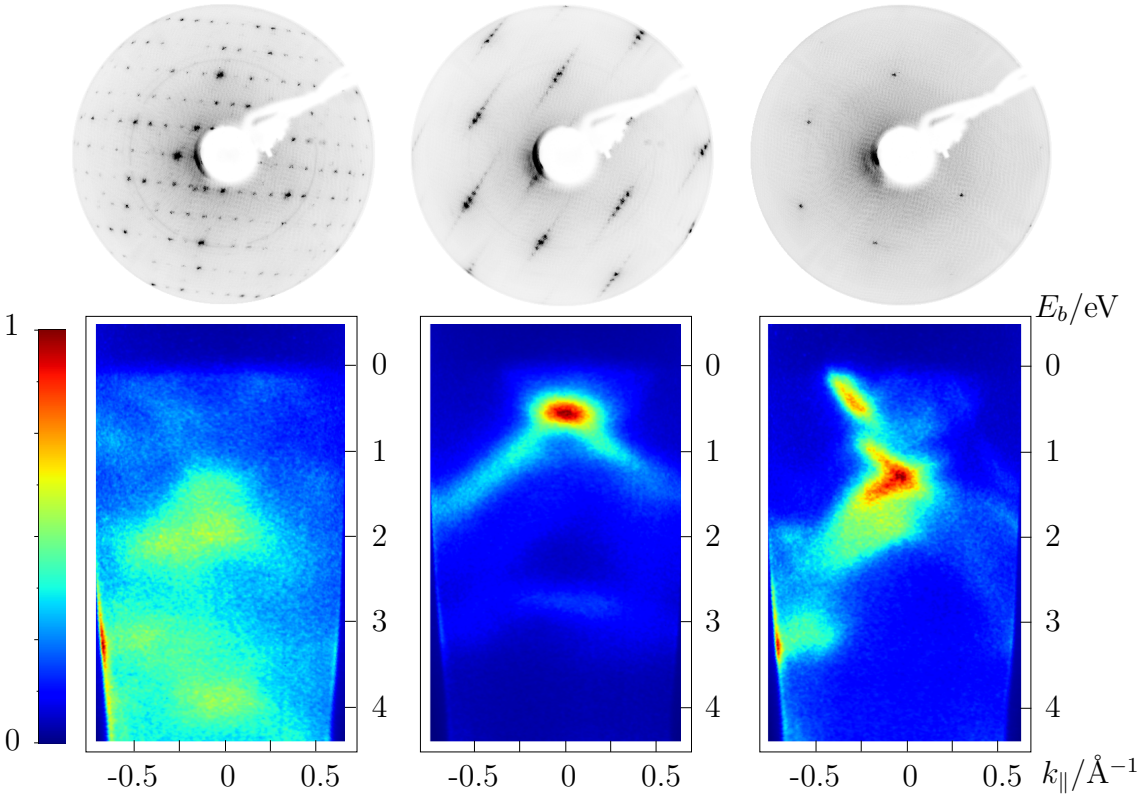

Figure 4.10: *Preparation of the tungsten (110) substrate. LEED pictures and the corresponding band structure in a false-color plot (intensity scale on the left side). The LEED pictures are taken at 160 eV kinetic energy. On the left a contaminated tungsten sample is shown. The superstructure in the LEED picture is formed by carbon atoms. In the middle one can see the influence of oxygen after heating the wafer to 1800 K in an oxygen atmosphere $p = 5 \cdot 10^{-8}$ mbar. After flashing the oxygen heated sample up to 2100 K we get the clean W(110) substrate, which is shown on the right.*

4.3.2 Epitaxy of the lanthanides

Films of 10 nm thickness ($\approx$ 35 monolayers) were found to be suitable to study the magnetic behavior of Gd and Tb [29, 42, 105]. They are thin enough to have their easy axis in plane and grow layer-by-layer, yet are thick enough to neglect the influence of the tungsten substrate and show electronic bulk behavior [42]. Films of a thickness of 25 nm and more have the problem that the lanthanides begin to form islands.

For the epitaxial growth of the lanthanides we use self-made evaporators, consisting of a tungsten crucible which is filled with 99.99% pure Gd or Tb. The crucible is heated by electron bombardment from surrounding tantalum filaments. This setup is enclosed by a tantalum shield, which blocks the hot electrons and prevents the molecular beam from evaporating onto critical parts of the manipulator and vacuum windows. The temperature of the crucible is controlled by an applied positive bias. Since the evaporation rate has an influence on the quality of the films we choose a well established rate of about 0.5 nm/min [29]. The evaporation

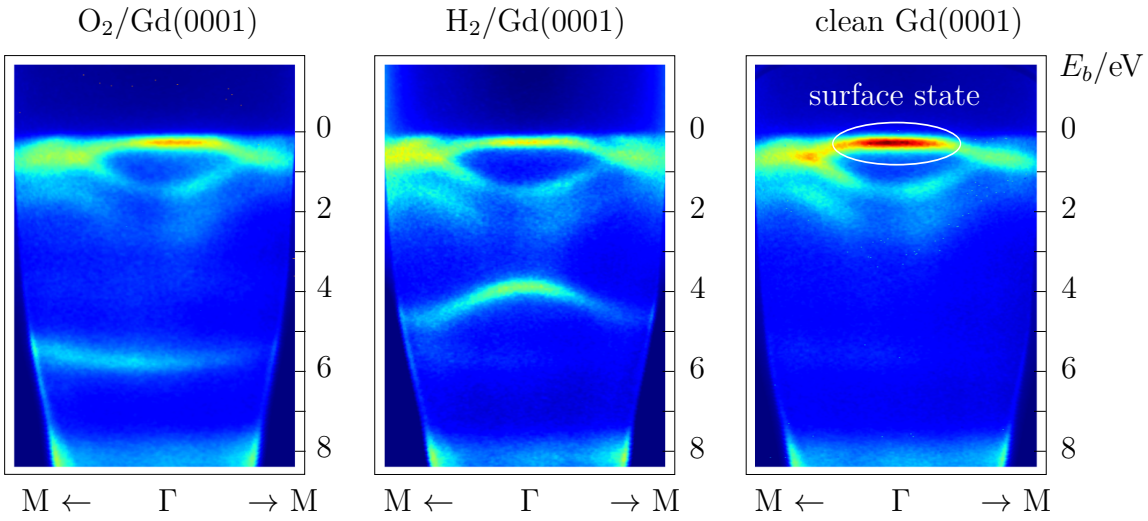

Figure 4.11: *ARPES spectra of the two most common impurities of a Gd sample in UHV. The main impurities of Tb are the same. In the left spectra the sample is contaminated with oxygen adsorbates. In the middle with hydrogen adsorbates. For comparison the spectrum of a clean Gd sample is shown on the right. Note that the intensity of the surface state is strongly influenced by the presence of adsorbates.*

rate and the film thickness are measured *in situ* by a quartz balance. It has proven useful to flash the sample immediately before the evaporation process, to remove interfering adsorbates.

Once grown, the sample needs to be annealed to allow the atoms to align and heal lattice defects. The annealing temperature is dependent on the film thickness [144] and differs considerably between Tb and Gd. We did several measurements to find the best annealing temperature for our 10 nm films and found 680 K to be suitable for Gd and 880 K for Tb.

Through residual gas in the vacuum chamber and the good getter properties of the lanthanides, the surface can be rapidly covered by adsorbates. The different types of adsorbates have one feature in common: they interfere with the surface state, usually reducing its intensity in photoemission. The intensity of the surface state is therefore a very good indicator of the sample quality. Oxygen and hydrogen are the most common impurities, since hydrogen is hard to pump and oxygen can remain from the tungsten cleaning cycle. Figure 4.11 shows the typical spectra of these adsorbates. Note that the oxygen chemisorbs dissociatively, leading to a low dispersion and a narrow line width [145, 146]. It is therefore not surprising, that adsorbed oxygen interferes strongly with the surface magnetism [147].

Hydrogen also chemisorbs readily on the (0001) surface of Gd and Tb. The high dispersion of its band indicates that hydrogen retains its strong intermolecular binding. As with oxygen, the surface state decreases with increasing hydrogen adsorption, and there is also some evidence that the surface-magnetism changes [148].

Chapter 5

Itinerant electrons: tr-ARPES of Gd and Tb

Besides the technological importance of laser induced magnetization dynamics, pump-probe experiments offer deep insights into the underlying mechanisms. In the past various models have been suggested to explain the ultrafast transfer of angular momentum observed in experiments. For the magnetization dynamics of transition metals this can be achieved by simple models based on rate equations [4, 14]. The underlying mechanism thereby is believed to be electron-phonon spin-flip scattering via spin-orbit coupling. In addition it was pointed out that magnetization dynamics of itinerant electrons can be strongly influenced by superdiffusive spin transport due to the spin-dependent Fermi surface [17]. This is especially true for thin magnetic films and surface sensitive techniques. In combination, these two models were sufficient to explain the dynamics seen in Fe, Co, Ni and their layered combinations.

Both models, however, fail to explain the complex magnetization dynamics of lanthanides since they assume that the magnetic system stays in equilibrium, i.e. instantaneous intra-atomic exchange between localized 4f and itinerant 5d6s electrons. To investigate this subject we have chosen Gd and Tb thin films. Gd metal is, with the vanishing orbital angular momentum, a model Heisenberg ferromagnet and as such of great theoretical interest. Tb on the other hand, beside its technological importance, is an ideal comparative counterpart to Gd since it differs mainly by the additional 4f electron which gives rise to a strong angular orbital momentum of $L = 3$ and thus a strong spin-lattice coupling.

We use time-resolved photoelectron spectroscopy to investigate the magnetization dynamics in these metals, because it offers the unique opportunity for the simultaneous investigation of itinerant valence band magnetism via the 5d6s exchange splitting, and the localized 4f magnetic order via magnetic linear dichroism. In addition, we are able to separate surface and bulk magnetism through separate analysis of the occupied majority component of the exchange split d_{z^2} surface state and the valence bulk bands. Especially with regard to other techniques it is imperative to keep in mind, that on the ultrafast timescale the system is far from the thermodynamic equilibrium and that therefore the measured signal, contrary

to its static relation, does not necessarily reflect the magnetism of the sample, but can additionally be influenced by other transient nonmagnetic effects. This difficult issue is often not or not satisfactory addressed and can only be settled through ongoing and careful comparison of experimental results from complementary time-resolved techniques. Disentangling magnetic and nonmagnetic signals can be quite challenging because optical, phononic and electronic changes influence each other. In addition to this general problem there are also differences concerning the probed region for the different techniques. Some experiments probe primarily the surface layers, as they are limited by the escape depth of electrons (e.g. PES, STS). Other methods probe the whole bulk (e.g. XMCD in absorption geometry). Some signals are sensitive to the local magnetic order (e.g. the exchange splitting), others to macroscopic magnetism (i.e. to the averaged spin orientation in the probed region).

This makes interpretation difficult in time-resolved measurements, because one can not simply compare with static experiments. If, e.g. the exchange splitting changes upon laser excitation one can not assume that the polarization of the bands is the same as in thermal equilibrium for the same splitting [149]. Spin currents, depopulation of states, transitions resonant to the laser excitations and transient lattice strains in combination with magnetostriction will influence the signal without necessarily changing the overall sample magnetization.

In this chapter we will discuss the different magnetic signals obtained by tr-ARPES, first we have a look at the itinerant bulk magnetism which is mediated by the 5d6s valence electrons. To this end we follow the binding energy of the exchange-split valence band electrons as a function of pump-probe delay (Ch. 5.1) and discuss the outcome within the M3TM. After that we will further investigate the distinct ultrafast response in Gd on behalf of measurements with smaller time steps and better statistics and give an in depth interpretation of our result. Then we will test this interpretation by temperature-dependent measurements (Ch. 5.2) and compare the data with earlier MOKE measurements. Subsequent (Ch. 5.3) we also have a look at the pump fluence dependence of the dynamics. The response of the localized 4f electrons will be discussed in Ch. 6.

5.1 The exchange splitting of the 5d6s bands

The exchange splitting is commonly regarded as a direct measure of magnetism according to the Stoner model (cf. pp. 11 f.). The net magnetic moment is thereby defined by the difference in occupation of the spin polarized valence bands, and thus by the size of their exchange splitting at the Fermi edge. This model is especially useful for transition metals like Fe, Co and Ni in thermal equilibrium, where the size of the exchange splitting is determined by the coupling constant J_{ij} between the polarized 3d electrons and their density at the Fermi edge. Since J_{ij} depends on the distance between the electrons, it is also dependent on the distance of the corresponding lattice sites i and j which varies with the phonon temperature T_p. This dependence can lead to various thermo-magnetic effects such as magnetostriction as in the case of Gd or lead to an antiferromagnetic phase transition as in the case of Tb. Since we know that the bands are due to magnon

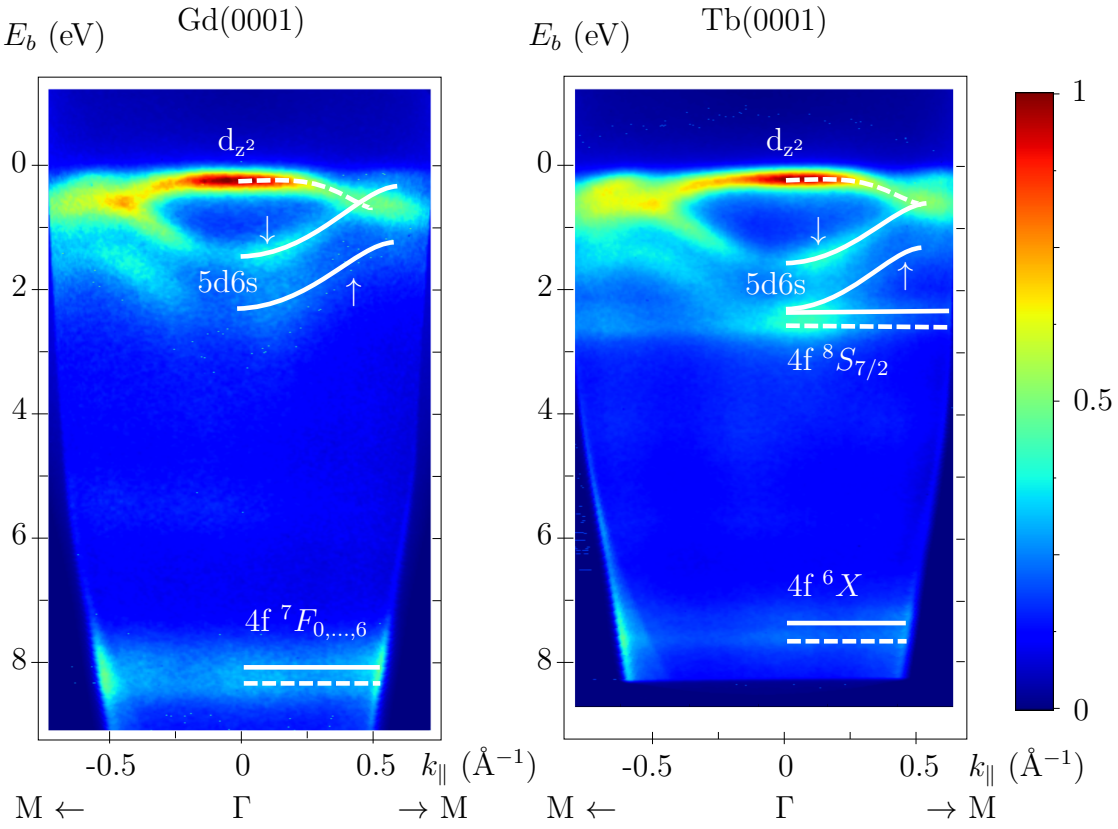

Figure 5.1: Gd and Tb spectra in the ferromagnetic phase at 90 K. *White lines guide the eye and mark bulk (—) and surface (---) states. At the used probe photon energy of 36 eV the high intense d_{z^2} surface state can be used as an indicator for the sample quality. The itinerant 5d6s electrons form the Δ_2 like valence bands are exchange split into minority (↓) and majority (↑) spin components. The final state multiplet of the 4f state has majority character and shows a surface core level shift. In Gd the whole multiplet lies around 8 eV while in Tb only the ^6X ($X = D, I, P$) can be found at this energy. The high spin $^8S_{7/2}$ component has much lower binding energy (≈ 2.5 eV) and overlaps with the 5d6s majority band at the Γ point.*

excitations not fully polarized at finite temperatures, it is evident that this also has an influence on the size of the exchange splitting[1].

In the rare earth metals Gd and Tb the size of the exchange splitting is influenced by yet another factor: the polarization of the 4f electrons and their intra-atomic coupling to the 5d spins, J_{int} [150]. In first approximation J_{int} will not vary with the lattice temperature, and in the case of Gd we can assume that any ultrafast dynamics of the exchange splitting is not driven by the polarization of the 4f electrons because they are not excited directly by the pump pulse[2] and couple only weakly to the lattice ($L \approx 0$, MCA = 0.03 meV).

[1] Magnon excitations lead to spin mixing where the eigenstate of a spin wavefunction has to be expressed by a superposition of spin up and spin down states: $(\alpha|\uparrow\rangle + \beta|\downarrow\rangle)e^{i\boldsymbol{kr}}$ [15].

[2] Occupied and unoccupied 4f states in Gd lie at 8 and -4 eV respectively [151] and thus unreachable by the pump-pulse energy of 1.6 eV.

In general, it can be stated that the exchange splitting is related to the magnetic order on the coherence length of the corresponding electrons. In metals the mean free path of the conduction electrons sets the upper limit for this length, and is usually on the order of a few tens of nanometers [17]. A rough estimation for the coherence length of itinerant electrons at the Curie temperature is given by

$$\ell \sim a\sqrt{w/k_B T_C} \tag{5.1}$$

with w the width of the band and a the lattice constant along the corresponding direction [152]. The band widths of the Gd 5d6s valence band along Γ - M are about $w \approx 3.5\,\text{eV}$ [24] leading to an estimated coherence length of $\ell_{\Gamma-M} \sim 37\,\text{Å}$ at T_C. From the dispersion of these bands along Γ - A we get, with the corresponding lattice constant, the coherence length perpendicular to the surface which is with $\ell_{\Gamma-A} \sim 29\,\text{Å}$ smaller. In contrast to these itinerant 5d6s bands the low dispersion of the surface state along Γ - M indicates in-plane localized Tamm-like character.

A reduction of the splitting thus indicates that the microscopic order is perturbed, either by spin mixing, polarization-dependent spin-flip scattering into the opposing channel or spin-dependent transport. That said, it is clear that the splitting will persist if averaging over several magnetic domains as long as the domain size exceeds the coherence length of the electrons and can therefore even be measured on "unmagnetized" samples, i.e. samples without macroscopic magnetic order. Additionally, by following the response of the minority and majority component of the 5d6s valence bands one has a signal of the bulk magnetization, since the above estimated coherence lengths assures a probing of the electronic structure about 10 layers into the bulk[3].

5.1.1 Spin mixing and Stoner behavior

Before we discuss the exchange splitting under non-equilibrium conditions let us have a look at the static case of thermal demagnetization. Fig. 5.2 shows the temperature dependence of the exchange splitting. There is a controversial discussion in literature if the splitting of the bulk bands follow the Stoner model and collapse completely or if there is a residual splitting above T_C as suggested by the fit in Fig. 5.2, the spin polarization will then be lost due to spin mixing of the bands.

Such a spin mixing behavior was fist found in the relatively localized d_{z^2} surface states of Gd and Tb [153, 154]. With increasing temperature its exchange splitting reduces only slightly and remains nearly constant above T_C, while the spin polarization reduces strongly and vanishes. In contrast, the itinerant 5d6s bulk bands were reported to follow the Stoner model with a complete collapse of the exchange splitting at T_C [26, 30]. Further measurements of the valence band structure with better energy resolution suggested a residual exchange splitting

[3] Not to be confused with the escape depth of the photoelectrons, which is about 2-3 layers at our photon energies. Even though the measured valence electrons stem from the topmost layers, they already show the complete bulk behavior because of their long coherence lengths. If this would not be the case, then their dispersion along the **c** direction could not be measured [29, 30].

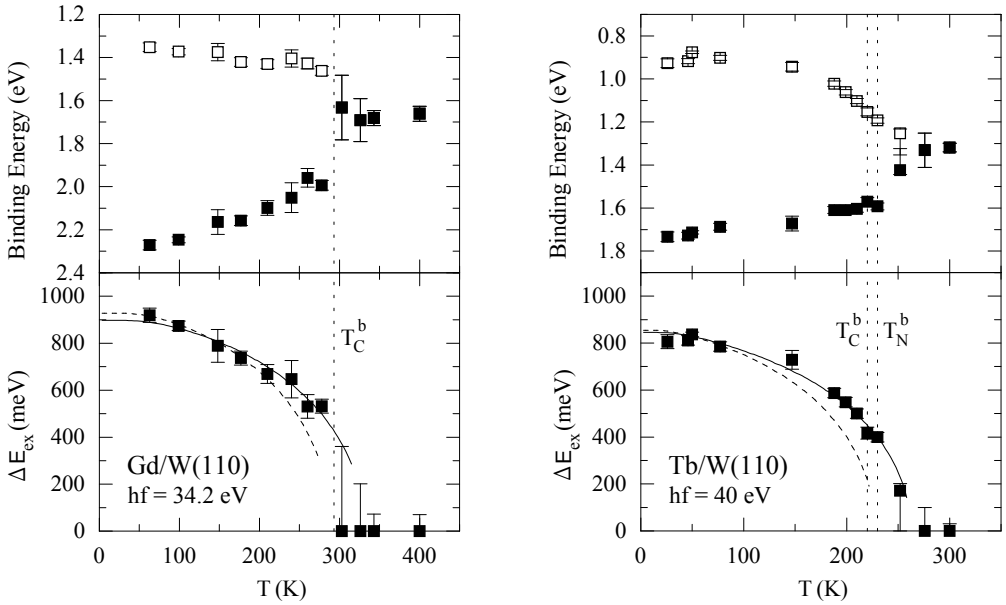

Figure 5.2: Temperature dependence of the 5d6s exchange splitting as measured by photoemission, from Ref. [42]. *The upper panel shows the binding energy of minority □ and majority ■ valence band components, left for Gd and right for Tb. Although not resolvable, a fit (solid line) of ΔE_{ex} suggests a residual exchange splitting above T_C. The dashed curve marks the expected magnetization using a Brillouin function with $J = 7/2$ in the case of Gd and $J = 6$ for Tb.*

which is not directly resolvable due to the intrinsic linewidth of the valence bands and thermal broadening. Subsequent spin-resolved experiments [155] supported these findings but were not able to measure the residual splitting directly since the spin polarization of these bands vanish at the Curie temperature. Heating the sample to even higher temperatures does not seem to influence the width of the 5d6s bands, i.e. the proposed residual exchange splitting, any further preventing a definite answer to this question within static techniques [42].

To settle this issue we performed a pump-probe experiment at 320 K which is 35 K above the Curie temperature[4] monitoring the width of the Gd valence band at the Γ point [IV]. We note that the width is not affected by pump-induced space charge (cf. Fig. 4.6 b). The result is shown in Fig. 5.3. The width of the fitted Gaussian changes within the length of the pump pulse and indeed shows a reduction $\Delta\sigma$ of 50 meV which corresponds to a residual exchange splitting of at least 100 meV at this temperature. This can only be explained by remaining short-range magnetic order which persists on the coherence length of the valence electrons. This interpretation is also supported by the massive residual exchange splitting of the surface state (400 meV at 350 K [153]) as its electrons are more strongly localized and therefore more sensitive to short-range magnetic order (cf.

[4]The Curie temperature of thin films is thickness-dependent and sensitive to the preparation method i.e. the deposition and annealing temperature. Temperatures that are too high will result in the formation of thicker Gd islands. An ideally prepared 100 Å thin Gd(0001) film has a T_C of 285 K, which is a bit lower than the bulk value of 293 K [35].

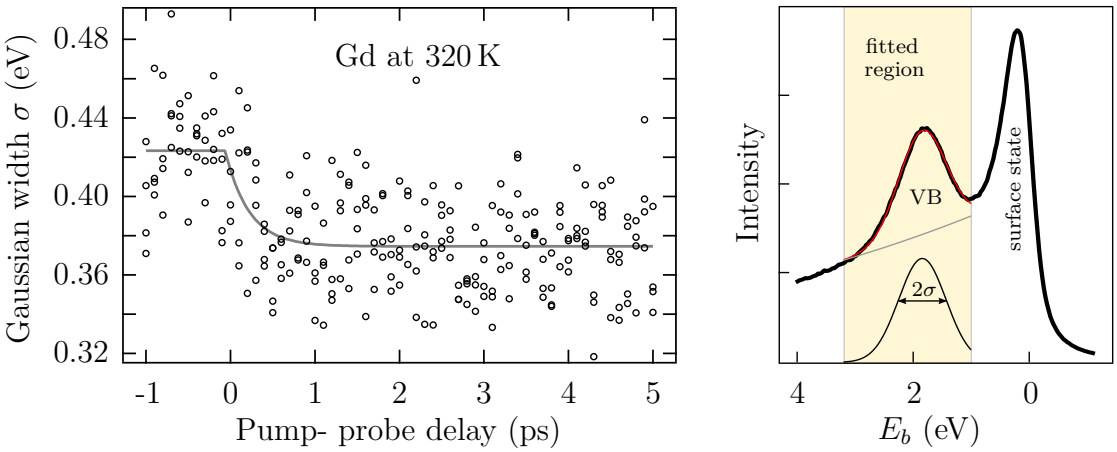

Figure 5.3: The valence band width of Gd at 320 K as a function of pump-probe delay. Left: *Even 35 K above the thin film Curie temperature ($T_C(100\,Å) = 285\,K$) the width of the valence band reduces upon laser excitation, suggesting a residual exchange splitting of about 100 meV. The solid line in this panel is a single exponential fit to the data and serves as a guide to the eye. In this measurement the 1.6 eV pump pulse is 300 fs long with an absorbed fluence of 4 mJ/cm^2. The spectrum is probed with 100 fs 36 eV photon pulses.* ***Right:*** *The fit of one random data point at negative delays is displayed. The energy distribution curve shows the spectrum at the Γ point (cf. Fig. 5.1 & 5.4). The with of the valence band is obtained by a fit with a Gaussian and an exponential background.*

discussion above). The fast time scale of the response indicates that the reduction of the residual splitting is thereby driven by spin transfer between microscopic regions of different magnetic ordering, rather than local spin flip excitations. Such nonlocal transport phenomena were also found to play a crucial role in the demagnetization of GdFeCo ferrimagnets [156].

The role of the surface It was brought forward by theory that the magnetism at the surface could differ significantly from the bulk behavior as a result of symmetry breaking at the vacuum interface (see e.g. [157–159]). Subsequently distinct surface magnetism was reported in Gd with an enhanced Curie temperature 22 to 60 K higher than the bulk value [26, 160–164]. Naively it could be argued that therefore enhanced surface magnetism is responsible for the massive residual exchange splitting of the surface state as well as the minor exchange splitting of the valence bands above the *bulk* Curie temperature. The subject of enhanced surface magnetism in Gd was further investigated, but the above mentioned results could not be reproduced by to other groups who reported an identical Curie temperature for the surface and bulk [144, 153, 155, 165, 166]. Among them Arnold and Pappas [165] pointed out some mistakes that might have been made in Ref. [160–162] regarding thermometry and the correction of instrumental asymmetries which could be the reason for the measured enhanced surface magnetism. A final conclusion can been drawn from STS measurements of well characterized films presented by Getzlaff *et al.* [153] where they found no residual spin polarization above the bulk Curie temperature despite the residual exchange splitting which they denoted to

short-range magnetic order, in agreement with our findings regarding the 5d6s bulk states.

Further, it was emphasized by Aspelmeier *et al.* that the experimental discrepancy concerning enhanced surface magnetism could very well stem from differences in the sample preparation since it influences the magnetism of thin films and their surfaces [144]. This could also explain the different reported magnetic couplings of the surface to the bulk which was claimed to be antiferromagnetic [160], ferromagnetic [167] and imperfect ferromagnetic [168]. The thickness of the film also plays a role as very thin films show finite size effects and are highly sensitive to induced strain from the lattice mismatch with the substrate. Thick films ($\sim 400\,\text{Å}$) show additional effects, such as, e.g. canted spin polarization at the surface [163, 169]. For films of the thickness used here, ferromagnetic coupling between surface and bulk is assumed to be present [153].

5.1.2 Analysis method and fitting algorithm

To analyze the size of the 5d6s exchange splitting well below the Curie temperature we need to be able to resolve minority and majority component of the valence band. The standard analysis which was also used in Ref. [42] are one-dimensional lineout fits to the *energy distribution cures* (EDC). We obtain them through integration of a small $k_{\parallel}$ region around the Γ point of the two-dimensional spectra. Figure 5.4 shows this for the example of a Gd spectrum measured at 90 K (highlighted in the inset).

For the analysis of the data obtained in pump-probe experiments we need to include the position of the 4f state to determine the Fermi energy. This way we can correct for pump pulse-induced space-charge effects as described in Ch. 4.2. The intrinsic linewidth of the states are Cauchy-Lorentz distributed with the width given by the photohole lifetime. For the fit of the Gd spectrum in Fig. 5.4 we use 5 different Lorentzians describing the sharp surface state (not shown), the minority (red) and majority (blue) component of the 5d6s valence band and the 4f state (gray) which is represented by two Lorenzians. In reality, the 4f state consists of a unresolvable multiplet of 7 components, all of them surface core level shifted. The fit by two Lorentzians is therefore only a crude approximation which is sufficient in our case since we are only interested in its energetic position to adjust the Fermi level accordingly (cf. Ch. 4.2).

Because we have no special spin-dependent selection rules the intensity of minority and majority valence band components are the same. The difference in the spectral width accounts for the distinct number of electrons available to the decay of the corresponding photohole. The intrinsic width of the surface state was found to be very narrow, only broadened during the *hot phase* of the electronic system (which lasts until about 2 ps pump-probe delay) as the hot electrons above the Fermi level decrease the lifetime of the surface state photohole. At negative time delays the width of the surface state reflects our energy resolution[5].

[5] High resolution measurements found an intrinsic width of 70 meV at 90 K [43, 170]

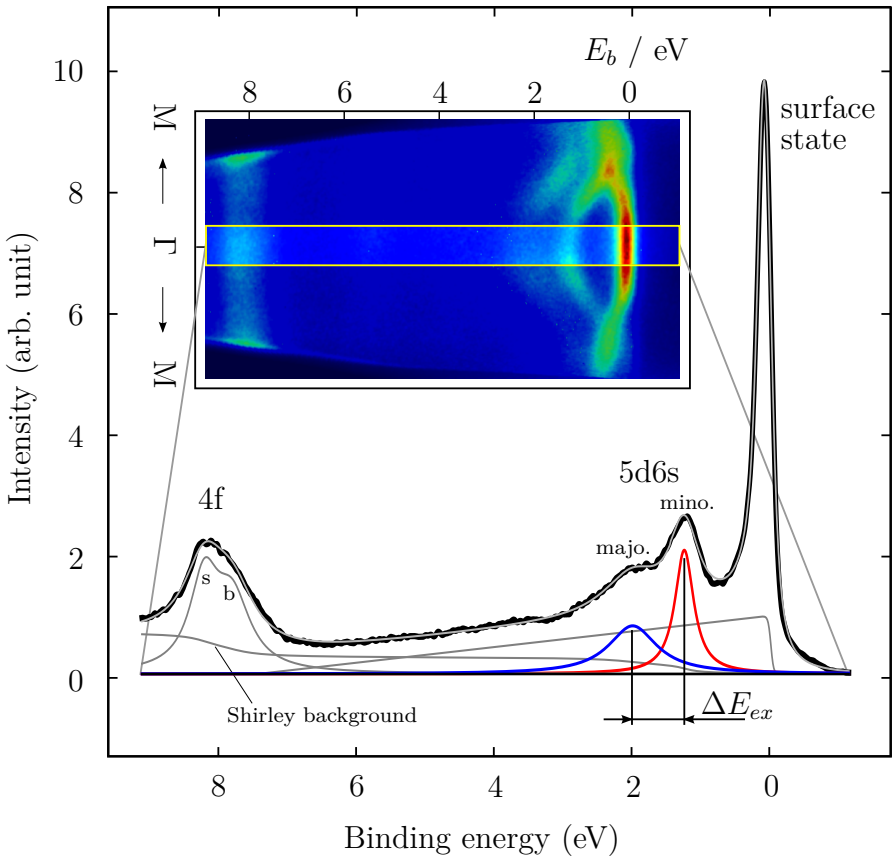

Figure 5.4: Photoelectron spectrum of a clean Gd(0001) film. *A selected energy distribution curve from the highlighted area ± 0.15 Å^{-1} around the Γ point was used to follow the evolution of the exchange split 5d6s bands. The combined spectral features of the fit give rise to the gray thin line that reflects the data (thick black line) reasonably well. The fitting model is described in detail in the text.*

All bulk states contribute to a Shirley background to account for the scattering probability of the electrons on their way to the surface. This background is proportional to the energy-integrated intensity of the peaks starting at the Fermi level whereas the 4f contribution was found to be 1.5 times bigger than the equal contributions from the minority and majority 5d6s bands. This is reasonable since these electrons have the additional probability to scatter with the valence electrons. In addition to this, a linear background has to be introduced to characterize the spectrum fully. It rises towards the Fermi level, and describes the contribution of phonon scattered electrons coming from other k-points, reflecting the rising DOS [42, 171].

Finally, to obtain the complete energy distribution curve all spectral features are cut by the Fermi edge and convolved with a Gaussian (σ = 60 meV, i.e. 140 eV FWHM) to account for the experimental resolution determined by the XUV monochromator and the analyzer (see Ch. 4.1.6 for details). For maximum objectivity and consistency all spectra in a pump-probe dataset were fitted using the same starting parameter and boundary conditions.

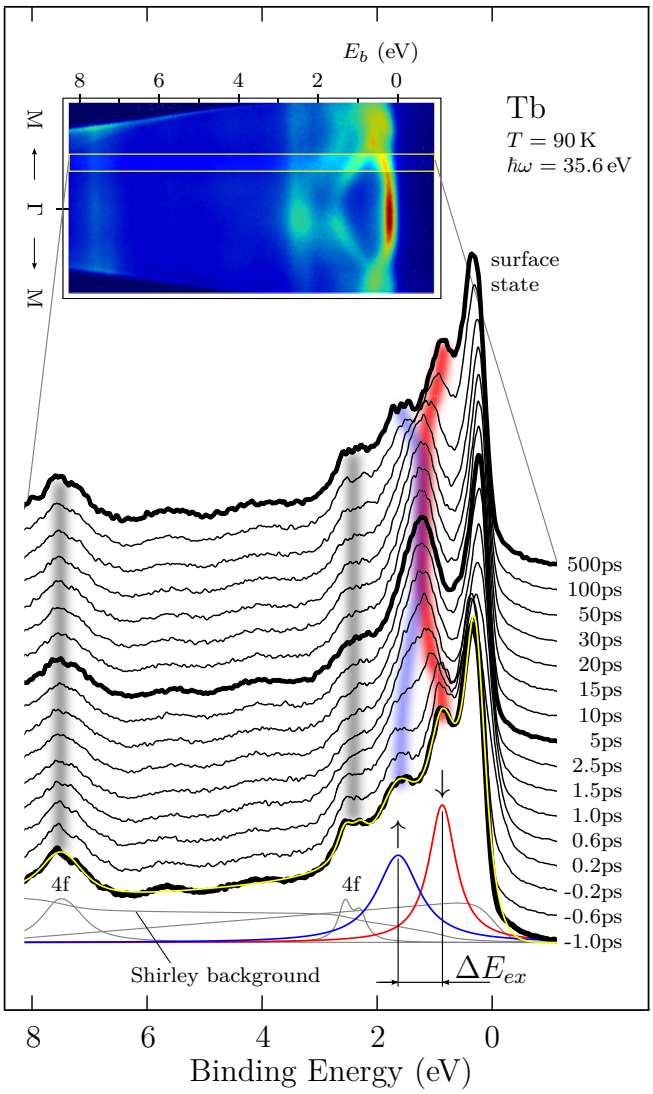

Figure 5.5: Photoelectron spectra of Tb(0001) for different pump- probe delays. *The selected energy distribution curves stem from the highlighted area at 0.3 - 0.4 Å^{-1} in Γ-M direction. This way it is possible to determine the size of the exchange splitting in the 5d6s bands (↑,↓). Thick lines correspond to -1, 5 and 500 ps. The fit result for -1 ps is shown at the front. Shaded areas follow the delay-dependent band positions and serve as guides to the eye.*

Analysis of Tb EDCs. In the case of Tb the exchange splitting can not be determined with a lineout fit at the Γ point because the 4f high spin $^8S_{7/2}$ multiplet component overlaps with the 5d6s majority valence band at this region (see inset in Fig. 5.5). It is therefore convenient to make use of the 5d6s band dispersion and analyze the spectra at 0.3 - 0.4 Å^{-1} along the Γ - M direction[6].

The fit procedure for the Tb spectra is analogous to that for Gd described above. Besides the known features that are also found in Gd the most notably difference is the mentioned 4f high spin multiplet component at 2.5 eV, which shows the same surface core level shift as the other components[7]. In contrast to Gd, the IR-induced space charge is negligible in Tb. The reason for this lies in the much higher work function of the Tb(0001) surface (4.95 eV compared to 3.72 eV [43, 44]). The Shirley background of the bulk states was found to be comparable to that for Gd with the same ratio of 1.5 between 4f and 5d6s contribution.

[6] This corresponds to approximately 8° emission angle at our photon energy.

[7] High resolution measurements of well prepared Tb films determined the surface core level shift to 0.26 eV [172]. We used this value in our analysis which reflects the data reasonably well.

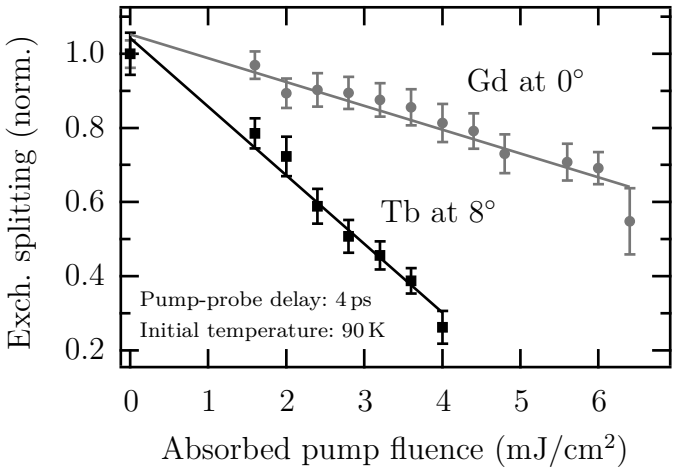

Figure 5.6: The maximum pump induced reduction of the 5d6s exchange splitting for different absorbed fluences. *The data was obtained at an emission angle of 0° for Gd and 8° for Tb to avoid interference by the Tb high spin 4f multiplet at the Γ point.*

We found the 5d6s exchange splitting in Tb to be three times more strongly reduced than in Gd at a given absorbed IR pump fluence (see Fig. 5.6) which can not solely be explained by the lower Curie temperature (223 K vs 293 K). The data in this figure was measured at 4 ps pump-probe delay where the valence band splitting reaches a minimum value (the dynamics will be discussed in Ch. 5.1.3). The fluence dependence is rather linear for both lanthanides at the measured values. For fluences above 2.5 mJ/cm^2, the exchange splitting in Tb is no longer directly resolvable. To quantify it further we need to set an additional boundary condition for the widths of both, majority and minority state. Because the intrinsic linewidth of the peaks is determined by the photohole lifetime, it decreases with decreasing binding energy. Assuming a linear dependence with a vanishing width at the Fermi level we get the following relation

$$\sigma = a(E_F - E_b) \qquad \text{with} \quad a = 0.27 \tag{5.2}$$

where the value of a is a global fit parameter determined from all spectra.

This model works well and gives an upper limit for the exchange splitting in the laser induced paramagnetic phase. It is also validated by using it for the Gd data where we found the same value for a and no difference compared to the analysis without bound widths.

Two-dimensional data analysis To compare the valence band dynamics of Gd and Tb at the Γ point it is necessary to fit the whole two-dimensional spectrum. The advantage is, besides the comparison at normal emission, an increase in statistics since we make use of all the measured data. The downside of this method are the higher computational effort and the requirement of additional assumptions such as the curvature of the band dispersion which have to be physically justified.

Fig. 5.7 shows a section of the fitted region including the surface state and the valence bands. Following the free electron picture these bands are assumed to be

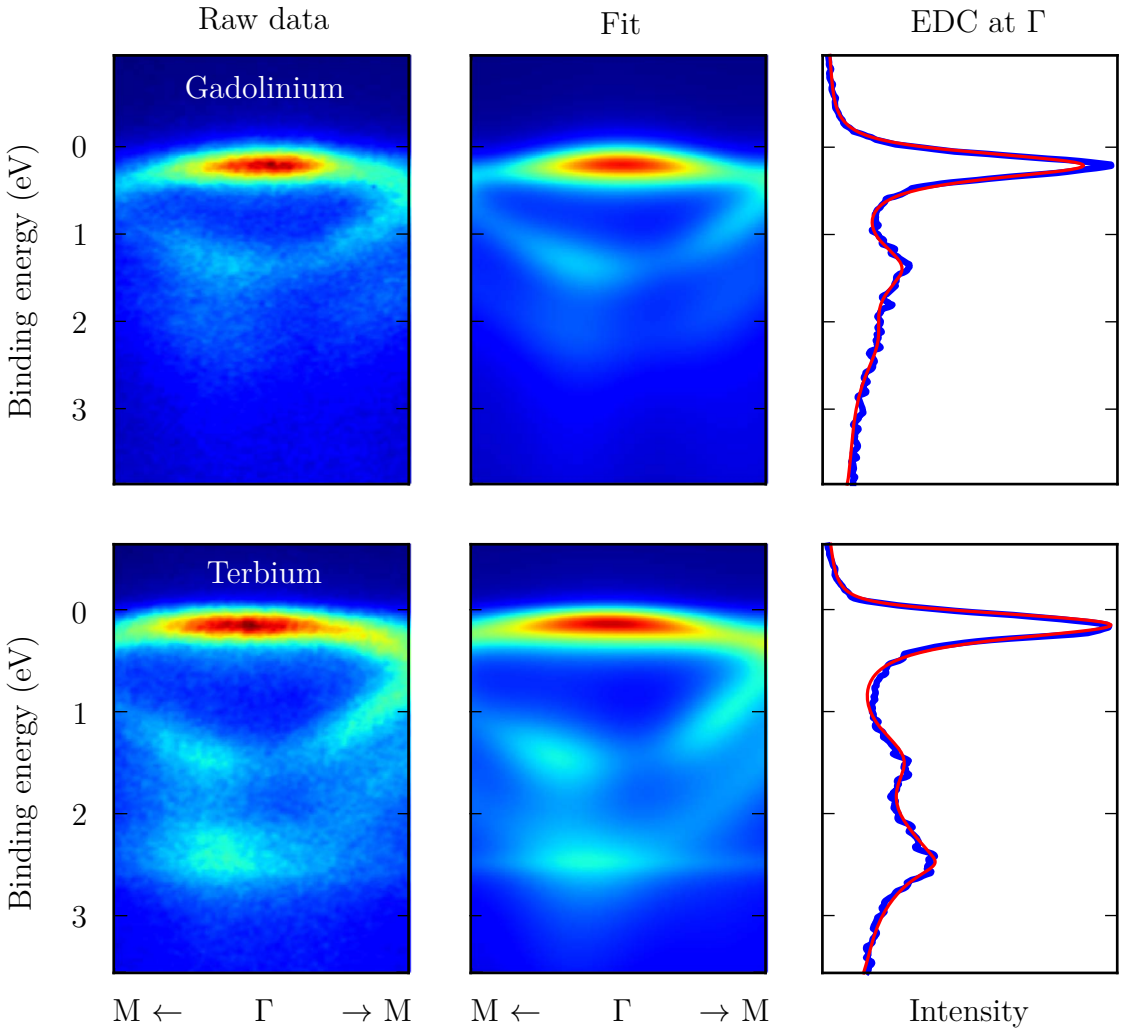

Figure 5.7: 2D analysis of a Gd and Tb spectrum at 90 K. *The raw data on the left is fitted assuming parabolic dispersions for all bands and non-dispersive 4f multiplets. The fit result is shown in the middle and reflects the data reasonably well. Energy distribution curves from the Γ point with the corresponding model lineout are shown on the right.*

parabolic at Γ with an effective mass describing the dispersion. This assumption reflects the raw data reasonably well. The obtained effective masses of the 5d6s bulk bands are about the one of a free electron, as a result of the itinerant character of these states. Included in the fit are also the measured 4f multiplet components which are non-dispersive (the ones at higher binding energy are not covered by the figure). Analogously to the one-dimensional fit model mentioned above an integral and a linear background are included and all bands are of Lorentzian line-shape in the energy direction. The intensity modulation along $k_{\parallel}$ seen in the data stems from the angular dependence of the dipole transition matrix element and is included by a cosine modulation. All spectral features are multiplied with a Fermi-Dirac distribution and convolved with a Gaussian in the energy and momentum direction reflecting the corresponding experimental resolutions.

5.1.3 Magnetization dynamics at 90 K

The data presented in this section were partially published and discussed in [II, V].

Using the two-dimensional fit procedure we follow the evolution of the minority and majority valence band component at Γ. The results shown in Fig. 5.8 exhibit an ultrafast response of the 5d6s valence band as the minority (red) and majority (blue) spin bands move towards each other and the exchange splitting diminishes. In both Gd and Tb the bands reach a quasi-stationary position at about 2 and 1 ps after excitation. The binding energies remain constant until about 40 ps pump-probe delay when the recooling of the sample sets in. It is noteworthy that during recooling the band positions are in line with the ones found in static temperature-dependent measurements (cf. Fig. 5.2). This is a strong indication that during this time the magnetic subsystems (i.e. minority 5d6s, majority 5d6s and 4f spins) are in equilibrium with the electron and phonon temperatures.

Within the first 1 - 2 ps after excitation the bands show a distinct behavior. This is especially pronounced in the case of Gd, where the 5d6s minority band (red) reacts much earlier than the corresponding majority counterpart (blue), which is delayed by about 0.5 ps. Additionally the time constant of the minority band shift is, with ≤ 0.3 ps, not resolvable[8] and much faster than the majority shift with 0.9 ± 0.2 ps. Compared to these findings the dynamics in Tb are more equal. Both bands start to move simultaneously at t_0 and a smaller difference in the fitted time constants is found ($\tau_{\mathrm{mino}} \leq 0.3$ ps and $\tau_{\mathrm{majo}} = 0.5 \pm 0.1$ ps)[9].

Another notable feature is the size of the minority shift in relation to its majority counterpart. In Gd the shift of both bands are quite different and mainly dominated by the majority band. This behavior is also seen in static measurements (cf. Fig. 5.2). Within a simple Stoner model one would expect equal shifts though. Recent theoretical work attributed this asymmetry to a surface induced effect which is introduced in the measurement by surface projection of the bulk states [150]. However, in Tb the shift of both spin bands is of comparable size and the effect is therefore most likely a result of the different density of minority and majority states at the Gd Fermi surface [24].

The band dynamics discussed above result in a breakdown of the exchange splitting which is shown in Fig. 5.9. We see directly that Tb reacts much faster than Gd. The difference can be quantified by single exponential fits (dashed lines) which yield a decay constant of $\tau_{\mathrm{ex}} = 0.5 \pm 0.1$ ps for Tb and $\tau_{\mathrm{ex}} = 1.0 \pm 0.2$ ps for Gd. The Gd time constant is in line with MOKE measurements, which found a value of 0.85 ps for the same system, but with a considerably lower absorbed fluence of about 1 mJ/cm^2 [173]. The electron temperatures shown in the inset of Fig. 5.9 reflect the different absorbed fluences ($F_{abs}^{Gd} = 5.5$ mJ/cm^2 and $F_{abs}^{Tb} = 3.6$ mJ/cm^2) and was used to determine the exact position of t_0. Thereby one has to keep in mind

[8] The shortest resolvable timescale in this experiment is limited by the pump-pulse length which we stretched to 300 fs FWHM to reduce space charge (cf. Ch. 4.2 for details). The effective time resolution for timescales slower than that is determined by the jitter between pump and probe which is at $\Delta t < 50$ fs much better.

[9] For better comparison the Tb sample was also measured with a stretched pump pulse, therefore we are also limited by the 0.3 ps.

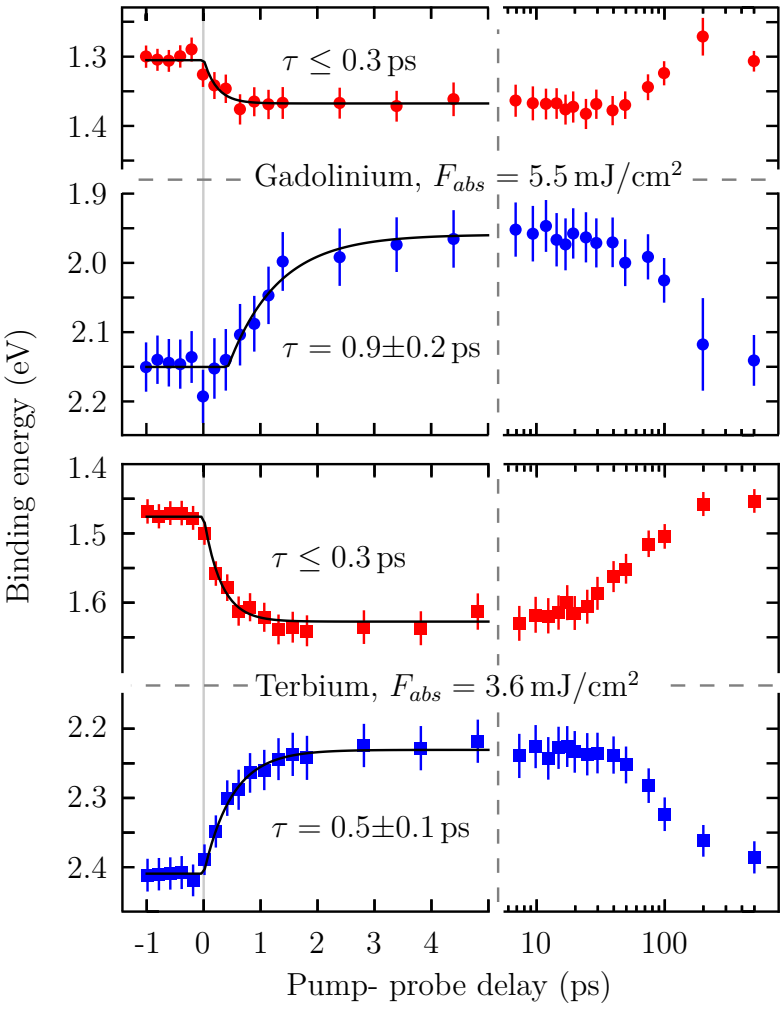

Figure 5.8: Binding energies of the minority (red) and majority (blue) spin bands at Γ as a function of pump-probe delay. *Solid lines are exponential fits to obtain the time constant τ. The error bars show two standard deviations from the fit. Note that the time axis changes from linear to logarithmic at 5 ps delay, with the last data point at 500 ps.*

that the absolute temperature obtained this way is biased due to (time-dependent) space-charge broadening (see Ch. 4.2 for details). This is especially true for Gd because of its low work function ($\Phi_{\mathrm{Gd}(0001)} = 3.72\,\mathrm{eV}$ [43], $\Phi_{\mathrm{Tb}(0001)} = 4.95\,\mathrm{eV}$ [44]). Nevertheless the rise in electron temperature is remarkably close to theoretically expected values (see e.g. Ref. [137]).

Since there is, at present, no theory that can describe a distinct response of the valence band components we use the M3TM, which was introduced in Ch. 2.2.1, to follow the "overall magnetization" of the valence band system via the exchange splitting. This way we can test if the dynamics can be explained using only Elliott-Yafet like electron-phonon spin-flip scattering. With knowledge of the electron and the spin temperature (i.e. the width of the Fermi edge and the exchange splitting), we can use known material constants together with the parameters given by Koopmans *et al.* [14]. First we rewrite equation 2.36 (Weiss mean field

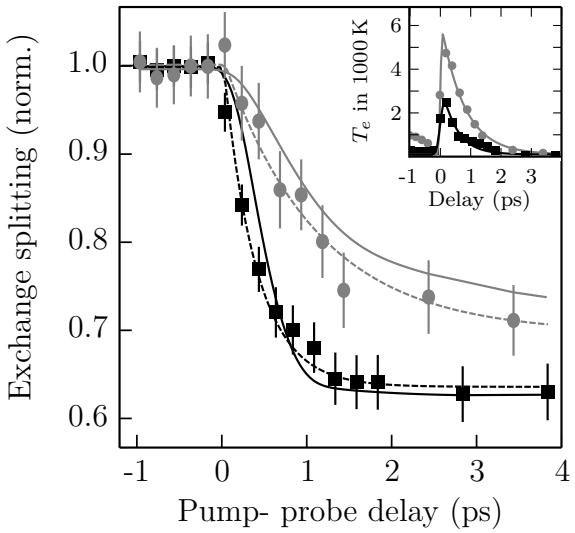

Figure 5.9: Temporal evolution of the exchange splitting of Gd (•) and Tb (■). *Dashed lines are single exponential fits that yield time constants of $\tau_{Gd} = 1.0 \pm 0.2$ ps and $\tau_{Tb} = 0.4 \pm 0.1$ ps. Solid lines correspond to a fit with the M3TM [14]. The inset shows the electron temperature obtained by the Fermi function in our 2D-analysis.*

description) by substituting $m = \Delta E_{ex}/2k_B T_C$ and $R = 1/\tau_R$

$$\partial_t \Delta E_{ex} = \frac{\Delta E_{ex}}{\tau_R} \frac{T_p}{T_C} \left(1 - \frac{\Delta E_{ex}}{2k_B T_C} \coth \frac{\Delta E_{ex}}{2k_B T_e} \right) \tag{5.3}$$

We can now follow the measured dynamics within the M3TM with τ_R as a free paramenter. The result is shown in Fig. 5.9 as solid lines. The obtained values of τ_R are 9 ps for Tb and 208 ps for Gd. From Eq. 2.37 we know that

$$\tau_R \sim \frac{\mu}{a_{sf} T_C^2} \tag{5.4}$$

The electron-phonon coupling g_{ep} is the same for Gd and Tb and thus not included here. This assumption is valid since in the M3TM super-diffusive spin transport is neglected and g_{ep} is therefore completely defied by the electron temperature profile obtained from the width of the Fermi edge. As shown in the inset of Fig. 5.9 the electron-phonon scattering rate is of the same shape and single exponential fits to the decay of T_e yield 0.9 ps for both materials. Since Gd and Tb have a similar valence band structure at the Fermi level we can assume the same spin flip probability a_{sf} for the hot electrons. The model then predicts a response which is twice as fast in Gd than in Tb. This is in contrast to the fitted values of τ_R which, if we trust the model, would imply a much higher value for a_{sf} in Tb. The reason for this discrepancy may be explained by the high angular orbital momentum in the Tb 4f system which is caused by the additional electron. It leads to strong spin lattice coupling[10] in the 4f system [175]. The M3TM however does not distinguish

[10] This is also reflected in the distinct magnetocrystalline anisotropy which is strong (~ 11 meV [41]) in Tb and nearly absent (~ 0.03 meV [40]) in Gd. Evidence for such a strong coupling can also be found in the magnon dispersion relation of Tb which exhibits several phonon induced features which are missing in Gd [67, 174].

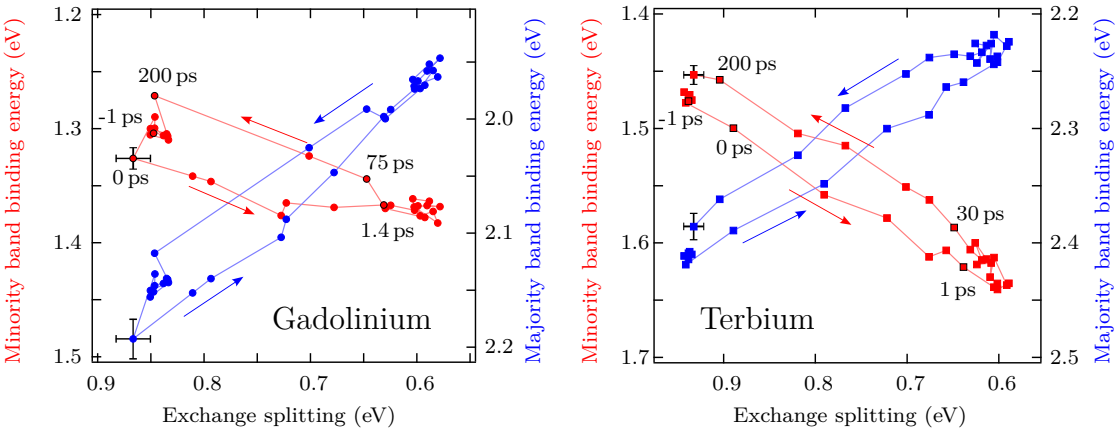

Figure 5.10: Laser driven minority (red) and majority (blue) valence band shifts and thermal recovery as a function of the exchange splitting. *Some delay points are labeled for the minority state. Starting at the left hand side of the plot at maximum exchange splitting, the band positions follow the lower branch as the exchange splitting diminishes after laser excitation. The bands reach a quasi-stationary position after about 1.5 ps in Gd and 1 ps in Tb. During thermal recooling of the sample the states follow the upper branch from right to left. The bands reach their initial positions after about 500 ps. Error bars show one standard deviation for a selected data point.*

between magnetism from different orbitals and is therefore limited to systems with one defined magnetic temperature.

A closer look to the fit results in Fig. 5.9 reveals that within the M3TM it is not possible to obtain the immediate decrease of the exchange splitting as shown by the single exponential fits. This is a principal limitation of the M3TM because the exchange splitting couples not solely to the electron but also to the phonon temperature in the equation above. The phonon contribution can in principle be compensated by τ_R but it is then not possible to reproduce the exponential shape. Particularly the very fast response of the minority spin band can not be explained by Elliott-Yafet like spin-flip scattering and has to have at least partially a different origin.

To further investigate the different temporal behavior of the magnetic subsystems, i.e. minority and majority valence band, we follow their binding energies with respect to the observed exchange splitting as shown in Fig. 5.10. Let us discuss the dynamics on the example of the minority state (red) in the gadolinium panel. We start at -1 ps with an initial exchange splitting of about 0.85 eV. At t_0 the laser driven demagnetization starts and the band position follows the lower branch until the exchange splitting reaches a quasi-stationary value of about 0.6 eV when both bands keep their binding energies until about 40 ps. After this time the recooling sets in and the bands follow the upper branch which corresponds to the positions that were reported in statical measurements [42]. Since the band positions are not the same during de- and re-magnetization we know that the demagnetization is not thermal, i.e. that the magnetic subsystems are not in equilibrium. The same argument can be made for Tb (right panel), where the valence band system is not

as far out of equilibrium as in Gd. The time that it takes for the 5d6s spin system to internally equilibrate is about 2 ps for Gd and 1 ps for Tb.

In order to explain the experimental findings for the highly perturbed 5d6s bands let us take a closer look at the ultrafast dynamics. Fig. 5.11 captures the fast timescale of the Gd valence band system for an absorbed fluence of 4.5 mJ/cm^2. The dataset was measured with smaller time steps and better statistics than the one discussed above. In addition to the 5d6s bulk band dynamics, the $5d_{z^2}$ surface state is included in the upper part of the plot. Besides its shift we also map its intensity. To discuss the dynamics of the bands and the underlying processes it is useful to follow simultaneously the evolution of the electron temperature. It is included in the bottom panel together with E3TM simulations to obtain the lattice temperature (T_p). It should be noted that the measured temperatures have an offset due to space-charge broadening of the Fermi edge. Nevertheless the relative change in the electron temperature is sufficient for a qualitative analysis of the dynamics. The timescales mentioned in the following discussion were obtained by single exponential fits to the band positions (solid lines).

We start with the IR laser excitation indicated by the vertical gray stripe at t_0 (300 fs FWHM). During this excitation phase we excite electrons to energies up to 1.6 eV above the Fermi level. Such transitions are available for all the observed spin bands (cf. calculation shown in Fig. 1.1 c [24]). Within 50 - 100 fs the excited electrons thermalize via electron-electron scattering [68, 176] leading to an electronic temperature of a few thousand Kelvins as shown in the bottom panel. Spin- and time-resolved measurements find that these hot electrons are not spin polarized [149] as a result of (spin conserving) ultrafast exchange scattering, which favors final state photohole pairs of opposite spins [177]. During the excitation several things happen. As the electron temperature rises, the surface state shifts upwards, to lower binding energies, and its intensity is reduced, reflecting the excitation density of the d_{z^2} electrons [178]. Because we do not measure the complete Brillouin zone we can not give an absolute value for the depopulation of the surface state. Nevertheless the intensity variation at the $\overline{\Gamma}$ point gives an idea about the amount of excited surface state electrons. We observe a remarkably strong drop to a value of 57 % during the IR excitation. Within this fast timescale the minority valence band shifts to higher binding energies. This, together with the reduced surface state intensity, indicates an effective charge redistribution[11] from surface to the bulk states as will be explained in the following.

At the starting temperature of 90 K the minority valence band is only partially occupied, crossing the Fermi edge near the K point of the Brillouin zone and in between Γ - K [24, 29, 179] and its spin polarization is approximately 80 % [155], which means that decay of majority electrons into this state is not completely forbidden. In fact, it was pointed out that excited majority electrons have an enhanced probability to decay into a minority channel by emission of a magnon [177, 180]. This process is overall spin conserving and does not lead to a net demagnetization. As a result, the minority band spin polarization should be

[11] This process should not be confused with super-diffusive spin-transport [17], which could additionally play a role here.

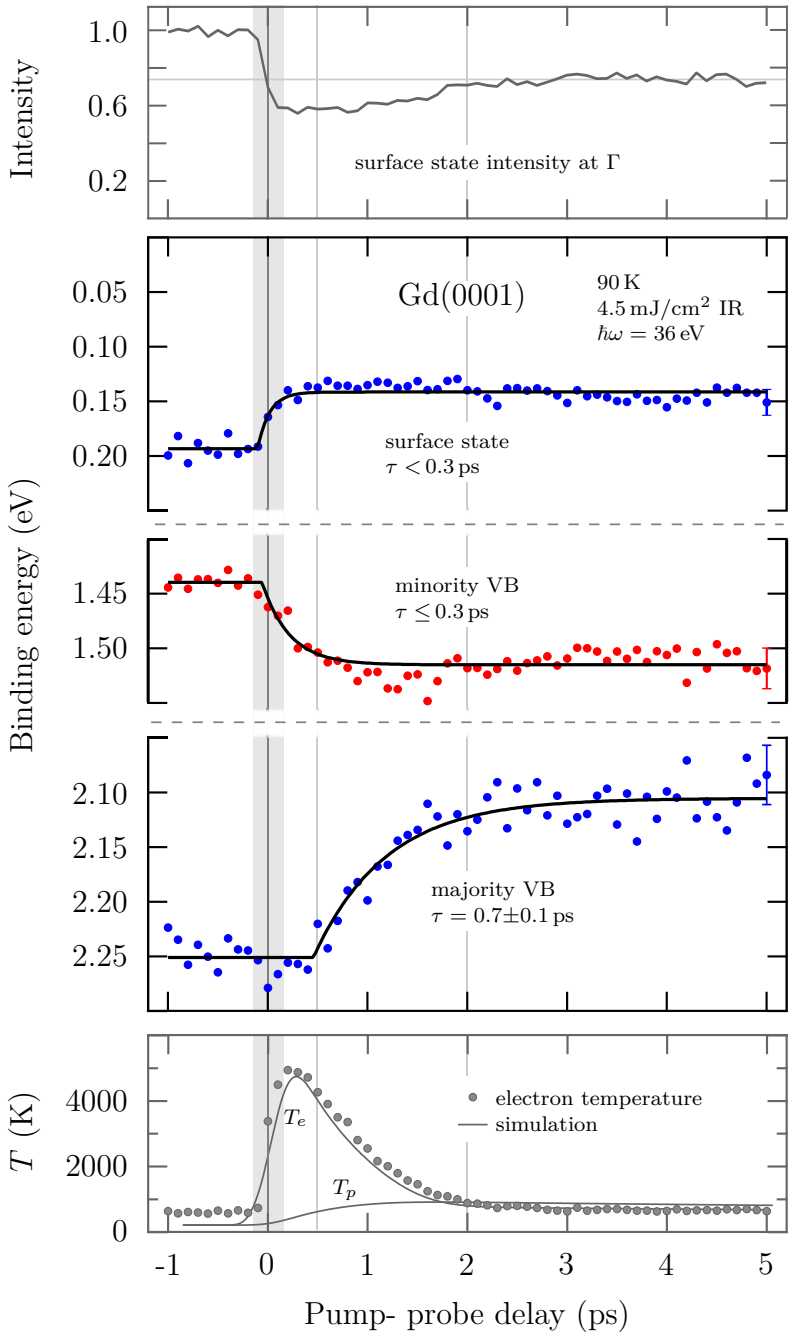

Figure 5.11: Ultrafast response of the Gd(0001) valence band structure at Γ. *The middle panel shows the binding energies of the majority surface state together with the minority and majority valence bands as a function of pump-probe delay. Solid lines are single exponential fits to obtain the corresponding time constants τ. The gray vertical stripe at t_0 illustrates the temporal width of the IR excitation (300 fs FWHM). Vertical gray lines at 0.5 and 2 ps facilitate the comparison of the dynamics. In the top panel the changing surface state intensity is included; the bottom panel shows the temperature of the electron gas as obtained by the width of the Fermi edge together with E3TM simulations.*

reduced as its binding energy reduces if the proposed magnon-decay of the hot majority electrons is the driving factor. Although additional effects including the lattice, like Elliot-Yafet spin-flip scattering, will certainly lead to a decreased lifetime of the hot majority electrons and therefore further enhance the population of the minority spin band, these additional contributions should be negligible during the first 100 fs and the ultrafast minority band shift around t_0 will predominantly be caused by spin-preserving electron-magnon scattering. To verify this thesis, it would be most insightful to perform spin- and time-resolved measurements on the valence band system, since EY-scattering should not lead to a significant reduction of the minority spin polarization, because it increases the number of minority electrons. The majority band on the other hand can not participate to charge redistribution, because it is already fully occupied[12]. Even though electron-magnon scattering would not imply a change in the overall magnetization during the ultrafast timescale, the minority shift has an impact on the subsequent evolution of the magnetic system because the spin-dependent Boltzmann scattering integral changes with the size of the exchange splitting [181, 182]. This implies that also electronic and thermal effects, which influence the splitting[13] can enhance (or lower) the spin-flip probability and therefore influence the demagnetization time.

After this initial, purely electronic, response electron-phonon scattering takes over as hot electrons equilibrate with the cold lattice. This process is with a timescale of 0.7 ps a lot slower than the electron-electron and electron-magnon interactions discussed above[14]. The surface state population recovers roughly on this timescale to a quasi-final value of 72 %, which persist (much like the shift) until the recooling of the sample starts at 40 ps (not shown here) and is therefore not related to spin transport. With a delay of about 0.5 ps with respect to the laser excitation, the majority valence band starts to move to lower binding energies. At that time, the minority component has already reached its quasi-final energy. Besides the half picosecond delay, the majority band is also much slower than the minority shift (0.7 vs. 0.3 ps). By comparison with the evolution of the electron temperature, we find that the majority band acts on the timescale of electron-phonon scattering, while the minority component is mostly related to faster processes like electron-electron and electron-magnon scattering. A change in the majority band binding energy can thus only be caused by spin-flip processes or thermal lattice expansion. It should be noted that the majority band movement could be adequately described by the somewhat slower electron-phonon scattering of the Elliott-Yafet type, since it follows the decay of the electron temperature.

[12]The initial photohole excitations in this band can decay within the first 100 fs through electron-electron scattering. But there are other majority bulk bands that cross the Fermi level which can contribute to the redistribution [179].

[13]The size of the exchange splitting in the 5d6s bands is determined by the inter-atomic 5d-5d (J_{ij}) as well as the intra-atomic 4f-5d (J_{int}) exchange parameters. The inter-atomic exchange constant between electrons from lattice cites i and j depends thereby on the inter-atomic distance and therefore on the phonon temperature T_p [183].

[14]The fastest timescale for electron-phonon interaction is given by the highest possible phonon energy which translates to 300 fs in Gd [184]. However the slow decrease of the electronic temperature indicates that this channel is not very efficient. Still an impact on the magnetic properties of the surface, due to laser induced strain, can not be completely excluded because the magnetostriction along the c-axis is not negligible in Gd [33, 185].

In conclusion we have found that the initial decrease in the Gd 5d6s exchange splitting, which is caused by the minority dynamics, is not necessarily accompanied by a reduction of the overall magnetization, but can be explained as the result of charge transfer between different states (i.e. surface and bulk) accompanied by magnon excitation in the minority band. The response of the majority valence band on the other hand is most likely caused by EY-like spin-flip scattering and should therefore lead to a reduction of the sample magnetization. A summary of the interpretation given here is shown in Fig. 5.12.

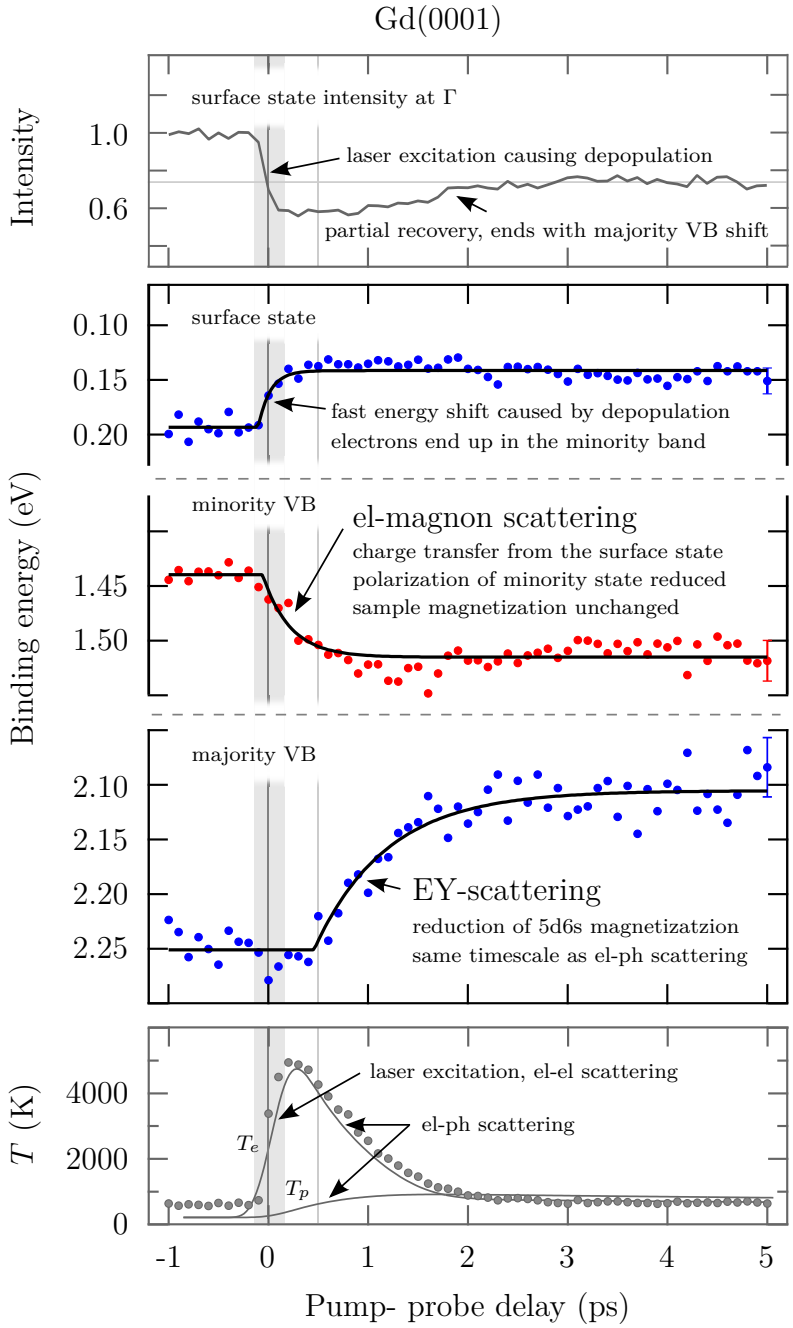

Figure 5.12: Interpretation of the Gd(0001) valence band response to fs laser excitation. *Shown is the data form Fig. 5.11 with a summary of the physical effects which we used to explain the measured dynamics. The full interpretation is given in the text.*

5.2 Gd: dynamics at different temperatures

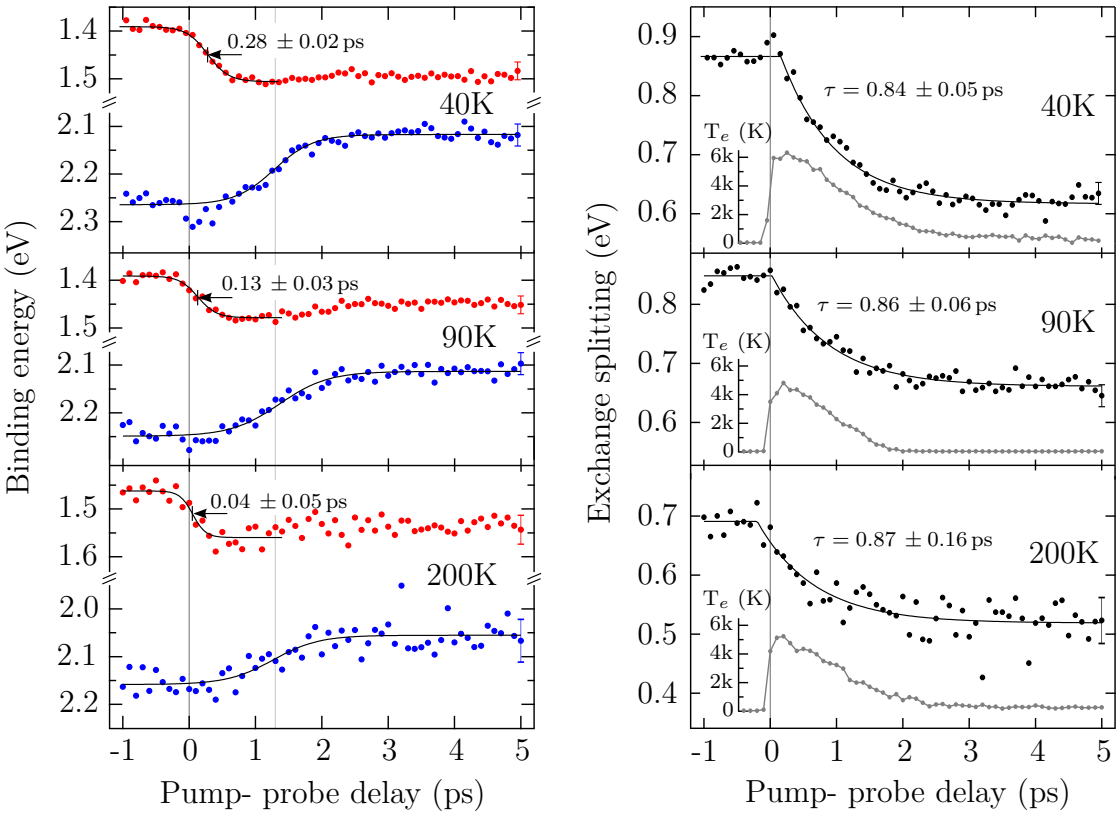

Figure 5.13: Ultrafast demagnetization of Gd at different starting temperatures. *The experiment was conducted with photon energies of 36 eV for the 100 fs probe and 1.6 eV for the 300 fs pump pulse with an absorbed pump fluence of 4 - 5 mJ/cm^2.* ***Left:*** *binding energies of the minority (red) and majority (blue) valence band components at Γ as a function of pump-probe delay.* ***Right:*** *the corresponding evolution of the exchange splitting. The fitted time constant of the collapse is roughly the same for all three temperatures. Temporal overlap of the pump and probe pulse (i.e. absolute t_0) was verified by the jump in the electron temperature (gray). Error bars are, for the sake of clarity, only included for the last data point and show two standard deviations.*

The explanation for the distinct dynamics given above suggests a dependence on the initial sample temperature. When the ultrafast minority band shift depends on the availability of this state as a decay channel, then it should be faster for higher starting temperatures because its spin polarization is lower and therefore less restricted for the decay of hot electrons. Fig. 5.13 shows the dynamics for three different starting temperatures. The response of the surface state is the same for all temperatures and is, for the sake of clarity, not included in the figure. If we consider the left panel with the binding energies of the bands we find the expected response of the minority band. At low temperatures (40 K), where the polarization of the exchange split bands are close to 100 %, the dynamics is delayed by 0.28 ps. In contrast, at 200 K where the spin polarization is only about 50 % [155], the minority band reacts on the timescale of the pump pulse. Since this delay is very

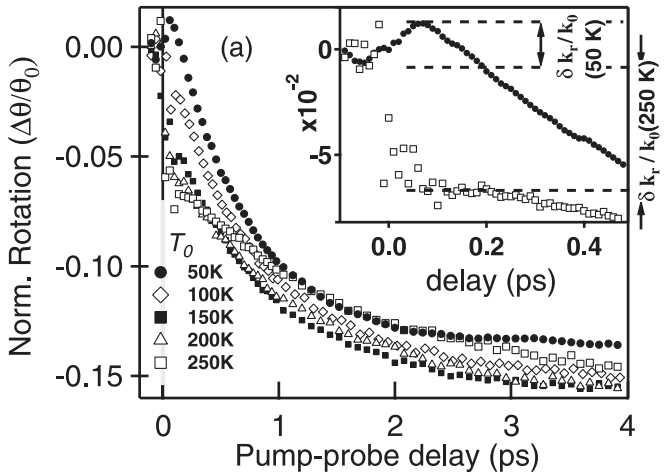

Figure 5.14: MOKE rotation from Gd(0001) as a function of pump-probe delay for different starting temperatures; from Ref. [173]. *The inset shows the ultrafast dynamics for equilibrium temperatures of 50 and 250 K. At 50 K there is an enhancement in the MOKE rotation (inset) which persists for about 150 fs until the decrease of the MOKE signal with a timescale of 0.8 ps. If started at an equilibrium temperature of 250 K an instantaneous initial decrease of MOKE rotation can be observed followed by a further reduction with a time constant of 1.2 ps.*

minor, it would be helpful to measure it again with shorter pulses. For this, one needs to use longer pump wavelengths to avoid space charge. Contrary to the minority dynamics, the starting point of the majority shift seems to be independent of the temperature, although small variations can not entirely be excluded.

The exchange splitting in the right panel reflects the temperature depended delay of the minority band as the starting point for the demagnetization is shifted accordingly. The absolute position of t_0 (i.e. the pump-probe overlap) is well known, since it can be validated by the electron temperature obtained from the Fermi edge, as shown in the gray insets. Although the exchange splitting is the result of the two distinct dynamics (minority and majority band movement) its dynamic can be reproduced with a single exponential fit. Besides the delay in the starting time, the demagnetization dynamics is the same for all three temperatures and exhibits a time constant of 0.85 ± 0.05 ps.

If we now compare our results with measurements from Sultan *et al.* [173], who used magneto-optical Kerr effect (MOKE) to follow the temperature-dependent dynamics, we find some distinct features. Fig. 5.14 shows the Kerr rotation as a function of pump-probe delay for an absorbed pump fluence of $1\,\mathrm{mJ/cm^2}$ (1.55 eV, 35 fs). Within the first few hundred femtoseconds the temperature plays a crucial role in the observed dynamics. At low temperatures (50 K) the MOKE rotation is enhanced within the first 150 fs but instantaneously reduced at 250 K (see inset). This is remarkable because we can now explain this behavior in terms of valence band dynamics. Comparing the extreme cases of "cold" and "warm" demagnetization as shown in Fig. 5.15, we find qualitatively the same features as in MOKE. The enhanced magnetization at low temperatures originates from a

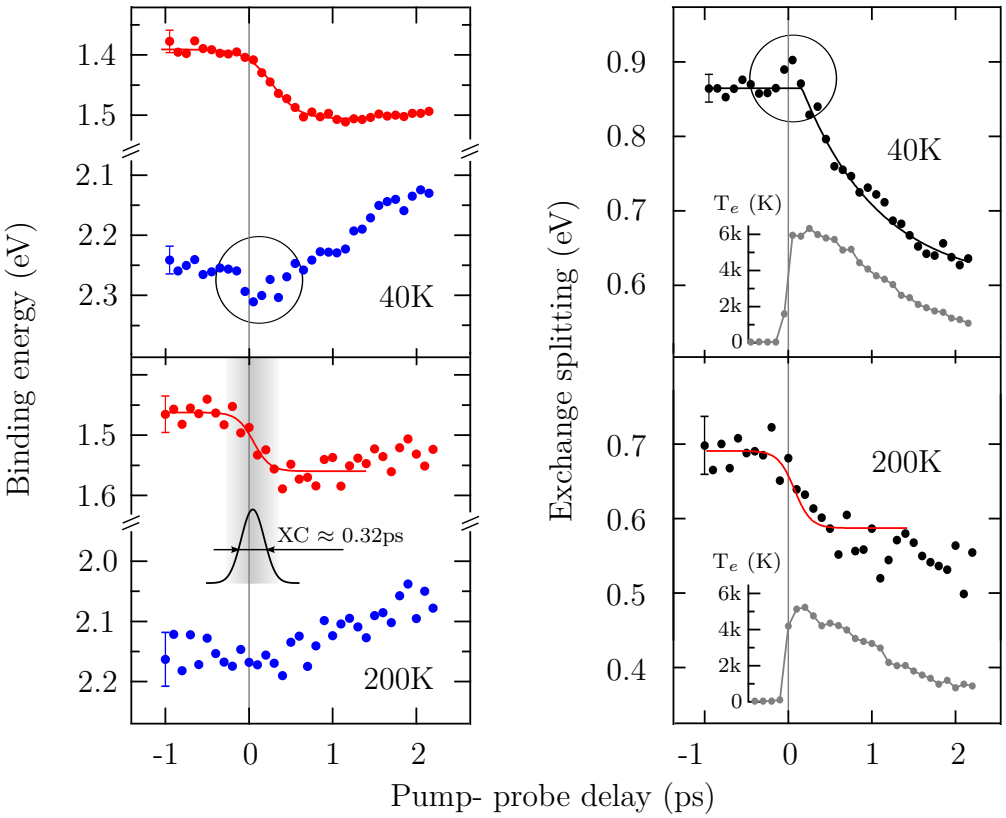

Figure 5.15: Ultrafast demagnetization of Gd at 40 and 200 K. *Shown is selected data from Fig. 5.13. The dynamics reflects the behavior found in MOKE rotation measurements. The enhancement of magnetization in cold (40 K) samples just after t_0 (circle) is caused by the majority spin band dynamics, while the ultrafast decrease of the exchange-splitting at the higher starting temperature (200 K) is determined by the minority spin band dynamics, as indicated by the overlaid red sigmoid fit from the minority dynamic (bottom left). The gray stripe indicates the pump-probe cross-correlation (XC) of 0.32 ps.*

dip at t_0 in the majority band together with the delayed response of the minority part. This majority dip, which is most pronounced at low temperatures, could be caused by a coherent interaction of the photon field with the itinerant electrons [7]. At high temperatures the t_0-dip in the majority state is absent and the step-like initial demagnetization is solely caused by the minority response, which basically reflects the width of the pump pulse.

5.3 Gd: dynamics at different pump fluences

Besides the equilibration temperature, another parameter that influences the dynamics is the fluence of the pump pulse. To compare different measurements it is therefore crucial to determine the absorbed fluence in the probed region. It should be noted that obtaining an absolute value is not simple, as it depends strongly on the spatial overlap of pump and probe pulse. In our measurements, this overlap is

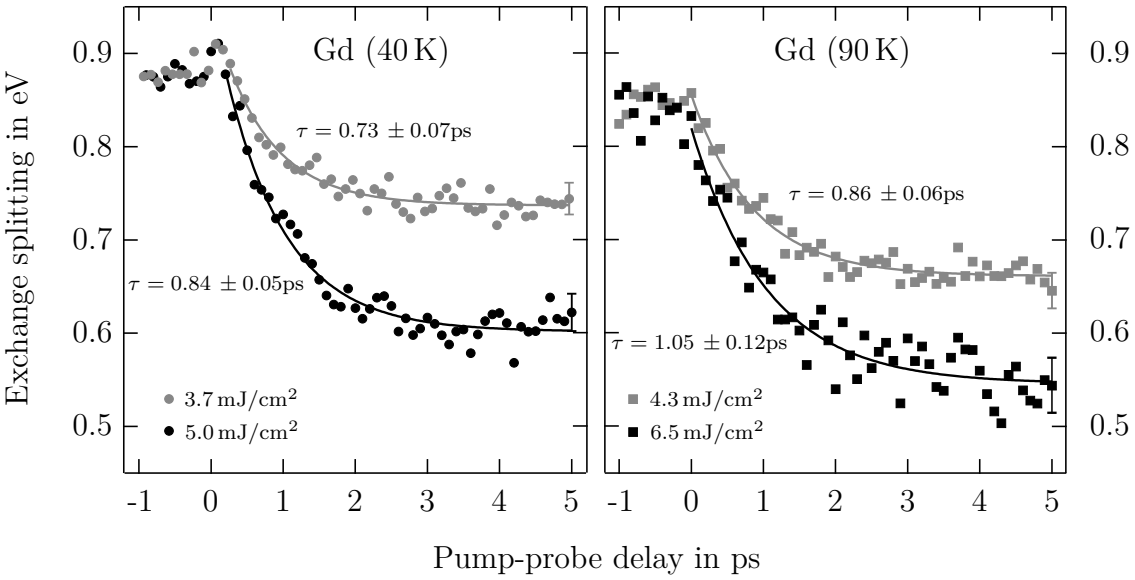

Figure 5.16: Impact of the pump fluence on the 5d6s demagnetization. *The reduction of the exchange splitting at a staring temperature of 40 K (left) and 90 K (right) is shown for two different absorbed fluences. In general lower fluences result in a less pronounced demagnetization with a faster time constant. Error bars at the last data point show two standard deviations.*

determined with a high magnification camera on a separate sample coated with a fluorescence indicator[15]. To find the exact position for both pump and probe, the pump pulse has to be strongly weakened. Thereby we have to make sure that the beam position is not moved by the attenuator. In addition, beam stability in the high harmonic path has to be assured as well. The spatial stability during a measurement was ensured by checking the beam positions before and after the experiment with the above method. The downside of this simple approach is that the beam spot on the fluorescent sample has a different color for the XUV and the IR beam, which results in strong chromatic aberration effects in the magnifying optics of the camera. This makes it imperative to adjust the focus of the camera for each spot accordingly to determine the size of it as well as its position.

The pump spot of the measurements presented here is set to be on the order of $\varnothing = 0.5\,\mathrm{mm}$ (FWHM) with a Gaussian intensity profile. We now probe the sample in the center of the pump spot with a 130 µm diameter (FWHM) XUV beam. To determine the absorbed IR fluence we measure the reflected beam profile at the angle of incidence (60°). Taking into account the windows of the vacuum chamber we find an absorption of 18 % for 100 Å Gd(0001)/W(110), which is in accordance to values given by Lisowski [186]. To obtain an absolute value for the fluence we fit a two-dimensional Gaussian to the pump spot intensity. 68 % of the applied fluence are now found within a $2\,\sigma$ circle. To account for finite spot sizes and inaccuracies of the spatial overlap we averaged the intensity within the $2\,\sigma$ circle for the fluence. From this, one sees directly that the absolute value for the excitation density has

[15] We used fluorescence indicator F254 for this, which is a manganese-doped zinc silicate Zn_2SiO_4, (CAS: 68611-47-2).

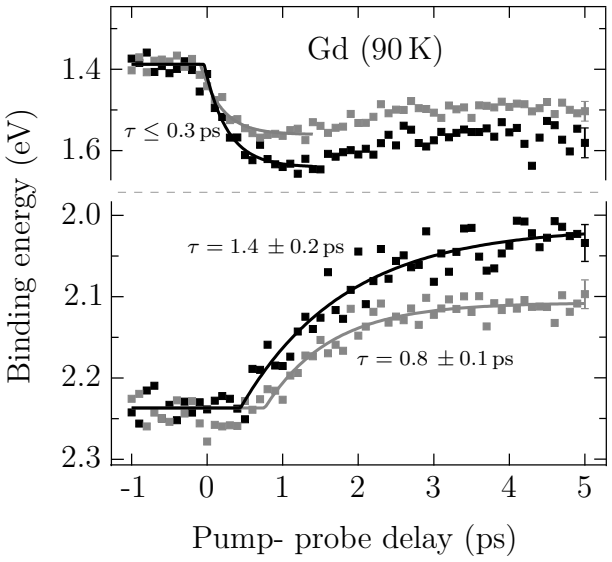

Figure 5.17: Distinct band dynamics for two different fluences at an equilibrium temperature of 90 K. *The minority band (top) shows very similar dynamics for the different absorbed fluences of 4.3 mJ/cm² (■) and 6.5 mJ/cm² (■). In contrast, the majority dynamics (bottom) shows significantly different time scales. The given time constants are obtained by single exponential fits (solid lines).*

a large error that we estimate to be on the order of ± 30 %. However, the relative error between two successive measurements depends only on the pointing stability and is therefore significantly smaller at ± 10 %.

Fig. 5.16 shows the reduction of the exchange splitting for two different fluences at 40 K and at 90 K. As one would expect, a higher fluence results in stronger demagnetization with an increased time constant, as obtained by single exponential fits. Besides this, it seems that lower starting temperatures reduce the time constant of the exchange splitting dynamics, which we can explain due to the delayed minority response. This results in a more "synchronous" shift of the bands and thus a faster decay. This reduction of the time constant was also found by MOKE [173], indicating that MOKE measures the combined response of both valence bands.

To find the origin of the fluence dependence we have a closer look at the band dynamics leading to the different exchange splittings. Fig. 5.17 shows this for the two fluences at 90 K. The minority shift seems to be simply enhanced for a higher fluence. Since its time constant ($\tau_{mino} \leq 0.3$ ps) reflects the pump-pulse length, there could be a fluence dependence as well[16]. The majority band on the other hand exhibits a significantly slower time constant at the higher pump fluence. This fluence dependence of the dynamics is well known [188, 189] and can be adequately described by EY-scattering [14]. The slight mismatch between both majority starting times is within the error bars.

It should be noted that the fluence dependence of the dynamics could in principle be influenced by electronic heat transport from the tungsten substrate. Gd and W have about the same IR absorption lengths of about 25 nm [186] but considerably different heat capacities. The static heat capacity of Gd is about twice that of W at the relevant temperatures (90 - 300 K) [71, 74]. This could result in a large temperature gradient at the Gd/W interface, where, at our geometry, the IR intensity is still about 60 % compared to the first layer [186]. Hot electrons from

[16] There is evidence that exchange scattering can lead to a fluence dependence, caused by the longitudinal relaxation within the sample [187].

the tungsten substrate can thus lead to a considerable heat transport into the Gd film after excitation. This contribution should depend on the absorbed fluence, since the temperature gradient at the interface does. A typical value for a 100 Å thin metal film to become uniform in temperature is about 2 ps [190] which is close to the observed timescale. However, this argument holds only true, if we assume ultrafast coupling of the valence band polarization to the 4f spin system since it is responsible for the high magnetic heat capacity. By neglecting the 4f spin contribution, the heat capacities of Gd and W are of the same size and we would therefore expect no influence from the substrate at fast timescales. This is important, because we will see later that the 4f spin polarization does not change on ultrafast timescales, we can thus neglect the substrate within the first few picoseconds.

Chapter 6

Localized electrons: MLD from the 4f multiplet

6.1 Orbital-resolved magnetization dynamics

Up to now we have mainly discussed the magnetization dynamics of the 5d6s spins and disregarded the 4f system. Since the 4f electrons carry the main part of the overall magnetic moment it is reasonable to follow its dynamic directly. To this end we use magnetic linear dichroism in photoemission, which is known to measure ferromagnetic order if a chiral geometry is chosen (see Ch. 3.3 for details). Besides static measurements, for which MLD is a well established probe for magnetic order [62, 97, 105, 106], MLD was also used to follow magnetism in the time domain [137]. Our approach is unique in that we simultaneously probe the valence band response as well as the 4f MLD upon laser excitation. This allows us, for the first time, to measure all the states that are involved in the magnetism of the lanthanide metals during and following laser excitation. We can therefore exclude common sources of errors such as offsets in t_0, the pump fluence or diversity in the sample quality; all problems that usually occur when one compares results from different experiments.

Figure 6.1 shows spectra of Gd and Tb for two opposite in-plane magnetization directions. As discussed in Ch. 3.3, a chiral geometry was chosen to measure the magnetization. Along with the 4f MLD signal, the pronounced 5d6s exchange splitting discussed in Ch. 5 can also be obtained from the spectra. The exchange splitting in Tb is determined in this chapter by fits to the spectrum at an emission angle of 8°, as described on page 67. The magnetization is changed in between two spectra by a pulsed coil[1] mounted in front of the sample at the measurement position. The high current pulses for the coil are generated through discharge of capacitors[2]. With this setup it is possible to magnetize Gd at 90 K. In the case of terbium, however, the magnetic field from the pulsed coil is not sufficient to change

[1] The coil has 10 windings and consists of a 2 mm thick tantalum wire.

[2] We used two capacitors (450 µF, 375 V) discharged by thyristors in a parallel configuration. For Gd it was sufficient to charge the capacitors to 100 V.

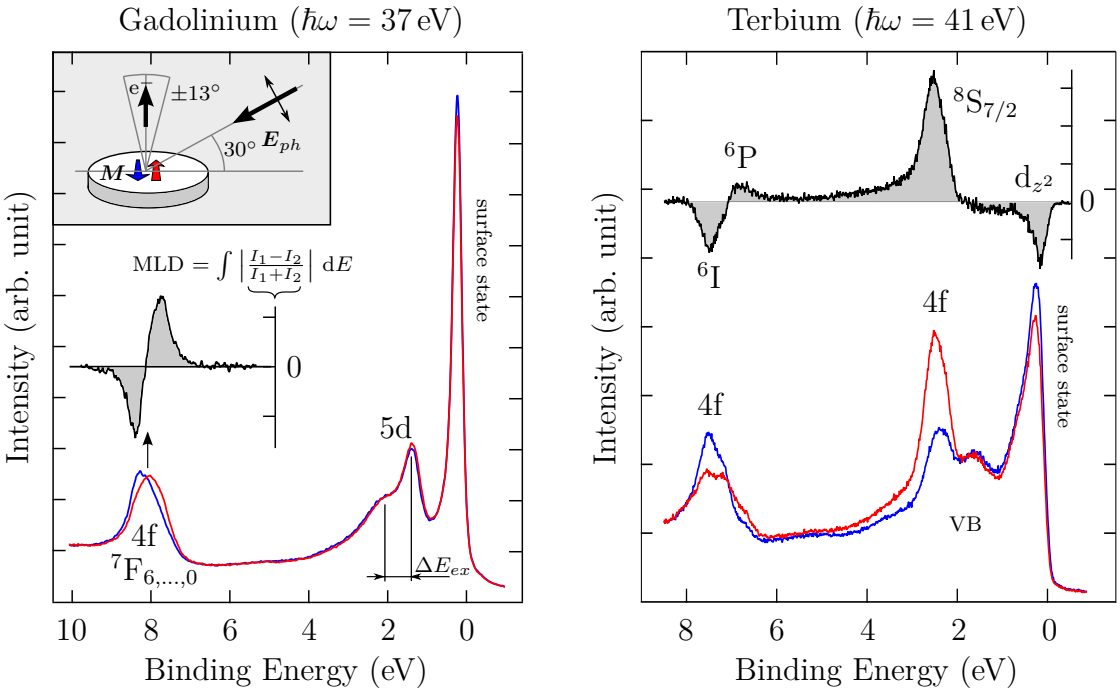

Figure 6.1: The valence band and 4f magnetic linear dichroism of gadolinium and terbium at 90 K. *The blue and red EDCs show the ARPES spectra probed with p-polarized light in normal emission for two opposite in-plane magnetization directions (geometry as shown in the inset). In Gd the exchange split (5d6s) valence bands at 2 eV binding energy, the surface state just below E_F and the 4f core level at 8 eV are clearly visible. The Gd 4f final state consists of 7 multiplet components $^7F_{6,\ldots,0}$ (from left to right) which are not resolvable. An additional surface core level shift of about 0.4 eV* makes it difficult to distinguish between surface and bulk contributions of the atomic MLD in our geometry [105]. The MLD signal is obtained by integration over the absolute value of the normalized difference of the blue and red spectra. In Tb (right) the MLD signal is a lot larger than in Gd. Especially the high spin $^8S_{7/2}$ final state component shows a remarkably strong dichroic effect. The "low" spin multiplet at 7.5 eV consists of three components ^6D, ^6I, ^6P whereas ^6I dominates at our photon energies. There are other multiplet terms at higher binding energies which are not within our energy window. Note that in Tb all components undergo a surface core level shift of ≈ 0.26 eV [172] with a strong signature at the used photon energies. In addition to the 4f multiplet MLD, a small dichroic signal is also present in the d_{z^2} surface state.*

* From our fits we get the best result for a surface core level shift of ≈ 0.41 eV. Kammerer et al. determined it to be 0.48 eV [191]. A theoretical estimation given in [192] quantified the shift to be about 0.3 - 0.4 eV.

the magnetization direction. We therefore heated Tb above the Curie temperature and subsequently cooled it slowly while constantly pulsing the coil. This way we can change the magnetization in Tb as well. Using a pulsed coil during cooling, instead of applying a constant current to a coil with many windings, has the advantage that the coil does not get hot and degas.

For the following discussion on the MLD dynamics it is helpful to recall what the different signals measure. As discussed previously, the exchange splitting measures the short-range magnetic order of the 5d6s electrons in the bulk[3]. In contrast MLD measures macroscopic magnetic order with an estimated surface to bulk signal ratio of 5/3 in Gd and 10/3 in Tb (cf. Ch. 3.3.2). The fact that MLD measures the macroscopic order has the consequence that the signal will vanish if the probed region breaks up into randomly oriented domains. This can happen when the absorbed pump fluence is high enough to completely demagnetize the sample. We found that this fluence is about $4\,\mathrm{mJ/cm^2}$ in Tb. Above this threshold the MLD signal is permanently destroyed because the remnant magnetic field from the surrounding unpumped sample regions is not sufficient to ensure realignment in the original direction. Thus we chose a relatively low absorbed fluence of $2.5\,\mathrm{mJ/cm^2}$ in Tb to assure a residual magnetization of about 30 % and realignment in the original direction at long pump-probe delays. For Gd we use $3.5\,\mathrm{mJ/cm^2}$, a value which leads to considerable demagnetization with still tolerable IR space charge.

6.1.1 Analysis of the MLD signal

During the evaluation of the time-resolved data we found, besides the delay-dependent space-charge shift discussed above (cf. Ch. 4.2), an additional slight shift of the Gd spectra for opposite magnetization directions which is only present at negative pump-probe delays up to about 1 ps. The shift is absent in static measurements and also not visible at 500 ps, where IR space charge is gone (see Fig. 6.2). Even though this shift is relatively small (about 30 meV), its influence on the 4f MLD signal is significant and needs to be addressed. Before applying any correction we need to make sure that the shift applies to the whole spectrum and is the same for all states. The inset of Fig. 6.2 shows that not only the surface state, but the whole valence band structure is shifted. The same shift can also be seen at the small oxygen peak at 27 eV kinetic energy and is the same for all angles in the two-dimensional spectra. There is, besides space charge, no physical explanation for such a shift at negative delays, making a correction imperative. For a complete discussion about the influence of the correction on the dynamics see Appx. A.1.

In contrast to Gd such a shift was not found in Tb, where the IR space charge is much smaller because of the higher work function. We therefore do not need to correct the Tb data and the analysis of the MLD signal is straightforward. The strong contrast at the high spin final state is particularly suitable for evaluation.

[3] The probed region is, with 2 - 3 topmost layers, the same for the 4f and the 5d6s photoelectrons, but the exchange split 5d6s bands are bulk bands and the corresponding electrons have an estimated coherence length of about 30 Å i.e. 10 ML.

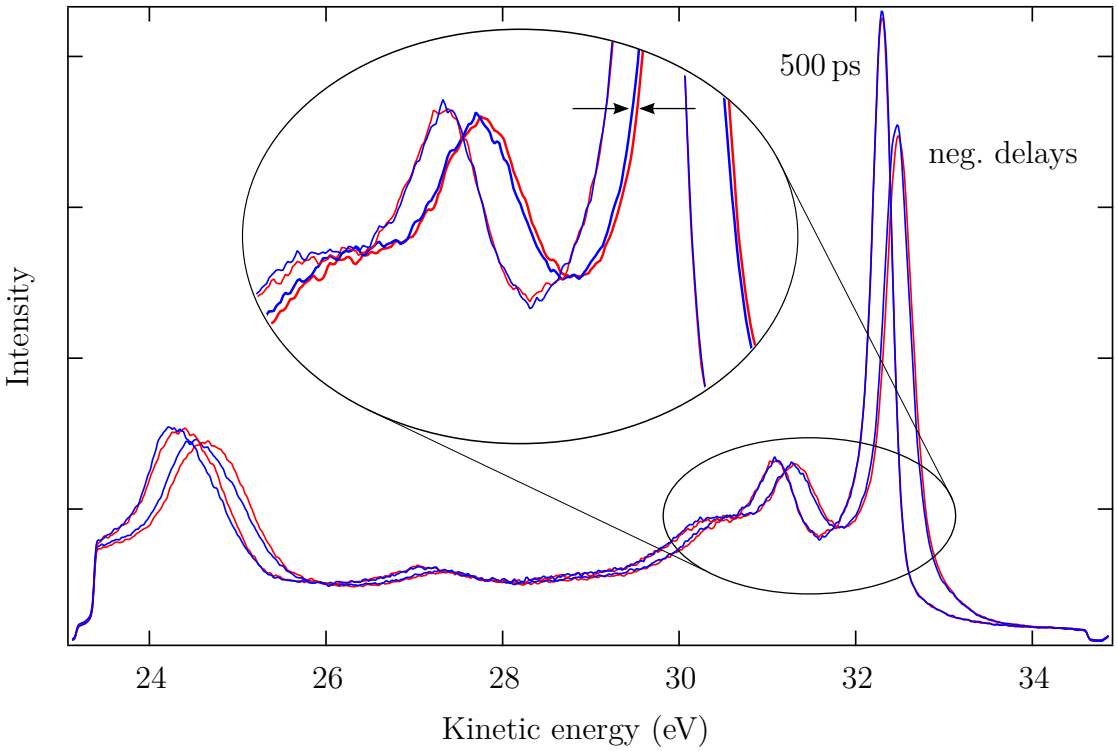

Figure 6.2: Space-charge effects in Gd MLD. *Besides the "normal" IR space-charge shift of about 0.2 eV between spectra taken at 500 ps (left) and negative pump-probe delays (-1 ps to t_0) a small shift of ≈ 30 meV between spectra with opposite magnetization directions (red and blue) can only be observed up to about 1 ps (see arrows in the inset for the shift at negative delays).*

The only peculiarity that has to be taken into account is that the common normalization (i.e. division of the difference spectrum by the sum of both spectra) does not work for this state since it overlaps with the majority component of the 5d6s bands, which moves with the pump-probe delay. Therefore, the normalization would lead to a slower observed response in the MLD signal, since the intensity from the majority state gets less within this region as it shifts to lower binding energies. The low spin multiplet components at 7.5 eV binding energy do not have this problem and by comparing here the normalized with the unnormalized MLD signal we find no significant difference. We therefore use only a normalization to the probe intensity for the individual spectra, i.e. we divide each spectrum by the background intensity. This way we can facilitate the intense high spin final state component to follow the polarization of the 4f system.

6.1.2 Laser-driven demagnetization of the 4f system

With the combined measurement of the 5d6s exchange splitting and 4f MLD, we can now directly investigate the intra-atomic exchange interaction between 4f and 5d6s states as we drive the magnetic system out of equilibrium. Intra-atomic exchange is regarded as the strongest force in magnetism and, up to now, only the much weaker inter-atomic exchange has been investigated by element-specific

probing of magnetic alloys. From these measurements it was claimed that at least the inter-atomic exchange can be overcome at sub-picosecond timescales [22, 193–195]. However, it should be noted that intrinsically, i.e. in a perfect alloy of two itinerant magnets, no distinct behavior can be present, because the valence band electrons responsible for the magnetic coupling are smeared out over several atoms. The simplest interpretation of some of the above observations (in particular in [193]) is thus that the distinct dynamics stem from regions with different compositions, where the respective dominant constituent then sets the timescale. This interpretation is also largely supported by spatially-resolved measurements, where nonlocal spin transport between regions of different compositions was found to have a strong influence on the dynamics [156]. The only other possibility, in the special case of RE-TM ferrimagnets, is a principal difference in the magnetic response of the localized RE core-level electrons and the shared itinerant RE-TM electrons. In this case it should be possible to measure the distinct behavior in a mono-atomic RE magnet as well, since it has both itinerant and localized electrons participating in the magnetization dynamics. In the RE metals observed here the intra-atomic exchange parameter is much bigger than the exchange between the atoms (in Gd: $J_{5d-4f} = 130\,\mathrm{meV}$, $J_{5d-5d} = 5.9\,\mathrm{meV}$ [23]). This is why instantaneous alignment of on-site moments and, hence, identical spin dynamics has been assumed so far.

Figure 6.3 shows the orbital-resolved dynamics for both, Gd and Tb, following laser excitation. As before, we have the distinct minority (red) and majority (blue) band response in Gd (left) and the faster and more symmetric behavior in Tb (right). The exchange splitting (black) shows a time constant of $0.7 \pm 0.1\,\mathrm{ps}$ in Gd which is as expected at the low fluence. In Tb the time constant of $0.3 \pm 0.1\,\mathrm{ps}$ is, within the error bars, the same as measured before at a higher fluences. If we now have a look at the corresponding MLD dynamics we see a remarkable discrepancy between Gd and Tb. While in Tb the MLD signal and the exchange splitting follow each other closely ($\tau_{MLD} = 0.4 \pm 0.1\,\mathrm{ps}$, $\tau_{ex} = 0.3 \pm 0.1\,\mathrm{ps}$) they show strikingly different dynamics in Gd.

The 5d6s exchange splitting in Gd reaches its minimum value after about 1 - 2 ps, by which time the electron and phonon heat baths are in equilibrium. In contrast the 4f magnetization hardly changes within the first two picoseconds, but continues to decrease until a minimum value at about 40 ps. The time constants obtained by single exponential fits reflect this behavior, with $0.7 \pm 0.1\,\mathrm{ps}$ for the exchange splitting and $14 \pm 3\,\mathrm{ps}$ for the MLD contrast. This slow response of the Gd 4f system is not to be expected and poses serious questions to our understanding of ultrafast magnetism. Naively one would expect that the strong 5d - 4f exchange coupling with $J_{int} = 130\,\mathrm{meV}$ would translate into a timescale of about 6 fs ($\tau \sim \hbar / J_{int}$), but it should be noted that this is only an upper limit for the fastest possible timescale. In general, the coupling depends not only on the interaction energy but also on the symmetry of the corresponding states.

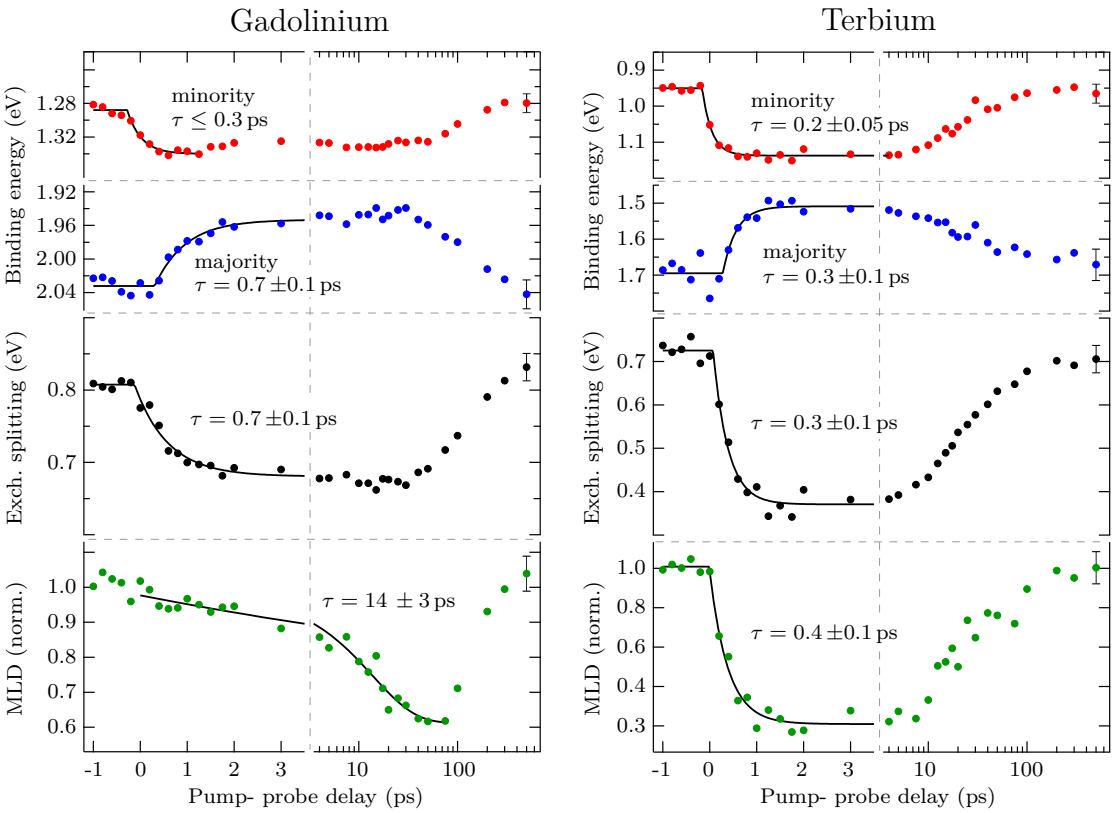

Figure 6.3: Magnetization dynamics of itinerant and localized electrons in Gd (left) and Tb (right). *The upper panels show the response of the minority (red) and majority (blue) 5d6s spin bands upon laser excitation. Their dynamics result in a reduction of the exchange splitting (black) with a time constant of 0.7 ps in Gd and 0.3 ps in Tb. In Gd the polarization of the 4f state (green, normalized) stays relatively unperturbed and diminishes with a much slower time constant of 14 ps while in Tb it follows closely the exchange splitting. Both the exchange splitting and the MLD signal are fitted with a single exponential function to obtain the given time constants. The initial sample temperature is 90 K and the spectra are recorded with 100 fs, 36.8 eV probe photon pulses. The sample is pumped by 300 fs (100 fs for Tb), 1.6 eV photon pulses with an absorbed fluence of 3.5 mJ/cm^2 in Gd and 2.5 mJ/cm^2 in Tb. Error bars on the last data points show two standard deviations.*

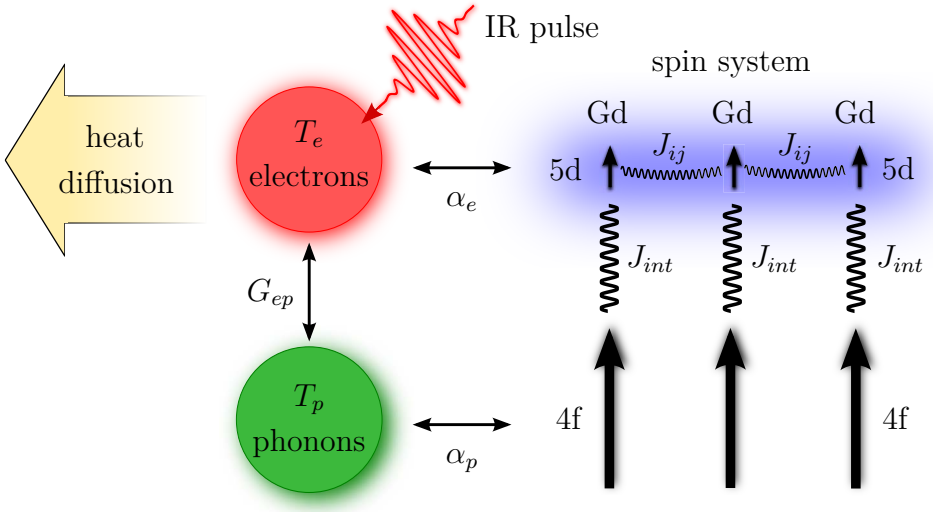

Figure 6.4: Extended three-temperature model. *In contrast to the ordinary 3TM the extended model takes heat diffusion of hot electrons and the complex inner structure of the Gd (or Tb) spin system into account. A schematic of the coupling within the spin system is given on the right. Two spins on atoms i and j interact through the coupling constant J_{ij} of the 5d electrons. Since these electrons are close to the Fermi level they are directly influenced by the electron temperature via α_e. Besides the intra-atomic coupling J_{int}, which describes the exchange between 4f and 5d electrons, the 4f spin system is also coupled to the phonon temperature via α_p.*

6.1.3 Orbital-resolved spin-dynamics simulations

To shed light on the origin of this strikingly disparate magnetization dynamics of the 5d6s exchange splitting and the 4f spin system, Wienholdt *et al.* performed atomistic spin dynamics simulations based on the E3TM (cf. pp. 19 ff.). Such an orbital-resolved model is required to describe the two distinct spin systems. Within this model the 5d6s electrons are represented by localized 5d moments, which are coupled to the electron temperature because they are directly excited by the laser pulse ($\hbar\omega = 1.6\,\mathrm{eV}$). In contrast, the 4f electrons are not perturbed by the laser, as their binding energies lie 8 eV below (occupied) and 4 eV above (unoccupied) the Fermi energy [151]. They therefore couple only to the phonon temperature. This is illustrated in Fig. 6.4 with the corresponding coupling parameters α_e and α_p.

The spin system in this figure is represented by the Hamiltonian from Ch. 2.1.3:

$$\mathcal{H} = -\frac{1}{2}\sum_{\langle ij\rangle} J_{ij}\boldsymbol{S}_i^{5d}\cdot\boldsymbol{S}_j^{5d} - \sum_i J_{int}\boldsymbol{S}_i^{5d}\cdot\boldsymbol{S}_i^{4f} - K^0\sum_i (S_i^{5d})_z^2 \tag{6.1}$$

with 5d and 4f spins expressed by the unit vectors $\boldsymbol{S}_i^{5d}$ and $\boldsymbol{S}_i^{4f}$ respectively, representing the normalized magnetic moments in the classical limit. The first term describes the inter-atomic Heisenberg exchange between the 5d spins at different lattice sites i, j of the hcp lattice. The second term is the intra-atomic exchange between the 4f and the 5d electrons, and the third term accounts for uniaxial

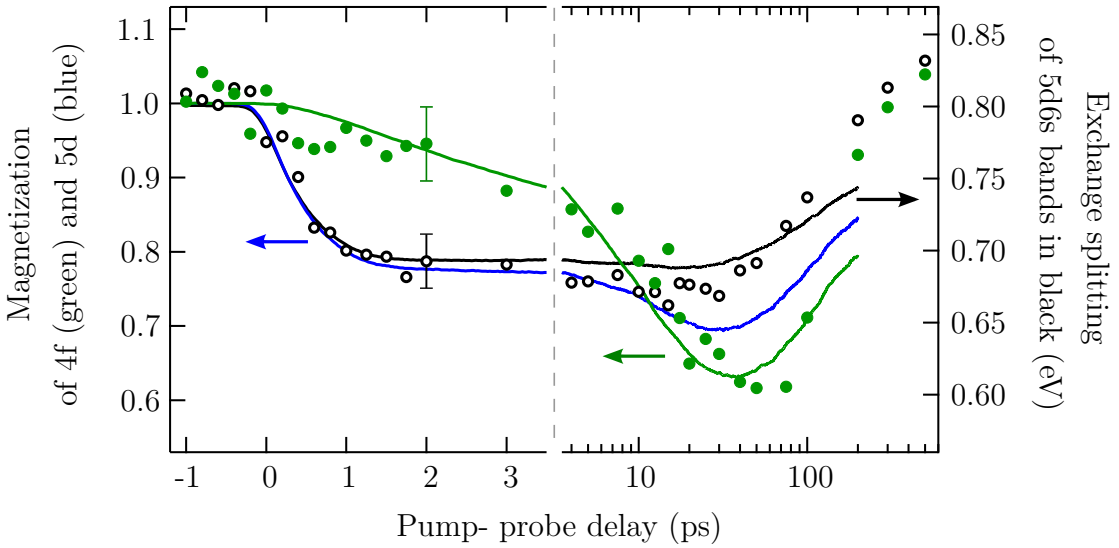

Figure 6.5: Orbital-resolved spin dynamics in gadolinium. *Measured exchange splitting of the 5d6s bulk bands (black circles, right ordinate) and normalized magnetic linear dichroism of the 4f state (green dots, left ordinate) are shown as a function of pump-probe delay. Solid green and blue lines are the (normalized) 4f and 5d magnetic moments, respectively, calculated with the orbital-resolved spin Hamiltonian. The black solid line is the exchange splitting computed ab initio with the 4f and 5d magnetic moments of the spin-dynamics simulations as input. The decoupling of the intra-atomic exchange is demonstrated by the significantly different demagnetization times of the 5d and 4f spin systems. Note that after 3.5 ps the dynamic is displayed on a logarithmic scale to cover the cooling back to the initial sample temperature of 90 K. Typical error bars ($\pm 2\,\sigma$) are shown for the data points at 2 ps pump-probe delay.*

anisotropy (cf. Ch. 2.1.2). Using the LLG equation with the above coupling we can now describe the dynamics of the 5d and 4f spin systems separately. For the 5d spins it reads:

$$\dot{\boldsymbol{S}}_i^{5d} = -\frac{\gamma}{(1+\alpha_e^2)\,\mu_s^{5d}}\,\boldsymbol{S}_i^{5d} \times \boldsymbol{H}_i(t) - \frac{\alpha_e \gamma}{(1+\alpha_e^2)\,\mu_s^{5d}}\,\boldsymbol{S}_i^{5d} \times \left(\boldsymbol{S}_i^{5d} \times \boldsymbol{H}_i(t)\right) \tag{6.2}$$

and analogue for the 4f moments:

$$\dot{\boldsymbol{S}}_i^{4f} = -\frac{\gamma}{\left(1+\alpha_p^2\right)\mu_s^{4f}}\,\boldsymbol{S}_i^{4f} \times \boldsymbol{H}_i(t) - \frac{\alpha_p \gamma}{\left(1+\alpha_p^2\right)\mu_s^{4f}}\,\boldsymbol{S}_i^{4f} \times \left(\boldsymbol{S}_i^{4f} \times \boldsymbol{H}_i(t)\right) \tag{6.3}$$

the effective field $\boldsymbol{H}_i(t)$ includes thermal fluctuations and is the connection to the rate equations of the E3TM (for details see Ch. 2.2). Good agreement between simulation and experiment is achieved by using coupling values of $\alpha_e = 1.3 \cdot 10^{-4}$ and $\alpha_p = 1.5 \cdot 10^{-3}$. Distinct values for α_e and α_p are not known in literature, but the average is in agreement with the known Gilbert damping $\alpha = 4.4 \cdot 10^{-4}$ of Gd [196].

The used exchange constants $J_{ij} = 5.9\,\text{meV}$ and $J_{int} = 130\,\text{meV}$ are calculated *ab initio* using density functional theory. These values lead to a computed Curie

temperature of 299 K, which is in close agreement with the experimental value of 293 K. The 5d and 4f magnetic moments from the simulation can thereby be used as an input for the calculation of the 5d6s exchange splitting for a given non-collinear 4f and 5d arrangement.

The results of the simulations are shown in Fig. 6.5 as solid lines. Even though the massive internal exchange interaction ($J_{int} = 130$ meV) is taken into account, the simulation supports the measured disparate timescales. This demonstrates that the strong exchange does not determine the demagnetization timescale of the 4f system. In fact by varying J_{int} it can be shown that only the 5d dynamics is influenced; the 5d system tends to remagnetize after the initial excitation if the 5d-4f exchange is enhanced, but the amount of angular momentum in the 5d system is not sufficient to change the 4f dynamics significantly (see Appx. A.2 for details). The (normalized) magnetization of the 4f and 5d systems from the simulation are given by the green and blue lines respectively. From these, the 5d6s exchange splitting is calculated (black) and given on the right ordinate. The simulation mirrors the slow (14 ps) 4f response as well as the sub-picosecond 5d demagnetization reasonably well. Also, the amplitude of the demagnetization is reproduced by using an absorbed fluence of 4 mJ/cm^2 in the simulation, which is well within the error bars of the measured absolute value of 3.5 ± 1 mJ/cm^2. The somewhat slower recooling after 50 ps is attributed to the exclusion of phonon heat transport in the model.

6.1.4 Comparison with XMCD measurements of Gd

The 14 ± 3 ps slow response of the Gd 4f system was unexpected and contradicts earlier findings from time-resolved XMCD measurements [175]. In these x-ray transmission experiments, Wietstruk *et al.* probed the M_5 edge ($3d_{5/2} \rightarrow 4f^{\downarrow}$) of a polycrystalline gadolinium film in between yttrium cap layers. They reported an initial drop in the XMCD signal of about 40 % with a time constant of 0.76 ± 0.25 ps followed by an additional decrease of 15 % with a time constant of 40 ± 10 ps as shown in Fig. 6.6. The fluence used in this experiment was 3 - 5 mJ/cm^2 and is thus comparable to the one in our measurement. We first assumed that the bulk sensitivity and the sample crystallinity together with the influence of the cap layers is the reason for this discrepancy. But recent XMCD experiments on single-crystalline Gd(0001)/W(110), done in cooperation with Wietstruk *et al.* at the BESSY femtoslicing facility, could qualitatively reproduce their earlier findings[4]. These particular experiments were not quite as surface sensitive as the MLD measurement. Using a reflection geometry in grazing incidence, the probed volume (which is determined by the penetration depth of the X-rays) can be calculated and is about 4 ML for the used angle of 4°. In conclusion, we can rule out that the crystallinity of the Gd film or the presence of cap layers are responsible for the fast XMCD response. In addition, it seems unlikely that the slightly larger probed volume would lead to such a strong additional contribution. Therefore, the fundamental question arises if MLD and XMCD are sill equivalent techniques and

[4] These measurements are not part of this thesis.

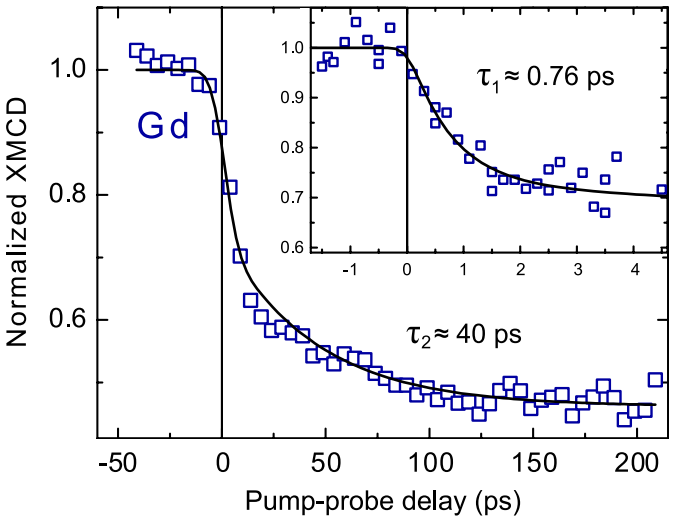

Figure 6.6: XMCD from polycrystalline Gd as a function of pump-probe delay; from Ref. [175]. *XMCD finds, contrary to MLD, two timescales in the Gd 4f system. A slow one of about 40 ± 10 ps (measured with a 10 ps probe pulses) and a fast one of 0.76 ± 0.25 ps (inset, measured with 120 fs probe pulses). In both cases the Gd sample was excited by a 50 fs long 1.5 eV pulse with a fluence of 3 - 5 mJ/cm².*

whether they show solely magnetism on ultrafast timescales.

Both, MLD as well as XMCD, are based on the same physical principles, they both result from electric dipole transitions as described by Fermi's golden rule, and both have similar selection rules[5]. The dichroic signal is the result of the different transition probabilities for reversed magnetization directions. But there are also some fundamental differences. XMCD is a measure of the optical properties; by choosing photon energies which are resonant to an excitation from an occupied nonmagnetic core level to a magnetic (polarized) final state one measures either reflectivity or absorption of the sample. The spin of the electron is conserved in this process and since the excitation is into an unoccupied but polarized state, the dichroism is a direct result of the Pauli principle. In contrast, MLD measures directly the photoelectrons, i.e. their transition from a magnetic initial state into a continuum final state. In this case, dichroism is a result of the interaction between the photoelectron and the core hole [197]. As a consequence XMCD probes the magnetic response of the unoccupied minority 4f states, while MLD measures the occupied majority 4f multiplets in the final state configuration. Careful analysis of the obtained XMCD signals revealed also nonmagnetic contributions[6] in the dynamics that may also have a non-negligible influence on the observed dynamics.

Recent unpublished spin- and time-resolved photoemission measurements from the Gd surface state confirmed a slow response that corresponds with what we

[5]Exception: $\Delta m = 0$ in MLD and $\Delta m = \pm 1$ in XMCD

[6]These can be found by comparing the (normalized) dynamics of both magnetization directions. These non-magnetic contributions seem to be too small to be responsible for the fast response, but only under the assumption that they are essentially non-symmetric, i.e. that all symmetric contributions are necessarily of magnetic origin.

see in the 4f MLD data[7]. The fast response reported by other authors [170, 176] can be attributed to the instantaneous change in the occupation of this state, while its intrinsic spin polarization remains unchanged. However, an interpretation of the data that relies on disparate surface and bulk behavior would reignite a long lasting dispute about the existence of distinct surface magnetism that was fought in the 1990s [26, 144, 153, 155, 157–166] (cf. pp. 64f.). This discussion, which concerned only static measurements[8], is regarded to be settled in favor of non-disparate surface-bulk behavior, but the existence of a different magnetic response at the surface can not be rejected per se, since we know that effects like e.g. super-diffusive spin transport, hot electron driven lattice transitions and quenching [198] or canting [199] of spin states can indeed differ at the surface. Band structure calculations of Gd show that the various magnetic phases of the heavy lanthanides can be reproduced by solely changing the lattice constants of Gd [183]. Already a 1.2 % reduction of the c/a ratio would lead to an antiferromagnetical ordering in Gd. Therefore, an enhanced ferromagnetic coupling could be reached due to magnetostriction if the lattice expands in the c-direction. Such a process could, in principle, stabilize the magnetic order at the surface.

6.2 4f dynamics in Terbium

In Tb the various multiplet components are well separated in the photoelectron spectrum, which allows for a separate investigation of their dynamics. In our experiment we resolve the high spin final state component $^8S_{7/2}$ at 2.5 eV binding energy and two of the lower spin components (^6I and ^6P) at about 7 eV. The MLD signal is most intense for the $^8S_{7/2}$. To compare the high- and low-spin dynamics we chose the more pronounced ^6I component. In addition to the 4f MLD we also see a small dichroic signal from the surface state. The right hand side of Fig. 6.7 shows the recorded MLD spectrum with the term symbols assigned. Their dynamics are shown on the left panel. All components show basically the same behavior which suggests, by comparing it additionally with the exchange splitting (Fig. 6.3), that the magnetic system in Tb is close to equilibrium at all times. The reason for the different behavior of the Gd and Tb 4f system seems to be the high angular orbital momentum induced by the additional 4f electron in Tb (Gd: $L_{4f} = 0$, Tb: $L_{4f} = 3$). It assures a strong coupling to the lattice via single ion anisotropy (cf. Ch. 2.1.2) leading to a magnetocrystalline anisotropy energy of 11 meV, which is about three orders of magnitude larger than in Gd [40, 41, 60]. This strong magnetic coupling to the lattice can also be seen in the magnon band structure, which shows large phonon induced band gaps [174]. These interactions are missing in the Gd magnon band structure [64, 67].

The orbital-resolved spin model that explains the Gd dynamics can also be used for Tb. Unfortunately there exist no *ab initio* calculations for Tb exchange constants

[7] The spin polarization of the surface state decreases on the timescale of 15 ±8 ps while its energetic shift shows, in agreement with our data, a response that is a lot faster (cf. Fig. 5.11) – Beatrice Andres, Freie Universität Berlin, private communication.

[8] Specifically about the question if the surface has an enhanced Curie temperature.

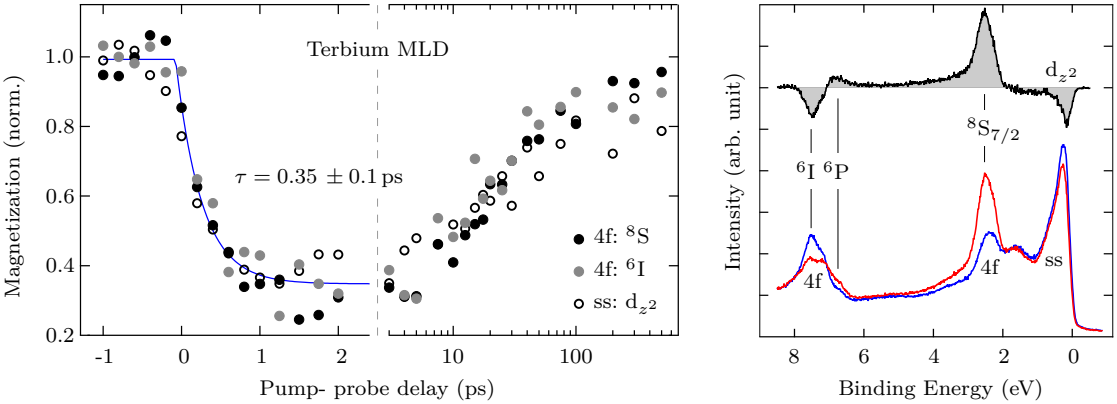

Figure 6.7: Component-resolved MLD as a function of pump probe delay. Left: *Shown are the high (●) and low (●) spin final state MLD contributions of the Tb 4f multiplet together with the dichroism from the d_{z^2} surface state (○) for an absorbed fluence of 2.5 mJ/cm^2. All components exhibit the same timescale of about 0.35 ps and, within the error bars (±0.1 for d_{z^2} and ±0.05 for ^8S and ^6I), the same level of normalized demagnetization. The blue line is a single exponential fit to all data points and serves as a guide to the eye.* ***Right:*** *Shown are EDCs at negative pump-probe delays for both magnetization directions (red and blue). The difference spectrum (shaded gray) is used to follow the magnetization of the different states.*

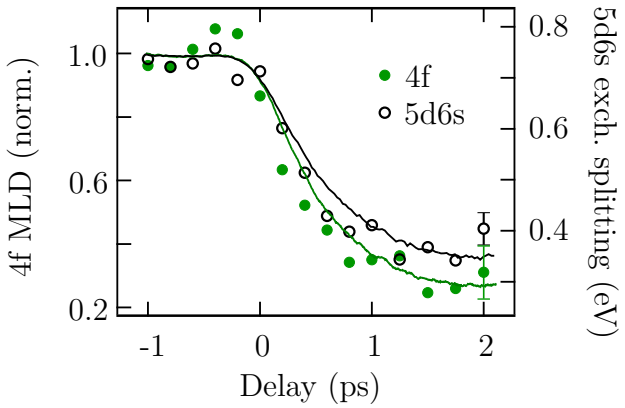

Figure 6.8: 5d6s exchange splitting and 4f MLD in Tb compared to the modified spin dynamic simulation of Gd. *The calculated lines were obtained by increasing the 4f phonon coupling of the Gd model to $\alpha_p = 0.5$; the amplitudes were adjusted to account for the lower T_C of Tb. Calculations by coauthors of [VI].*

since they are much more demanding to calculate than the Gd ones due to the finite angular momentum in the 4f shell. For a simple comparison of the key features it should be sufficient to use the Gd calculation and adapt the 4f coupling to the lattice. By using the values from [40, 41] for the MCA we can estimate the coupling to be a factor of 340 stronger than in Gd we thus change α_p from 0.0015 to 0.5. This increase is on the same order of magnitude as the factor between the Gilbert damping parameters found for Gd- and Tb- transition metal alloys with 0.0005 and 0.038 respectively [200, 201].

The result of the adapted spin-dynamics simulation is shown in Fig. 6.8 as solid lines. The calculation agrees well with the measured dynamics. Both, 4f and 5d6s polarization decrease with the same fast timescale, justifying our above assumption that spin-lattice coupling is responsible for the 4f timescale. The small (~ 0.1 ps) mismatch in the decay constant of the simulation with the data is most likely a consequence of the usage of the Gd *ab initio* calculation as an approximation for Tb. The fact that we can reproduce the experimental findings within the model of Wienholdt and coworkers shows that, despite the common belief that the 5d - 4f exchange sets the demagnetization timescale in RKKY magnets, it is in fact the direct spin lattice interaction of the 4f electrons.

Influence of oxygen adsorbates on the surface magnetism in Tb It was reported, that oxygen adsorption on Lanthanides suppress the magnetism of the surface layer [147]. This can, in principal, be used to separate the magnetic signal from the top most layer and the underlying bulk layers, making it possible to investigate their magnetization dynamics separately. The result of such an experiment is shown in Fig. 6.9. On the right hand side the energy distribution curves of the corresponding sample is shown. Blue and red spectra are opposite in plane magnetization directions in the chiral MLD geometry. The lower spectra show a pure Tb thin film, while the upper spectra stem from a Tb film with ~ 0.1 L oxygen deposited on the surface. The adsorbed oxygen results in a vanishing MLD signal from the surface state, as well as a reduced signal from the surface core level shifted multiplet components (marked by gray vertical lines, s). Even though the oxygen peak has the same intensity as the 4f multiplets (PE at $\hbar\omega = 41$ eV) it seems to be not enough to completely suppress the surface core level shift. The moderate oxygen dosing which was chosen here has also no significant influence on the magnetization dynamics as shown on the left hand side of Fig. 6.9. Here the $^8S_{7/2}$ component was chosen for comparison. The response upon laser excitation is convincingly unchanged by the deposited O_2. It is likely that also a higher deposition will not alter the dynamics significantly.

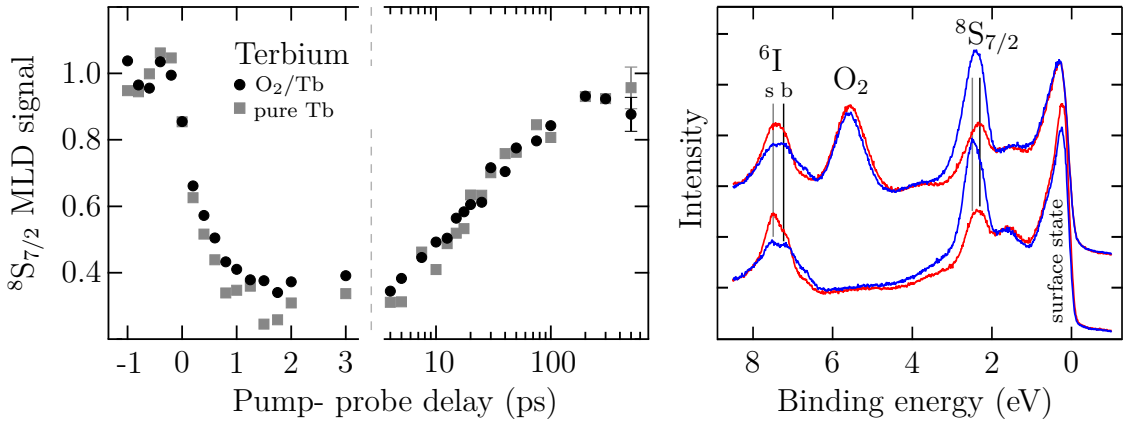

Figure 6.9: Influence of surface adsorbed oxygen on the magnetization dynamics. *Shown is the 4f MLD ^8S final state dynamics upon laser excitation for a Tb film with (●) and without (■) deposited oxygen. The corresponding energy distribution curves are given in the right panel. Deposition of oxygen leads to a reduction of the surface core level shifted multiplet components (s, gray lines) and a complete suppression of the surface state MLD signal. Probe: FWHM = 100 fs, $\hbar\omega = 41$ eV. Pump: FWHM = 100 fs, $\hbar\omega = 1.6$ eV, $F_{abs} = 2.5$ mJ/cm^2.*

Chapter 7

Summary and Outlook

The goal of this thesis was to shed light on to the microscopic processes which drive the ultrafast demagnetization in Gd and Tb after laser excitation. To this end we used a novel approach, combining valence band photoemission and core-level magnetic linear dichroism in a single pump-probe experiment. This way we were able to capture all the transient states that are involved in the magnetization dynamics. The experiment was made possible by a unique high-order harmonic setup which provided the needed time- and energy-resolution of the XUV-probe.

In summary, we have shown that the magnetic systems of single-crystalline Gd and Tb films exhibit very different behavior after laser excitation. Especially Gd is driven far from equilibrium, demonstrating that the intra-atomic exchange interaction, which is generally assumed to be quasi-instantaneous, is broken on a ten picosecond timescale. The distinct minority and majority spin dynamics in the valence band, reflecting the magnetization of the itinerant 5d6s electrons, give insights into the ultrafast processes comprising initial charge redistribution, as well as electron-electron and electron-magnon scattering. On slightly slower timescales we find EY-like spin-flips to be present in the 5d6s majority bulk band dynamics. The difference in the 4f response between Gd and Tb are attributed to ordinary spin-lattice coupling and can adequately be described by Gilbert damping using a ratio between the damping parameters of both metals which is also found in between their magnetocrystalline anisotropy energies. The strong spin-lattice coupling in Tb lead, thereby, to a fast response which keeps the magnetic system – contrary to Gd – close to equilibrium.

Besides these main results we examined in Gd the pump laser fluence and temperature dependence of the valence band dynamics and found comparable results to those obtained earlier by MOKE. With our method we contribute to this extremely active field by the additional insight into the origin of the dependency. The temperature dependence is driven by the fast minority bulk band, which we explain in terms of electron-electron and electron-magnon scattering. The fluence dependence on the other hand is driven by the slower majority bulk band, which can be explained by EY-scattering. We could also prove the conjecture that these bulk bands show residual exchange splitting above the Curie temperature, which we determined to be at least 100 meV at 320 K.

In addition to these physical insights, we raised questions about the comparability of different magnetic techniques in the ultrafast regime. In particular, the discrepancy between the MLD and the XMCD response needs further investigation. To this end it would be helpful to exclude space-charge influences in the MLD signal by using lower photon energies for the excitation. Besides this, it would be useful to perform XMCD measurements on single-crystalline Tb at comparable conditions to those presented here.

Repeating the experiments on an insulating substrate would help to gain insights into transport effects. Additionally, the role of the surface could be further investigated by repeating the Gd MLD experiment in Γ - K direction, where diffraction dichroism dominates. To this end, it could also prove helpful to cap the Gd sample with one monolayer of Eu or Tb. Eu as a cap layer has the advantage that the 4f multiplets are well separated from the Gd 4f, which would allow for a separate analysis of surface and bulk 4f magnetism. Tb on the other hand has the benefit of a very similar valence band structure which makes it possible to exclude the influence of the itinerant electrons at the interface.

Ultimately, the aim is to repeat the measurements presented in this thesis with spin resolution. This goal, however, requires high harmonic setups with much higher repetition rates since the fluence per shot is already limited by space charge and spin-resolving detectors are very inefficient.

In conclusion, in this work we have gained significant microscopic insights into the role of inter- and intra-atomic exchange coupling during laser driven demagnetization. The former, which is predominately influenced by Elliot-Yafet and exchange scattering is reflected by the dynamics of the itinerant electrons. The latter is, surprisingly, not sufficient to establish magnetic equilibrium on the ultrafast timescales and the dynamics of the localized spins are basically determined by spin-lattice interaction alone. This discrepancy, which shows that intra-atomic nonequilibrium conditions persists over several picoseconds, was observed for the first time and was not expected from existing theoretical understanding. With these key insights we have contributed significantly to the field of laser-driven magnetization dynamics, emphasizing that the role of lanthanide alloyants in all optical magnetic switching experiments of RE-TM ferrimangets could be ultimately determined by the interplay of their itinerant with the localized electrons.

Appendix

A.1 Space-charge correction of the Gd MLD data

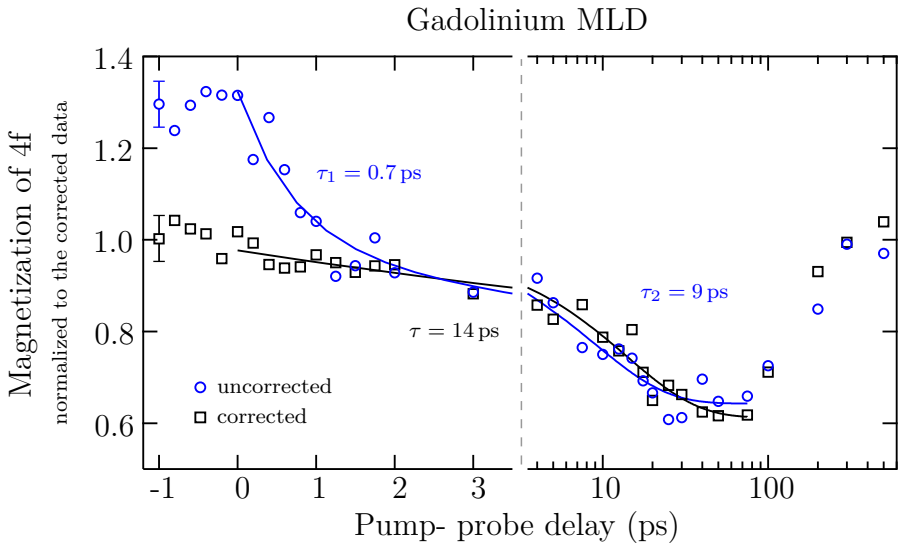

Figure A.1: Gd MLD as a function of pump-probe delay before (blue) and after (black) correction of the space-charge-induced shift. *The slight shift between the opposite magnetization directions discussed in Ch. 6.1.1 leads to an enhanced MLD signal at negative delays up to about 1 ps. From that delay on the shift is negligible and the dynamics are the same. The corrected data can be fitted with a single exponential function (black line) while the uncorrected data can only be reproduced by a double exponential function (blue line). The time constants of the fits are given in the figure.*

In Ch. 6 we discussed the 4f dynamics as measured by MLD. We found an unphysical shift in the Gd dataset starting at negative delays for which we corrected by aligning the spectra to their respective valence band positions. Figure A.1 shows this Gd MLD dynamics as measured (blue circles) and with the applied correction (black squares). If compared to earlier publications, e.g. by XMCD [175], the correction seems unjustified because XMCD finds a similar behavior with also a sub-picosecond contribution. We therefore carefully analyzed all our measured MLD datasets before we came to the conclusion that the correction is indeed necessary. The first hint for the necessity of the correction lies in the level of demagnetization. In the

uncorrected MLD data set, it is more than twice as strong as the one calculated from the 5d exchange splitting (65 % vs. 30 % at 40 ps pump-probe delay). This is not a strict proof though since MLD measures the overall magnetization in the probed spot and is therefore – in contrast to the exchange splitting – also influenced by macroscopic effects like the formation of different magnetic domains. This would in principal allow such dynamics but seems to be unreasonable at the timescales discussed here[1]. Also, for the corrected dataset, the MLD signal and the exchange splitting follow each other closely with both reaching their initial value at 500 ps. We investigated this matter more closely and, although we could not determine the origin of the shift, we found in some measurements an even reversed behavior. Finally, the strongest argument for the correction is its absence in the unpumped case, which must be identical to the situation at -1 ps delay, and the fact that all states are affected, as shown in Fig. 6.2. Although we do not know the microscopic mechanisms that would lead to a magnetization-dependent shift at negative delays, we know that the shift is induced by space charge and needs to be corrected.

A.2 Spin dynamic simulations

In Ch. 6.1.3 we have shown that, despite the strong intra-atomic exchange, 4f and 5d magnetism in Gd are out of equilibrium for tens of picoseconds. This could be reproduced by orbital-resolved spin dynamic simulations, from which we concluded that the 4f demagnetization is predominately driven by its direct coupling to the lattice. The obvious question is now about the role of the intra-atomic exchange during demagnetization. In Fig. A.2 this question is addressed; it shows simulations with different intra-atomic exchange parameters. The dynamics of the 4f system is, apart from an offset given by the respective initial magnetic moment, not significantly altered. The 5d dynamics on the other hand is strongly influenced by the intra-atomic exchange; a large exchange energy leads to a slight remagnetization of the 5d system to establish equilibrium. This result is remarkable; it shows that the small magnetic moment of the 5d electrons can not effectively drive the 4f magnetization.

[1] Apart from the timescales, it seems also unlikely because the sample is not completely demagnetized, and the thin film magnetization is dominated by shape anisotropy which would keep the direction of the easy axis.

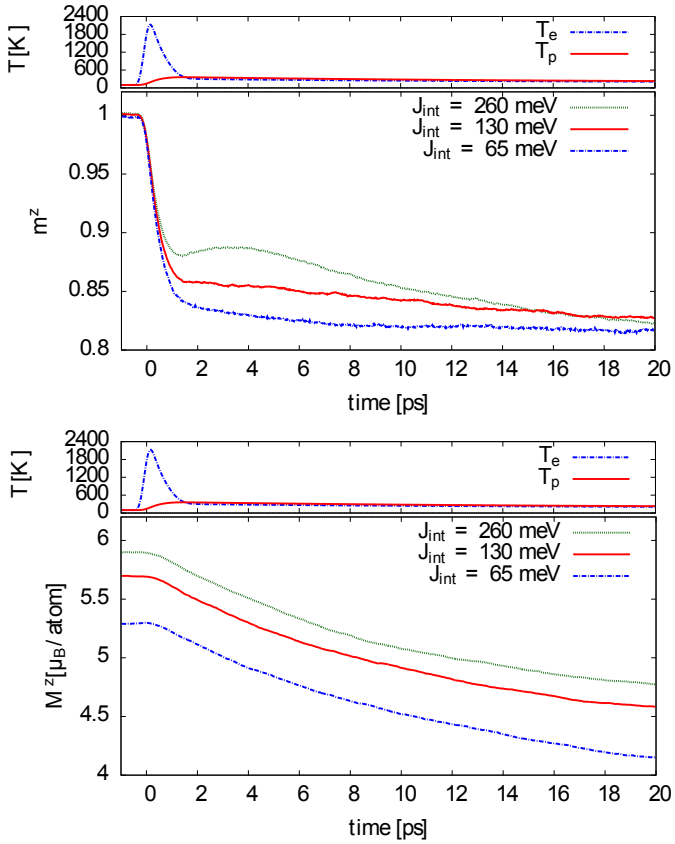

Figure A.2: Influence of the intra-atomic exchange interaction J_{int} on the orbital-resolved spin dynamic simulations. *The upper panel shows the calculated magnetic moment of the itinerant 5d electrons for the different intra-atomic coupling parameters. The bottom panel the respective calculated response of the magnetic moment of the localized 4f electrons. At the top of each panel are the used temperature transients for the calculation displayed. Calculations by Wienholdt and coworkers.*

Publications

[I] B. Frietsch, *"Laser Driven Magnetization Dynamics in Thin Lanthanide Films Studied by Time- and Angular-Resolved Photoemission using High-Order Harmonic Radiation"*, Diplomarbeit, Freie Universität Berlin (2011).

[II] R. Carley, K. Döbrich, B. Frietsch, C. Gahl, M. Teichmann, O. Schwarzkopf, P. Wernet and M. Weinelt, *"Femtosecond Laser Excitation Drives Ferromagnetic Gadolinium out of Magnetic Equilibrium"*, Physical Review Letters **109**, 057401 (2012).

[III] B. Frietsch, R. Carley, K. Döbrich, C. Gahl, M. Teichmann, O. Schwarzkopf, P. Wernet and M. Weinelt, *"A high-order harmonic generation apparatus for time- and angle-resolved photoelectron spectroscopy"*, Review of Scientific Instruments **84**, 075106 (2013).

[IV] B. Frietsch, J. Bowlan, R. Carley, M. Teichmann, J. Wolter, and M. Weinelt *"The valence band structure of Gadolinium studied with time-resolved photoemission"*, in Ultrafast Magnetism I (J.-Y. Bigot, W. Hübner, T. Rasing and R. Chantrell, eds.), Springer Proceedings in Physics **159**, 274–277 (2015).

[V] M. Teichmann, B. Frietsch, K. Döbrich, R. Carley, and M. Weinelt. *"Transient band structures in the ultrafast demagnetization of ferromagnetic gadolinium and terbium"*, Physical Review B **91**, 014425 (2015).

[VI] B. Frietsch, J. Bowlan, R. Carley, M. Teichmann, S. Wienholdt, D. Hinzke, U. Nowak, K. Carva, P. M. Oppeneer and M. Weinelt, *"Disparate ultrafast dynamics of itinerant and localized magnetic moments in gadolinium metal"*, Nature Communications **6**, 8262 (2015).

[VII] B. Frietsch, R. Carley, M. Teichmann, J. Bowlan, and M. Weinelt *"Transient States in the Demagnetization of Gd – Signatures of the Underlying Microscopic Processes"*, Proceedings of the Ultrafast Magnetism Conference 2015 – **in press**.

Bibliography

[1] J. Stöhr and H. Siegmann. *Magnetism*. Springer, 2007.
(Cit. on p. 1.)

[2] A. Vaterlaus, T. Beutler, and F. Meier. "Spin-lattice relaxation time of ferromagnetic gadolinium determined with time-resolved spin-polarized photoemission". In: *Phys. Rev. Lett.* **67** (1991), 3314.
(Cit. on pp. 1, 17.)

[3] W. Hübner and K. H. Bennemann. "Simple theory for spin-lattice relaxation in metallic rare-earth ferromagnets". In: *Phys. Rev. B* **53** (1996), 3422.
(Cit. on p. 1.)

[4] E. Beaurepaire, J.-C. Merle, A. Daunois, and J.-Y. Bigot. "Ultrafast Spin Dynamics in Ferromagnetic Nickel". In: *Phys. Rev. Lett.* **76** (1996), 4250.
(Cit. on pp. 1, 17, 59.)

[5] G. P. Zhang and W. Hübner. "Laser-Induced Ultrafast Demagnetization in Ferromagnetic Metals". In: *Phys. Rev. Lett.* **85** (2000), 3025.
(Cit. on pp. 1, 17.)

[6] G. Zhang and T. George. "Total angular momentum conservation in laser-induced femtosecond magnetism". In: *Phys. Rev. B* **78** (2008), 1.
(Cit. on p. 1.)

[7] J.-Y. Bigot, M. Vomir, and E. Beaurepaire. "Coherent ultrafast magnetism induced by femtosecond laser pulses". In: *Nature Phys.* **5** (2009), 515.
(Cit. on pp. 1, 81.)

[8] E. Beaurepaire, G. M. Turner, S. M. Harrel, M. C. Beard, J.-Y. Bigot, and C. A. Schmuttenmaer. "Coherent terahertz emission from ferromagnetic films excited by femtosecond laser pulses". In: *Appl. Phys. Lett.* **84** (2004), 3465.
(Cit. on p. 1.)

[9] M. Fähnle, M. Haag, and C. Illg. "Is the angular momentum of a ferromagnetic sample after exposure to a fs laser pulse conserved? " In: *J. Magn. Magn. Mater.* **347** (2013), 45.
(Cit. on p. 1.)

[10] E. Carpene, E. Mancini, C. Dallera, M. Brenna, E. Puppin, and S. De Silvestri. "Dynamics of electron-magnon interaction and ultrafast demagnetization in thin iron films". In: *Phys. Rev. B* **78** (2008), 174422.
(Cit. on p. 1.)

[11] M. Krauß, T. Roth, S. Alebrand, D. Steil, M. Cinchetti, M. Aeschlimann, and H. Schneider. "Ultrafast demagnetization of ferromagnetic transition metals: The role of the Coulomb interaction". In: *Phys. Rev. B* **80** (2009), 180407.
(Cit. on p. 2.)

[12] B. Koopmans, H. Kicken, M. van Kampen, and W. de Jonge. "Microscopic model for femtosecond magnetization dynamics". In: *J. Magn. Magn. Mater.* **286** (2005), 271.
(Cit. on p. 2.)

[13] B. Koopmans, J. Ruigrok, F. Dalla Longa, and W. de Jonge. "Unifying Ultrafast Magnetization Dynamics". In: *Phys. Rev. Lett.* **95** (2005), 267207.
(Cit. on p. 2.)

[14] B. Koopmans, G. Malinowski, F. Dalla Longa, D. Steiauf, M. Fähnle, T. Roth, M. Cinchetti, and M. Aeschlimann. "Explaining the paradoxical diversity of ultrafast laser-induced demagnetization." In: *Nat. Mater.* **9** (2010), 259.
(Cit. on pp. 2, 18, 59, 71, 72, 83.)

[15] R. J. Elliott. "Theory of the Effect of Spin-Orbit Coupling on Magnetic Resonance in Some Semiconductors". In: *Phys. Rev.* **96** (1954), 266.
(Cit. on pp. 2, 18, 61.)

[16] Y. Yafet. "g Factors and Spin-Lattice Relaxation of Conduction Electrons". In: *Solid State Physics*. Solid State Physics **14** (1963). Ed. by F. Seitz and D. Turnbull, 1.
(Cit. on p. 2.)

[17] M. Battiato, K. Carva, and P. M. Oppeneer. "Superdiffusive Spin Transport as a Mechanism of Ultrafast Demagnetization". In: *Phys. Rev. Lett.* **105** (2010), 1.
(Cit. on pp. 2, 59, 62, 74.)

[18] M. Fähnle and C. Illg. "Electron theory of fast and ultrafast dissipative magnetization dynamics." In: *J. Phys.: Condens. Matter* **23** (2011), 493201.
(Cit. on p. 2.)

[19] I. A. Yastremsky, P. M. Oppeneer, and B. A. Ivanov. "Theory of fast time evolution of nonequilibrium spin states in magnetic heterostructures". In: *Phys. Rev. B* **90** (2014), 024409.
(Cit. on p. 2.)

[20] S. Essert and H. Schneider. "Electron-phonon scattering dynamics in ferromagnetic metals and their influence on ultrafast demagnetization processes".

In: *Phys. Rev. B* **84** (2011), 224405.
(Cit. on p. 2.)

[21] C. D. Stanciu, F. Hansteen, A. V. Kimel, A. Kirilyuk, A. Tsukamoto, A. Itoh, and T. Rasing. "All-Optical Magnetic Recording with Circularly Polarized Light". In: *Phys. Rev. Lett.* **99** (2007), 047601.
(Cit. on p. 2.)

[22] I Radu, K Vahaplar, C Stamm, T Kachel, N Pontius, H. a. Dürr, T. a. Ostler, J Barker, R. F. L. Evans, R. W. Chantrell, a Tsukamoto, a Itoh, a Kirilyuk, T. Rasing, and a. V. Kimel. "Transient ferromagnetic-like state mediating ultrafast reversal of antiferromagnetically coupled spins." In: *Nature* **472** (2011), 205.
(Cit. on pp. 2, 89.)

[23] S. Wienholdt, D. Hinzke, K. Carva, P. M. Oppeneer, and U. Nowak. "Orbital-resolved spin model for thermal magnetization switching in rare-earth-based ferrimagnets". In: *Phys. Rev. B* **88** (2013), 020406.
(Cit. on pp. 2, 7, 11, 16, 19, 89.)

[24] P. Kurz, G. Bihlmayer, and S. Bügel. "Magnetism and electronic structure of hcp Gd and the Gd(0001) surface". In: *J. Phys.: Condens. Matter* **14** (2002), 6353.
(Cit. on pp. 4, 5, 62, 70, 74.)

[25] C. Santos, W. Nolting, and V. Eyert. "Ferromagnetism and temperature-dependent electronic structure of hcp gadolinium". In: *Phys. Rev. B* **69** (2004), 214412.
(Cit. on p. 4.)

[26] D. Li, J. Pearson, S. D. Bader, D. N. McIlroy, C. Waldfried, and P. A. Dowben. "Spin-polarized photoemission studies of the exchange splitting of the Gd 5d electrons near the Curie temperature". In: *Phys. Rev. B* **51** (1995), 13895.
(Cit. on pp. 4, 62, 64, 95.)

[27] E. Weschke and G. Kaindl. "Magnetic exchange splitting in lanthanide metals". In: *J. Phys.: Condens. Matter* **13** (2001), 11133.
(Cit. on p. 4.)

[28] D. Wegner, A. Bauer, and G. Kaindl. "Magnon-broadening of exchange-split surface states on lanthanide metals". In: *Phys. Rev. B* **73** (2006), 165415.
(Cit. on p. 4.)

[29] K. Döbrich. "Bandstrukturen und Fermiflächen schwerer Lanthanidmetalle bei magnetischen Phasenübergängen". PhD thesis. Freie Universität Berlin, 2007.
(Cit. on pp. 4, 5, 57, 62, 74.)

[30] B. Kim, A. B. Andrews, J. L. Erskine, K. J. Kim, and B. N. Harmon. "Temperature-dependent conduction-band exchange splitting in ferromag-

netic hcp gadolinium: Theoretical predictions and photoemission experiments". In: *Phys. Rev. Lett.* **68** (1992), 1931.
(Cit. on pp. 5, 62.)

[31] R. L. Benbow. "Dipole selection rules for the hexagonal-close-packed lattice". In: *Phys. Rev. B* **22** (1980), 3775.
(Cit. on p. 4.)

[32] D. Pescia, A. R. Law, M. T. Johnson, and H. P. Hughes. "Determination of observable conduction band symmetry in angle-resolved electron spectroscopies: non-symmorphic space groups". In: *Solid State Commun.* **56** (1985), 809.
(Cit. on p. 4.)

[33] F. J. Darnell. "Temperature Dependence of Lattice Parameters for Gd, Dy, and Ho". In: *Phys. Rev.* **130** (1963), 1825.
(Cit. on pp. 7, 76.)

[34] F. J. Darnell. "Lattice Parameters of Terbium and Erbium at Low Temperatures". In: *Phys. Rev.* **132** (1963), 1098.
(Cit. on p. 7.)

[35] M. Farle, K. Baberschke, U. Stetter, A. Aspelmeier, and F. Gerhardter. "Thickness-dependent Curie temperature of Gd(0001)/W(110) and its dependence on the growth conditions". In: *Phys. Rev. B* **47** (1993), 11571.
(Cit. on pp. 7, 63.)

[36] F. Heigl, J. E. Prieto, O. Krupin, K. Starke, G. Kaindl, and M. Bode. "Annealing-induced extension of the antiferromagnetic phase in epitaxial terbium metal films". In: *Phys. Rev. B* **72** (2005), 035417.
(Cit. on p. 7.)

[37] H. E. Nigh, S. Legvold, and F. H. Spedding. "Magnetization and Electrical Resistivity of Gadolinium Single Crystals". In: *Phys. Rev.* **132** (1963), 1092.
(Cit. on p. 7.)

[38] L. W. Roeland, G. J. Cock, M. F. A., A. C. Moleman, K. A. McEwen, R. G. Jordan, and D. W. Jones. "Conduction electron polarization of gadolinium metal". In: *J. Phys. F: Met. Phys.* **5** (1975), L233.
(Cit. on p. 7.)

[39] L. Roeland, G. Cock, and P.-A. Lindgard. "High-field magnetization of Tb single crystals". In: *J. Phys. C: Solid State Phys.* **8** (1975), 3427.
(Cit. on p. 7.)

[40] S. Abdelouahed and M. Alouani. "Magnetic anisotropy in Gd, GdN, and $GdFe_2$ tuned by the energy of gadolinium $4f$ states". In: *Phys. Rev. B* **79** (2009), 054406.
(Cit. on pp. 7, 72, 95, 97.)

[41] J. Rhyne and A. E. Clark. "Magnetic Anisotropy of Terbium and Dysprosium". In: *J. Appl. Phys.* **38** (1967), 1379.
(Cit. on pp. 7, 15, 72, 95, 97.)

[42] C. Schüßler-Langeheine. "Magnetic Properties of Thin Films of Heavy Lanthanide Metals Studied by Magnetic X-Ray Diffraction and High-Resolution Photoemission." PhD thesis. Freie Universität Berlin, 1999.
(Cit. on pp. 7, 11, 54, 55, 57, 63, 65, 66, 73.)

[43] B. Andres. "Spinauflösende Zwei-Photonen-Photoemission an der Gadolinium (0001)-Oberfläche". Diplomarbeit. Freie Universität Berlin, 2010.
(Cit. on pp. 7, 53, 65, 67, 71.)

[44] V. S. Fomenko. "Work function of yttrium and lanthanide single crystals". In: *Powder Metall. Met. Ceram.* **33** (1994), 85.
(Cit. on pp. 7, 67, 71.)

[45] R. Ahuja, S. Auluck, B. Johansson, and M. S. S. Brooks. "Electronic structure, magnetism, and Fermi surfaces of Gd and Tb". In: *Phys. Rev. B* **50** (1994), 5147.
(Cit. on p. 11.)

[46] A. Liechtenstein, M. Katsnelson, V. Antropov, and V. Gubanov. "Local spin density functional approach to the theory of exchange interactions in ferromagnetic metals and alloys". In: *J. Magn. Magn. Mater.* **67** (1987), 65.
(Cit. on p. 11.)

[47] F. J. Himpsel. "Exchange splitting of epitaxial fcc Fe/Cu(100) versus bcc Fe/Ag(100)". In: *Phys. Rev. Lett.* **67** (1991), 2363.
(Cit. on p. 11.)

[48] E. C. Stoner. "Collective Electron Ferromagnetism. II. Energy and Specific Heat". In: *Proc. R. Soc. A* **169** (1939), 339.
(Cit. on p. 11.)

[49] H. Ibach and H. Lüth. *Festkörperphysik*. Springer, 2002.
(Cit. on p. 11.)

[50] W. Heisenberg. "Zur Theorie des Ferromagnetismus". In: *Zeitschrift für Physik* **49** (1928), 619.
(Cit. on p. 13.)

[51] B. N. Harmon and A. J. Freeman. "Spin-polarized energy-band structure, conduction-electron polarization, spin densities, and the neutron magnetic form factor of ferromagnetic gadolinium". In: *Phys. Rev. B* **10** (1974), 1979.
(Cit. on p. 14.)

[52] J. Friedel. "Metallic alloys". In: *Il Nuovo Cimento* **7** (1958), 287.
(Cit. on p. 14.)

[53] M. A. Ruderman and C. Kittel. "Indirect Exchange Coupling of Nuclear Magnetic Moments by Conduction Electrons". In: *Phys. Rev.* **96** (1954),

99.
(Cit. on p. 14.)

[54] T. Kasuya. "A Theory Of Metallic Ferromagnetism And Antiferromagnetism On Zeners Model". In: *Progress of Theoretical Physics* **16(1)** (1956), 45.
(Cit. on p. 14.)

[55] K. Yosida. "Magnetic Properties of Cu-Mn Alloys". In: *Phys. Rev.* **106** (1957), 893.
(Cit. on p. 14.)

[56] G. Genkin and M. Sapozhinikov. "Ruderman-Kittel-Kasuya-Yosida interaction between zerodimensional and onedimensional ferromagnetic inclusions in a matrix of nonmagnetic metal". In: *Appl. Phys. Lett.* **64** (1994), 796.
(Cit. on p. 14.)

[57] R. Skomski. "RKKY interaction between nanomagnets of arbitraty shape". In: *Europhys. Lett.* **48** (1999), 455.
(Cit. on p. 14.)

[58] N. Kolmakova, A. Tishin, and J. Bohr. "On the single-ion magnetic anisotropy of the rare-earth metals". In: *J. Magn. Magn. Mater.* **161** (1996), 245.
(Cit. on p. 15.)

[59] R. Briss, G. Keeler, and C. Shepard. "Temperature dependence of the magnetocrystalline anisotropy energy of terbium in the basal plane". In: *J. Phys. F: Metal Phys.* **7** (1977), 1669.
(Cit. on p. 15.)

[60] K. Tajima. "Magnetocristalline Anisotropy of Rare Earth Impurities Doped in Gadolinium". In: *J. Phys. Soc. Jpn.* **31** (1971), 441.
(Cit. on pp. 15, 95.)

[61] J. W. Cable and E. O. Wollan. "Neutron Diffraction Study of the Magnetic Behavior of Gadolinium". In: *Phys. Rev.* **165** (1968), 733.
(Cit. on p. 15.)

[62] K. Starke. *Magnetic Dichroism in Core-Level Photoemission*. Springer Berlin Heidelberg, 2000.
(Cit. on pp. 15, 32, 35–37, 40, 85.)

[63] C. Stamm, T. Kachel, N. Pontius, R. Mitzner, T. Quast, K. Holldack, S. Khan, C. Lupulescu, E. F. Aziz, M. Wietstruk, H. A. Dürr, and W. Eberhardt. "Femtosecond modification of electron localization and transfer of angular momentum in nickel". In: *Nat. Mater.* **6** (2007), 740.
(Cit. on p. 17.)

[64] J. Jensen and A. R. Mackintosh. *Rare Earth Magnetism*. Clarendon Press - Oxford, 1991.
(Cit. on pp. 17, 35, 95.)

[65] J. C. G. Houmann and R. M. Nicklow. "Lattice Dynamics of Terbium". In: *Phys. Rev. B* **1** (1970), 3943.
(Cit. on p. 17.)

[66] M. Rosen. "Elastic Moduli and Ultrasonic Attenuation of Gadolinium, Terbium, Dysprosium, Holmium, and Erbium from 4.2 to 300°K". In: *Phys. Rev.* **174** (1968), 504.
(Cit. on p. 17.)

[67] W. C. Koehler, H. R. Child, R. M. Nicklow, H. G. Smith, R. M. Moon, and J. W. Cable. "Spin-Wave Dispersion Relations in Gadolinium". In: *Phys. Rev. Lett.* **24** (1970), 16.
(Cit. on pp. 17, 72, 95.)

[68] U. Bovensiepen. "Coherent and incoherent excitations of the Gd(0001) surface on ultrafast timescales". In: *J. Phys.: Condens. Matter* **19** (2007), 083201.
(Cit. on pp. 17, 19, 74.)

[69] M. I. Kaganov, I. M. Lifshitz, and L. V. Tanatarov. "Relaxation between electrons and the crystalline lattice". In: *Sov. Phys. JETP* **4** (1957), 173.
(Cit. on p. 17.)

[70] S. I. Anisimov, B. L. Kapeliovich, and T. L. Perel'man. "Electron emission from metal surfaces exposed to ultrashort laser pulses". In: *Zh. Eksp. Teor. Fiz.* **66** (1974), 776.
(Cit. on p. 17.)

[71] S. Y. Dan'kov, A. M. Tishin, V. K. Pecharsky, and K. A. Gschneidner. "Magnetic phase transitions and the magnetothermal properties of gadolinium". In: *Phys. Rev. B* **57** (1998), 3478.
(Cit. on pp. 18, 19, 54, 83.)

[72] K. D. Jayasuriya, A. M. Stewart, S. J. Campbell, and E. S. R. Gopal. "The critical specific heat of terbium". In: *J. Phys. F: Met. Phys.* **14** (1984), 1725.
(Cit. on p. 18.)

[73] J. Hohlfeld, S.-S. Wellershoff, J. Güdde, U. Conrad, V. Jähnke, and E. Matthias. "Electron and lattice dynamics following optical excitation of metals". In: *Chem. Phys.* **251** (2000), 237.
(Cit. on p. 19.)

[74] G. K. White and S. J. Collocott. "Heat Capacity of Reference Materials: Cu and W". In: *J. Phys. Chem. Ref. Data* **13** (1984), 1251.
(Cit. on pp. 19, 83.)

[75] U. Nowak. *Handbook of magnetism and advanced materials 2*. Ed. by H. Kronmueller and S. Parkin. Wiley, 2007.
(Cit. on p. 21.)

[76] A. L'Huillier, K. J. Schafer, and K. Kulander. "Theoretical aspects of intense field harmonic generation". In: *J. Phys. B* **24** (1991), 3315.
(Cit. on p. 23.)

[77] H. Eichmann, A. Egbert, S. Nolte, C. Momma, B. Wellegehausen, W. Becker, S. Long, and J. K. McIver. "Polarization-dependent high-order two-color mixing". In: *Phys. Rev. A* **51** (1995), R3414.
(Cit. on p. 23.)

[78] B. Sundaram and P. W. Milonni. "High-order harmonic generation: Simplified model and relevance of single-atom theories to experiment". In: *Phys. Rev. A* **41** (1990), 6571.
(Cit. on p. 23.)

[79] M. Lewenstein, P. Balcou, M. Y. Ivanov, A. L'Huillier, and P. B. Corkum. "Theory of high-harmonic generation by low-frequency laser fields". In: *Phys. Rev. A* **49** (1994), 2117.
(Cit. on pp. 23, 27.)

[80] L. Keldysh. "Ionization in field of a strong electromagnetic wave". In: *Soviet Physics JETP-USSR* **20** (1965), 1307.
(Cit. on p. 24.)

[81] P. Milonni and B. Sundaram. *Progress in Optics, Volume XXXI*. Elsevier Science Publishers, 1993.
(Cit. on p. 24.)

[82] R. Kienberger and F. Krausz. *Few-Cycle Laser Pulse Generation and Its Applications*. Ed. by F. Kärtner. Springer, 2004.
(Cit. on p. 26.)

[83] H. Hertz. "Über einen Einfluss des ultravioletten Lichtes auf die electrische Entladung". In: *Annalen der Physik und Chemie* **267** (1887), 983.
(Cit. on p. 28.)

[84] W. Hallwachs. "Über den Einfluss des Lichtes auf electrostatisch geladene Körper". In: *Annalen der Physik und Chemie* **269** (1888), 301.
(Cit. on p. 28.)

[85] P. Lenard. "Über die Lichtelektrische Wirkung". In: *Annalen der Physik* **8** (1902), 169.
(Cit. on p. 28.)

[86] A. Einstein. "Über einen die Erzeugung und Verwandlung des Lichtes betreffenden heuristischen Gesichtspunkt". In: *Annalen der Physik* **17** (1905), 132.
(Cit. on p. 28.)

[87] F. Reinert and S. Hüfner. "Photoemission spectroscopy from early days to recent applications". In: *New J. Phys.* **7** (2005), 97.
(Cit. on p. 28.)

[88] A. Bostwick, T. Ohta, T. Seyller, K. Horn, and E. Rotenberg. "Quasiparticle dynamics in graphene". In: *Nature Phys.* **3** (2006), 36.
(Cit. on p. 28.)

[89] P. Dirac. "The Quantum Theory of Emission and Absorption of Radiation". In: *Proc. R. Soc. A* **114** (1927), 243.
(Cit. on p. 30.)

[90] G. Wentzel. "Über strahlungslose Quantensprünge". In: *Zeitschrift für Physik* **43** (1927), 524.
(Cit. on p. 30.)

[91] E. Fermi. *Nuclear Physics*. University of Chicago Press, 1950.
(Cit. on p. 30.)

[92] M. Seah and W. Dench. "Quantitative electron spectroscopy of surfaces: A standard data base for electron inelastic mean free paths in solids". In: *Surf. Interface Anal.* **1** (1979), 2.
(Cit. on p. 31.)

[93] J. Szajman, R. Leckey, J. Liesegang, and J. Jenkin. "Is there a universal mean-free-path curve for electron inelastic scattering in solids?" In: *J. Electron Spectrosc. Relat. Phenom.* **20** (1980), 323.
(Cit. on p. 31.)

[94] H. Lüth. *Surfaces and Interfaces of Solid Materials*. Springer Verlag, 1995.
(Cit. on p. 31.)

[95] D. Venus. "Magnetic circular dichroism in angular distributions of core-level photoelectrons". In: *Phys. Rev. B* **48** (1993), 6144.
(Cit. on p. 32.)

[96] C. M. Schneider, D. Venus, and J. Kirschner. "Strong x-ray magnetic circular dichroism in a "forbidden geometry" observed via photoemission". In: *Phys. Rev. B* **45** (1992), 5041.
(Cit. on p. 32.)

[97] C. Roth, H. Rose, F. Hillebrecht, and E. Kisker. "Magnetic linear dichroism in soft x-ray core level photoemission from iron". In: *Solid State Commun.* **86** (1993), 647.
(Cit. on pp. 32, 33, 85.)

[98] G. van der Laan and A. I. Figueroa. "X-ray magnetic circular dichroism - A versatile tool to study magnetism ". In: *Coord. Chem. Rev.* **277–278** (2014), 95.
(Cit. on p. 32.)

[99] B. T. Thole and G. van der Laan. "Spin polarization and magnetic dichroism in photoemission from core and valence states in localized magnetic systems". In: *Phys. Rev. B* **44** (1991), 12424.
(Cit. on p. 35.)

[100] G. van der Laan and B. T. Thole. "Spin polarization and magnetic dichroism in photoemission from core and valence states in localized magnetic systems. II. Emission from open shells". In: *Phys. Rev. B* **48** (1993), 210.
(Cit. on p. 35.)

[101] B. T. Thole and G. van der Laan. "Spin polarization and magnetic dichroism in photoemission from core and valence states in localized magnetic systems. III. Angular distributions". In: *Phys. Rev. B* **49** (1994), 9613.
(Cit. on pp. 35, 36.)

[102] G. van der Laan. "Angular-resolved linear and circular dichroism in core-level photoemission of metallic systems". In: *Phys. Rev. B* **51** (1995), 240.
(Cit. on pp. 35, 36.)

[103] G. Panaccione, P. Torelli, G. Rossi, G. van der Laan, P Prieto, and F Sirotti. "Magnetic linear dichroism in Gd 4f and 4d photoemission of magnetic interfaces". In: *J. Phys.: Condens. Matter* **11** (1999), 3431.
(Cit. on p. 35.)

[104] R. D. Cowan. *Theory of Atomic Spectra and Structure*. University of California Press, Berkeley, 1981.
(Cit. on p. 37.)

[105] O. Krupin. "Dichroism and Rashba effect at magnetic crystal surfaces of rare-earth metals". PhD thesis. Freie Universität Berlin, 2004.
(Cit. on pp. 38, 40, 57, 85, 86.)

[106] R. Schellenberg, E. Kisker, A. Fanelsa, F. U. Hillebrecht, J. G. Menchero, A. P. Kaduwela, C. S. Fadley, and M. A. Van Hove. "Photoelectron diffraction: A source for magnetic dichroism in angle-resolved photoemission from ferromagnets". In: *Phys. Rev. B* **57** (1998), 14310.
(Cit. on pp. 38, 85.)

[107] F. J. García de Abajo, M. A. Van Hove, and C. S. Fadley. "Multiple scattering of electrons in solids and molecules: A cluster-model approach". In: *Phys. Rev. B* **63** (2001), 075404.
(Cit. on p. 40.)

[108] F. Krausz and M. Ivanov. "Attosecond physics". In: *Rev. Mod. Phys.* **81** (2009), 163.
(Cit. on p. 41.)

[109] C. La-O-Vorakiat, M. Siemens, M. M. Murnane, H. C. Kapteyn, S. Mathias, M. Aeschlimann, P. Grychtol, R. Adam, C. M. Schneider, J. M. Shaw, H. Nembach, and T. J. Silva. "Ultrafast Demagnetization Dynamics at the M Edges of Magnetic Elements Observed Using a Tabletop High-Harmonic Soft X-Ray Source". In: *Phys. Rev. Lett.* **103** (2009), 257402.
(Cit. on p. 41.)

[110] R. Sandberg, D. Raymondson, C. La-O-Vorakiat, A. Paul, K. Raines, J. Miao, M. Murnane, H. Kapteyn, and W. Schlotter. "Tabletop soft-x-ray

Fourier transform holography with 50 nm resolution". In: *Opt. Lett.* **34** (2009), 1618.
(Cit. on p. 41.)

[111] E. Magerl, S. Neppl, A. L. Cavalieri, E. M. Bothschafter, M. Stanislawski, T. Uphues, M. Hofstetter, U. Kleineberg, J. V. Barth, D. Menzel, D. F. Krausz, R. Ernstorfer, R. Kienberger, and P. Feulner. "A flexible apparatus for attosecond photoelectron spectroscopy of solids and surfaces". In: *Rev. Sci. Instrum.* **82** (2011), 063104.
(Cit. on pp. 41, 42.)

[112] G. L. Dakovski, Y Li, T Durakiewicz, and G Rodriguez. "Tunable ultrafast extreme ultraviolet source for time- and angle-resolved photoemission spectroscopy." In: *Rev. Sci. Instrum.* **81** (2010), 073108.
(Cit. on pp. 41, 42.)

[113] M. Bauer. "Femtosecond ultraviolet photoelectron spectroscopy of ultrafast surface processes". In: *J. Phys. D: Appl. Phys.* **38** (2005), R253.
(Cit. on p. 41.)

[114] S. Mathias, L. Miaja-Avila, M. M. Murnane, H. Kapteyn, M. Aeschlimann, and M. Bauer. "Angle-resolved photoemission spectroscopy with a femtosecond high harmonic light source using a two-dimensional imaging electron analyzer." In: *Rev. Sci. Instrum.* **78** (2007), 083105.
(Cit. on pp. 41, 42.)

[115] J. C. Petersen, S. Kaiser, N. Dean, A. Simoncig, H. Y. Liu, A. L. Cavalieri, C. Cacho, I. C. E. Turcu, E. Springate, F. Frassetto, L. Poletto, S. S. Dhesi, H. Berger, and A. Cavalleri. "Clocking the Melting Transition of Charge and Lattice Order in $1T$-TaS_2 with Ultrafast Extreme-Ultraviolet Angle-Resolved Photoemission Spectroscopy". In: *Phys. Rev. Lett.* **107** (2011), 177402.
(Cit. on p. 41.)

[116] P. Wernet, J. Gaudin, K. Godehusen, O. Schwarzkopf, and W. Eberhardt. "Femtosecond time-resolved photoelectron spectroscopy with a vacuum-ultraviolet photon source based on laser high-order harmonic generation." In: *Rev. Sci. Instrum.* **82** (2011), 063114.
(Cit. on pp. 41, 42.)

[117] A. Melzer, D. Kampa, J. Wang, and T. Fauster. "Time-resolved photoemission at the Si(100)-Ga surface using a femtosecond higher-harmonic laser source". In: *Phys. Rev. B* **80** (2009), 205424.
(Cit. on p. 42.)

[118] C.-T. Chiang, A. Blättermann, M. Huth, J. Kirschner, and W. Widdra. "High-order harmonic generation at 4MHz as a light source for time-of-flight photoemission spectroscopy". In: *Appl. Phys. Lett.* **101** (2012), 071116.
(Cit. on p. 42.)

[119] J. Norin, K. Osvay, F. Albert, D. Descamps, J. Yang, A. L'Huillier, and C.-G. Wahlström. "Design of an extreme-ultraviolet monochromator free from temporal stretching." In: *Appl. Opt.* **43** (2004), 1072.
(Cit. on p. 42.)

[120] L. Nugent-Glandorf, M. Scheer, D. A. Samuels, V. Bierbaum, and S. R. Leone. "A laser-based instrument for the study of ultrafast chemical dynamics by soft x-ray-probe photoelectron spectroscopy". In: *Rev. Sci. Instrum.* **73** (2002), 1875.
(Cit. on p. 42.)

[121] L. Poletto. "Time-compensated grazing-incidence monochromator for extreme-ultraviolet and soft X-ray high-order harmonics". In: *Appl. Phys. B: Lasers Opt.* **78** (2004), 1013.
(Cit. on p. 42.)

[122] F. Frassetto, S. Bonora, P. Villoresi, L. Poletto, E. Springate, C. A. Froud, I. C. E. Turcu, A. J. Langley, D. S. Wolff, J. L. Collier, S. S. Dhesi, and A. Cavalleri. "Design and characterization of the XUV monochromator for ultrashort pulses at the ARTEMIS facility". In: *Proc. of SPIE* **7077** (2008), 1.
(Cit. on p. 42.)

[123] P. Siffalovic, M. Drescher, M. Spieweck, T. Wiesenthal, Y. C. Lim, R. Weidner, A. Elizarov, and U. Heinzmann. "Laser-based apparatus for extended ultraviolet femtosecond time-resolved photoemission spectroscopy". In: *Rev. Sci. Instrum.* **72** (2001), 30.
(Cit. on p. 42.)

[124] T. Haarlammert and H. Zacharias. "Application of high harmonic radiation in surface science". In: *Curr. Opin. Solid State Mater. Sci.* **13** (2009), 13.
(Cit. on p. 42.)

[125] F. Schäfers. *Reflec.* Tech. rep. Berliner Elektronen Speicherring für Synchrotronstrahlung, 1996.
(Cit. on p. 42.)

[126] F. Schäfers. *The BESSY Raytrace Program RAY*. Ed. by A. Erko, M. Idir, T. Krist, and A. G. Michette. Vol. 137. Springer Series in optical science. Springer Berlin Heidelberg, 2008, 9.
(Cit. on p. 42.)

[127] P. Wernet, K. Godehusen, O. Schwarzkopf, and W. Eberhardt. *Femtosecond VUV Photon Pulses for Time-resolved Photoelectron Spectroscopy*. Ed. by P. Corkum, D. M. Jonas, R. J. D. Miller, and A. M. Weiner. Vol. 88. Springer Series in Chemical Physics. Springer Berlin Heidelberg, 2007, 45.
(Cit. on p. 43.)

[128] L. Nugent-Glandorf, M. Scheer, M. Krishnamurthy, J. Odom, and S. Leone. "Photoelectron spectroscopic determination of the energy bandwidths of

high-order harmonics (7th-55th) produced by an ultrafast laser in neon". In: *Phys. Rev. A* **62** (2000), 023812.
(Cit. on p. 43.)

[129] O. E. Martinez. "Pulse distortion in tilted pulse schemes for ultrashort pulses". In: *Optics Comm.* **59** (1986), 229.
(Cit. on pp. 43, 44.)

[130] T. Noll, T. Zeschke, G. Reichardt, H. Lammert, and W. Gudat. "Six-strut arrangements for cartesian movements of mirrors". In: *Nucl. Instrum. Methods Phys. Res., Sect. A* **467-468** (2001), 775.
(Cit. on p. 45.)

[131] P. Salières, A. L'Huillier, and M. Lewenstein. "Coherence Control of High-Order Harmonics". In: *Phys. Rev. Lett.* **74** (1995), 3776.
(Cit. on p. 46.)

[132] L. Miaja-Avila, C. Lei, M. Aeschlimann, J. L. Gland, M. M. Murnane, H. C. Kapteyn, and G. Saathoff. "Laser-Assisted Photoelectric Effect from Surfaces". In: *Phys. Rev. Lett.* **97** (2006), 113604.
(Cit. on p. 51.)

[133] G. Saathoff, L. Miaja-Avila, M. Aeschlimann, M. M. Murnane, and H. C. Kapteyn. "Laser-assisted photoemission from surfaces". In: *Phys. Rev. A* **77** (2008), 022903.
(Cit. on p. 51.)

[134] J. M. Schins, P. Breger, P. Agostini, R. C. Constantinescu, H. G. Muller, A. Bouhal, G. Grillon, A. Antonetti, and A. Mysyrowicz. "Cross-correlation measurements of femtosecond extreme-ultraviolet high-order harmonics". In: *J. Opt. Soc. Am. B: Opt. Phys.* **13** (1996), 197.
(Cit. on p. 51.)

[135] S. Hellmann, K. Rossnagel, M. Marczynski-Bühlow, and L. Kipp. "Vacuum space-charge effects in solid-state photoemission". In: *Phys. Rev. B* **79** (2009), 035402.
(Cit. on p. 51.)

[136] S. Passlack, S. Mathias, O. Andreyev, D. Mittnacht, M. Aeschlimann, and M. Bauer. "Space charge effects in photoemission with a low repetition, high intensity femtosecond laser source". In: *J. Appl. Phys.* **100** (2006), 024912.
(Cit. on p. 51.)

[137] A. Melnikov, H. Prima-Garcia, M. Lisowski, T. Gießel, R. Weber, R. Schmidt, C. Gahl, N. M. Bulgakova, U. Bovensiepen, and M. Weinelt. "Nonequilibrium Magnetization Dynamics of Gadolinium Studied by Magnetic Linear Dichroism in Time-Resolved $4f$ Core-Level Photoemission". In: *Phys. Rev. Lett.* **100** (2008), 107202.
(Cit. on pp. 54, 71, 85.)

[138] S. C. Wu, H. Li, Y. S. Li, D. Tian, J. Quinn, F. Jona, and D. Fort. "Surface state on clean Tb(0001)". In: *Phys. Rev. B* **44** (1991), 13720.
(Cit. on p. 56.)

[139] J. Kolaczkiewicz and E. Bauer. "The Adsorption of Eu, Gd and Tb on the W(110) Surface". In: *Surf. Sci.* **175** (1986), 487.
(Cit. on p. 56.)

[140] U. Stetter, M. Farle, K. Baberschke, and W. G. Clark. "Critical behavior of strained epitaxial Gd films: *In situ* ac-susceptibility measurements in UHV". In: *Phys. Rev. B* **45** (1992), 503.
(Cit. on p. 56.)

[141] R. Musket, W. McLean, C. Colmenares, D. Makowiecki, and W. Siekhaus. "Preparation of atomically clean surfaces of selected elements: a review". In: *Application of Surface Science* **10** (1982), 143.
(Cit. on p. 56.)

[142] M. Bode, R. Pascal, and R. Wiesendanger. "STM study of carbon-induced reconstructions on W(110): strong evidence for a surface lattice deformation". In: *Surf. Sci.* **344** (1995), 185.
(Cit. on p. 56.)

[143] K. Zakeri, T. Peixoto, Y. Zhang, J. Prokop, and J. Kirschner. "On the preparation of clean tungsten single crystals". In: *Surf. Sci.* **604** (2010), L1.
(Cit. on p. 56.)

[144] A. Aspelmeier, F. Gerhardter, and K. Baberschke. "Magnetism and structure of ultrathin Gd films". In: *J. Magn. Magn. Mater.* **132** (1994), 22.
(Cit. on pp. 58, 64, 65, 95.)

[145] C. Puglia, A. Nilsson, B. Hernnäs, O. Karis, P. Bennich, and N. Martensson. "Physisorbed, chemisorbed and dissociated O_2 on Pt(111) studied by different core level spectroscopy methods". In: *Surf. Sci.* **342** (1995), 119.
(Cit. on p. 58.)

[146] J. Zhang, P. A. Dowben, D. Li, and M. Onellion. "Angle-resolved photoemission study of oxygen chemisorption on Gd(0001)". In: *Surf. Sci.* **329** (1995), 177.
(Cit. on p. 58.)

[147] D. N. McIlroy, C. Waldfried, D. Li, J. Pearson, S. D. Bader, D.-J. Huang, P. D. Johnson, R. F. Sabiryanov, S. S. Jaswal, and P. A. Dowben. "Oxygen Induced Suppression of the Surface Magnetization of Gd(0001)". In: *Phys. Rev. Lett.* **76** (1996), 2802.
(Cit. on pp. 58, 97.)

[148] D. Li, J. Zhang, P. A. Dowben, and M. Onellion. "Altering the Gd(0001) surface electronic structure with hydrogen adsorption". In: *Phys. Rev. B* **48** (1993), 5612.
(Cit. on p. 58.)

[149] B. Andres, M. Christ, M. Wietstruk, C. Gahl, M. Weinelt, and J. Kirschner. "Stoner-like response of the Gd(0001) surface state to femtosecond laser excitation". Freie Universität Berlin, unpublished. 2015.
(Cit. on pp. 60, 74.)

[150] L. M. Sandratskii. "Exchange splitting of surface and bulk electronic states in excited magnetic states of Gd: First-principles study". In: *Phys. Rev. B* **90** (2014), 184406.
(Cit. on pp. 61, 70.)

[151] J. K. Lang, Y. Baer, and P. A. Cox. "Study of the 4f and valence band density of states in rare-earth metals: II. Experiment and results". In: *J. Phys. F: Met. Phys.* **11** (1981), 121.
(Cit. on pp. 61, 91.)

[152] H. Chapellmann and V. Vieira. "Strong short-range magnetic order in ferromagnetic transition metals above T_C: a theoretical explanation". In: *Solid State Commun.* **43** (1982), 747.
(Cit. on p. 62.)

[153] M. Getzlaff, M. Bode, S. Heinze, R. Pascal, and R. Wiesendanger. "Temperature-dependent exchange splitting of the magnetic Gd(0001) surface state". In: *J. Magn. Magn. Mater.* **184** (1998), 155.
(Cit. on pp. 62–65, 95.)

[154] M. Bode, M. Getzlaff, a. Kubetzka, R. Pascal, O. Pietzsch, and R. Wiesendanger. "Temperature-Dependent Exchange Splitting of a Surface State on a Local-Moment Magnet: Tb(0001)". In: *Phys. Rev. Lett.* **83** (1999), 3017.
(Cit. on p. 62.)

[155] K. Maiti, M. C. Malagoli, A. Dallmeyer, and C. Carbone. "Finite Temperature Magnetism in Gd: Evidence against a Stoner Behavior". In: *Phys. Rev. Lett.* **88** (2002), 167205.
(Cit. on pp. 63, 64, 74, 79, 95.)

[156] C. E. Graves et al. "Nanoscale spin reversal by non-local angular momentum transfer following ultrafast laser excitation in ferrimagnetic GdFeCo." In: *Nat. Mater.* **12** (2013), 293.
(Cit. on pp. 64, 89.)

[157] K. Binder and D. P. Landau. "Crossover Scaling and Critical Behavior at the "Surface-Bulk" Multicritical Point". In: *Phys. Rev. Lett.* **52** (1984), 318.
(Cit. on pp. 64, 95.)

[158] R. Wu, C. Li, A. J. Freeman, and C. L. Fu. "Structural, electronic, and magnetic properties of rare-earth metal surfaces: hcp Gd(0001)". In: *Phys. Rev. B* **44** (1991), 9400.
(Cit. on pp. 64, 95.)

[159] T. Kaneyoshi. "Surface magnetism; magnetization and anisotropy at a surface". In: *J. Phys.: Condens. Matter* **3** (1991), 4497.
(Cit. on pp. 64, 95.)

[160] D. Weller, S. F. Alvarado, W. Gudat, K. Schröder, and M. Campagna. "Observation of Surface-Enhanced Magnetic Order and Magnetic Surface Reconstruction on Gd(0001)". In: *Phys. Rev. Lett.* **54** (1985), 1555.
(Cit. on pp. 64, 65, 95.)

[161] D. Weller and S. F. Alvarado. "Possible evidence for a first-order magnetic phase transition on the Gd(0001) surface". In: *Phys. Rev. B* **37** (1988), 9911.
(Cit. on pp. 64, 95.)

[162] E. Vescovo, C. Carbone, and O. Rader. "Surface magnetism of Gd(0001) films: Evidence for an unexpected phase transition". In: *Phys. Rev. B* **48** (1993), 7731.
(Cit. on pp. 64, 95.)

[163] H. Tang, D. Weller, T. G. Walker, J. C. Scott, C. Chappert, H. Hopster, A. W. Pang, D. S. Dessau, and D. P. Pappas. "Magnetic reconstruction of the Gd(0001) surface". In: *Phys. Rev. Lett.* **71** (1993), 444.
(Cit. on pp. 64, 65, 95.)

[164] A. Fedorov, T. Valla, D. Huang, G. Reisfeld, F. Loeb, F. Liu, and P. Johnson. "Spin polarized photoemission studies of the Gd(0001) surface". In: *J. Electron Spectrosc. Relat. Phenom.* **92** (1998), 19.
(Cit. on pp. 64, 95.)

[165] C. S. Arnold and D. P. Pappas. "Gd(0001): A Semi-Infinite Three-Dimensional Heisenberg Ferromagnet with *Ordinary* Surface Transition". In: *Phys. Rev. Lett.* **85** (2000), 5202.
(Cit. on pp. 64, 95.)

[166] M. Donath, B. Gubanka, and F. Passek. "Temperature-Dependent Spin Polarization of Magnetic Surface State at Gd(0001)". In: *Phys. Rev. Lett.* **77** (1996), 5138.
(Cit. on pp. 64, 95.)

[167] G. A. Mulhollan, K. Garrison, and J. L. Erskine. "Surface magnetism of Gd(0001): Evidence of ferromagnetic coupling to bulk". In: *Phys. Rev. Lett.* **69** (1992), 3240.
(Cit. on p. 65.)

[168] D. Li, J. Zhang, P. A. Dowben, and K. Garrison. "Evidence for imperfect ferromagnetic coupling between the Gd (0001) surface and the bulk". In: *J. Phys.: Condens. Matter* **5** (1993), L73.
(Cit. on p. 65.)

[169] A. W. Pang, A. Berger, and H. Hopster. "Magnetization behavior of thick epitaxial Gd(0001) films on W(110)". In: *Phys. Rev. B* **50** (1994), 6457.
(Cit. on p. 65.)

[170] A. Melnikov, I. Radu, U. Bovensiepen, O. Krupin, K. Starke, E. Matthias, and M. Wolf. "Coherent Optical Phonons and Parametrically Coupled Magnons Induced by Femtosecond Laser Excitation of the Gd(0001) Surface". In: *Phys. Rev. Lett.* **91** (2003), 227403.
(Cit. on pp. 65, 95.)

[171] R. C. White, C. S. Fadley, M. Sagurton, P. Roubin, D. Chandesris, J. Lecante, C. Guillot, and Z. Hussain. "Nondirect transitions in variable-temperature angle-resolved photoemission from metals". In: *Phys. Rev. B* **35** (1987), 1147.
(Cit. on p. 66.)

[172] E. Navas, K. Starke, C. Laubschat, E. Weschke, and G. Kaindl. "Surface core-level shift of 4 f states for Tb(0001)". In: *Phys. Rev. B* **48** (1993), 14753.
(Cit. on pp. 67, 86.)

[173] M. Sultan, U. Atxitia, A. Melnikov, O. Chubykalo-Fesenko, and U. Bovensiepen. "Electron- and phonon-mediated ultrafast magnetization dynamics of Gd(0001)". In: *Phys. Rev. B* **85** (2012), 184407.
(Cit. on pp. 70, 80, 83.)

[174] J. Jensen and J. G. Houmann. "Spin waves in terbium. II. Magnon-phonon interaction". In: *Phys. Rev. B* **12** (1975), 320.
(Cit. on pp. 72, 95.)

[175] M. Wietstruk, A. Melnikov, C. Stamm, T. Kachel, N. Pontius, M. Sultan, C. Gahl, M. Weinelt, H. A. Dürr, and U. Bovensiepen. "Hot-Electron-Driven Enhancement of Spin-Lattice Coupling in Gd and Tb 4f Ferromagnets Observed by Femtosecond X-Ray Magnetic Circular Dichroism". In: *Phys. Rev. Lett.* **106** (2011), 127401.
(Cit. on pp. 72, 93, 94, 101.)

[176] M. Lisowski, P. Loukakos, a. Melnikov, I. Radu, L. Ungureanu, M. Wolf, and U. Bovensiepen. "Femtosecond Electron and Spin Dynamics in Gd(0001) Studied by Time-Resolved Photoemission and Magneto-optics". In: *Phys. Rev. Lett.* **95** (2005), 137402.
(Cit. on pp. 74, 95.)

[177] A. V. Fedorov, T. Valla, F. Liu, P. D. Johnson, M. Weinert, and P. B. Allen. "Spin-resolved photoemission study of photohole lifetimes in ferromagnetic gadolinium". In: *Phys. Rev. B* **65** (2002), 212409.
(Cit. on p. 74.)

[178] P. Loukakos, M. Lisowski, G. Bihlmayer, S. Blügel, M. Wolf, and U. Bovensiepen. "Dynamics of the Self-Energy of the Gd(0001) Surface State Probed

by Femtosecond Photoemission Spectroscopy". In: *Phys. Rev. Lett.* **98** (2007), 097401.
(Cit. on p. 74.)

[179] K. M. Döbrich, a. Bostwick, E. Rotenberg, and G. Kaindl. "Change of the Fermi surface of Gd metal upon magnetic ordering as seen via angle-resolved photoelectron spectroscopy". In: *Phys. Rev. B* **81** (2010), 012401.
(Cit. on pp. 74, 76.)

[180] P. B. Allen. "Electron spin-flip relaxation by one magnon processes: Application to the gadolinium surface band". In: *Phys. Rev. B* **63** (2001), 214410.
(Cit. on p. 74.)

[181] A. Baral, S. Vollmar, and H. C. Schneider. "Magnetization dynamics and damping due to electron-phonon scattering in a ferrimagnetic exchange model". In: *Phys. Rev. B* **90** (2014), 014427.
(Cit. on p. 76.)

[182] A. Baral and H. C. Schneider. "Magnetic switching dynamics due to ultrafast exchange scattering: A model study". In: *Phys. Rev. B* **91** (2015), 100402.
(Cit. on p. 76.)

[183] I. D. Hughes, M. Dane, A. Ernst, W. Hergert, M. Luders, J. Poulter, J. B. Staunton, A. Svane, Z. Szotek, and W. M. Temmerman. "Lanthanide contraction and magnetism in the heavy rare earth elements". In: *Nature* **446** (2007), 650.
(Cit. on pp. 76, 95.)

[184] S. S. Kushwaha and A Kumar. "An electron gas model for the lattice dynamics of lanthanides". In: *J. Phys. C: Solid State Physics* **4** (1971), 1674.
(Cit. on p. 76.)

[185] R. M. Bozorth and T. Wakiyama. "Magnetostriction and Anomalous Thermal Expansion of Single Crystals of Gadolinium". In: *J. Appl. Phys.* **34** (1963), 1351.
(Cit. on p. 76.)

[186] M. J. Lisowski. "Elektronen- und Magnetisierungsdynamik in Metallen untersucht mit zeitaufgelöster Photoemission". PhD thesis. Freie Universität Berlin, 2005.
(Cit. on pp. 82, 83.)

[187] U. Atxitia, O. Chubykalo-Fesenko, J. Walowski, A. Mann, and M. Münzenberg. "Evidence for thermal mechanisms in laser-induced femtosecond spin dynamics". In: *Phys. Rev. B* **81** (2010), 174401.
(Cit. on p. 83.)

[188] C. La-O-Vorakiat, E. Turgut, C. A. Teale, H. C. Kapteyn, M. M. Murnane, S. Mathias, M. Aeschlimann, C. M. Schneider, J. M. Shaw, H. T. Nembach, and T. J. Silva. "Ultrafast Demagnetization Measurements Using Extreme

Ultraviolet Light: Comparison of Electronic and Magnetic Contributions". In: *Phys. Rev. X* **2** (2012), 011005.
(Cit. on p. 83.)

[189] M. Sultan, A. Melnikov, and U. Bovensiepen. "Ultrafast magnetization dynamics of Gd(0001): Bulk versus surface". In: *Phys. Status Solidi B* **248** (2011), 2323.
(Cit. on p. 83.)

[190] G. Tas and H. J. Maris. "Electron diffusion in metals studied by picosecond ultrasonics". In: *Phys. Rev. B* **49** (1994), 15046.
(Cit. on p. 84.)

[191] R. Kammerer, J. Barth, F. Gerken, A. Flodström, and L. Johansson. "4f-surface binding energy shift for Eu and Gd metals". In: *Solid State Commun.* **41** (1982), 435.
(Cit. on p. 86.)

[192] B. Johansson. "Valence state at the surface of rare-earth metals". In: *Phys. Rev. B* **19** (1979), 6615.
(Cit. on p. 86.)

[193] S. Mathias, C. La-o vorakiat, P. Grychtol, P. Granitzka, E. Turgut, J. M. Shaw, M. Aeschlimann, M. M. Murnane, and H. C. Kapteyn. "Probing the timescale of the exchange interaction in a ferromagnetic alloy". In: *PNAS* **109** (2012), 4792.
(Cit. on p. 89.)

[194] N. Bergeard, V. López-Flores, V. Halté, M. Hehn, C. Stamm, N. Pontius, E. Beaurepaire, and C. Boeglin. "Ultrafast angular momentum transfer in multisublattice ferrimagnets". In: *Nat. Commun.* **5** (2014), 4466.
(Cit. on p. 89.)

[195] A. R. Khorsand, M. Savoini, A. Kirilyuk, A. V. Kimel, A. Tsukamoto, A. Itoh, and T. Rasing. "Element-Specific Probing of Ultrafast Spin Dynamics in Multisublattice Magnets with Visible Light". In: *Phys. Rev. Lett.* **110** (2013), 107205.
(Cit. on p. 89.)

[196] W. Platow, A. N. Anisimov, G. L. Dunifer, M. Farle, and K. Baberschke. "Correlations between ferromagnetic-resonance linewidths and sample quality in the study of metallic ultrathin films". In: *Phys. Rev. B* **58** (1998), 5611.
(Cit. on p. 92.)

[197] G. van der Laan. "Applications of soft x-ray magnetic dichroism". In: *J. Phys.: Conf. Series* **430** (2013), 012127.
(Cit. on p. 94.)

[198] O. Eriksson, A. M. Boring, R. C. Albers, G. W. Fernando, and B. R. Cooper. "Spin and orbital contributions to surface magnetism in 3d elements". In:

Phys. Rev. B **45** (1992), 2868.
(Cit. on p. 95.)

[199] D. L. Mills. "Surface anisotropy and surface spin canting in the semi-infinite ferromagnet". In: *Phys. Rev. B* **39** (1989), 12306.
(Cit. on p. 95.)

[200] G. Woltersdorf, M. Kiessling, G. Meyer, J.-U. Thiele, and C. H. Back. "Damping by Slow Relaxing Rare Earth Impurities in $Ni_{80}Fe_{20}$". In: *Phys. Rev. Lett.* **102** (2009), 257602.
(Cit. on p. 97.)

[201] C. Luo, D. Zhang, Y. Wang, H. Huang, Y. Zhai, and H. Zhai. "Angular dependence of ferromagnetic resonance in Tb-doped $Ni_{80}Fe_{20}$ thin films ". In: *J. Alloys Compd.* **598** (2014), 57.
(Cit. on p. 97.)

Acknowledgments

First I want to thank Prof. Martin Weinelt for giving me the opportunity to work in this exciting field of physics. This thesis is based on his – at the time – novel idea of time-resolved band-structure analysis based on a higher harmonic source. His encouragement and dedication were needed to beat the odds. He always had an open ear and helpful advice whenever there was a problem. The discussions with him were invaluable for my understanding of the observed magnetic phenomena and helped to solve many mysteries. I thank Prof. Karsten Horn for his encouragement during my time as an engineer to sign up for physics and for co-assessing this work.

Of all colleagues, foremost mentioned should be Robert Carley, Martin Teichmann and Kristian Döbrich. They were an integral part of the HHG project, without their preliminary work and their combined expertise these novel magnetization experiments would not have been possible. Beyond that, I need to thank Robert particularly for his indefatigable efforts that kept the laser running, Martin for his incredible python programs, and Kristian for sharing his knowledge that shed some light on the mystery of lanthanide magnetism. I am very grateful that, even after all of you left the project, you still supported me, whether through actual help with the laser, python code, or by proofreading this thesis. Also mentioned should be John Bowlan who joined the HHG-team temporarily and whose help during measurements was well appreciated. Beam time and dragon fighting with all of you guys has been fun!

I thank all members of the AG Weinelt for the pleasant working environment and the cross-project help. In particular, for gadolinium and paper discussions, Beatrice Andres – I have to apologize for disturbing your work flow repeatedly with my magnetism-troubled thoughts. I thank Daniel Brete for his support concerning technical and administrative details; Cornelius Gahl, Thomas Moldt, Marko Wietstruk and Christoph Trabant for helpful discussions.

I thank Kamil Bobowski and Markus Gleich for their forbearance. I know that the supervision during the writing period of this thesis was not as intense as it should be.

For theoretical backup I have to thank Sönke Wienholdt, Denise Hinzke, Prof. Ulrich Nowak, Karel Carva and Prof. Peter Oppeneer. Their simulations contributed significantly to the interpretation of the distinct timescales found in Gd.

Finally I want to thank my parents and friends for their patience and support.

Academic curriculum vitae

Der Lebenslauf ist in der Online-Version aus Gründen des Datenschutzes nicht enthalten.

Selbstständigkeitserklärung gemäß §7 der Promotionsordnung

Ich, Björn Frietsch, versichere, dass ich die vorliegende Dissertation selbstständig verfasst und sämtliche Hilfsmittel, Hilfen und Quellen angegeben habe. Diese Arbeit wurde bisher weder in dieser noch in ähnlicher Form einer Promotionskomission vorgelegt.

Björn Frietsch

Berlin, den 09.09.2015